

NORTHWESTERN UNIVERSITY

Search for the Higgs Boson Decays to a Photon and Two Leptons  
with Low Dilepton Invariant Mass.

A DISSERTATION

SUBMITTED TO THE GRADUATE SCHOOL  
IN PARTIAL FULFILLMENT OF THE REQUIREMENTS

for the degree

DOCTOR OF PHILOSOPHY

Field of Physics and Astronomy

By

Andrey Pozdnyakov

EVANSTON, ILLINOIS

December 2015

© Copyright by Andrey Pozdnyakov 2015

All Rights Reserved

## ABSTRACT

Search for the Higgs Boson Decays to a Photon and Two Leptons  
with Low Dilepton Invariant Mass.

Andrey Pozdnyakov

A search for a Higgs boson decay  $H \rightarrow \gamma^* \gamma \rightarrow \ell \ell \gamma$  is presented. The analysis is performed using proton-proton collision data recorded by the CMS detector at the CERN LHC at a centre-of-mass energy of 8 TeV, corresponding to an integrated luminosity of  $19.7 \text{ fb}^{-1}$ . The selected events have an opposite-sign muon or electron pair and a high transverse momentum photon. No excess above background has been found in the three-body invariant mass range  $120 < m_{\ell \ell \gamma} < 150 \text{ GeV}$ , and limits have been derived for the Higgs boson production cross section times branching fraction for the  $H \rightarrow \gamma^* \gamma \rightarrow \ell \ell \gamma$  decay, where the dilepton invariant mass is less than 20 GeV. For a Higgs boson with  $m_H = 125 \text{ GeV}$ , a 95% confidence level (CL) exclusion observed (expected) limit is 6.7 ( $5.9^{+2.8}_{-1.8}$ ) times the standard model prediction.

Additionally, a search for  $H \rightarrow (J/\psi) \gamma \rightarrow \mu \mu \gamma$  process is presented, and an upper limit at 95% CL on the branching fraction of the  $H \rightarrow (J/\psi) \gamma$  decay for the 125 GeV Higgs boson is set at  $1.5 \times 10^{-3}$ .

## **Acknowledgements**

I would like to thank my mentor and advisor Mayda Velasco for all the support. I also wish to thank Stoyan Stoynev, Michael Schmitt, Brian Pollack, Nathaniel Odell, Chia-Ming Kuo and Chiu-Ping Chang for the help and feedback provided for the analysis.

## Preface

As it is clear from the title of this dissertation, you will learn something new about the Higgs boson from it. In Chapter 1 I will give a brief introduction to the Standard Model (SM) of Particle Physics and describe the Higgs mechanism. There I will also motivate the search for the particular decay of the Higgs boson into two leptons and a photon, which is the main subject of the dissertation.

Then, in Chapter 2 I will give a short description of the CMS detector including its main subsystems relevant for the analysis. There are more than 2000 scientists working on the CMS experiment and everyone contributes to the detector support in order to ensure its smooth operation. Personally, I was responsible for the beam timing detector at CMS, during 2012 data-taking. I implemented the online software for monitoring of the beam arrival times. This work is described in Section 2.2.

In Chapter 3 I come back to the main topic of the dissertation and describe all the details of the search analysis for  $H \rightarrow \gamma^* \gamma \rightarrow \ell \ell \gamma$  and  $H \rightarrow (J/\psi) \gamma \rightarrow \mu \mu \gamma$  decays. And in Chapter 4 I present the results and conclude. I hope you will enjoy the reading.

## Table of Contents

ABSTRACT	3
Acknowledgements	4
Preface	5
List of Tables	8
List of Figures	10
Chapter 1. Introduction	16
1.1. Standard Model theory and Higgs Mechanism	16
1.2. Higgs boson production at the LHC	22
1.3. Decays of the Higgs boson	26
1.4. Higgs boson decays into $\ell^+\ell^-\gamma$ final state	28
Chapter 2. Experimental Apparatus	38
2.1. Compact Muon Solenoid	38
2.2. Beam timing measurement at CMS	45
Chapter 3. Physics Analysis: Search for $H \rightarrow \ell\ell\gamma$	49
3.1. Features of the decay	49
3.2. Simulated samples	50

3.3. Background Estimation and Analysis Strategy	53
3.4. Event reconstruction	55
3.5. Event selection	64
3.6. Statistical Methods	74
3.7. Systematic uncertainties	83
Chapter 4. Results	94
4.1. Muon channel	94
4.2. Combination with the Electron Channel	95
4.3. Model independent limits	98
4.4. Differential limits in bins of $m_{\mu\mu}$	99
4.5. Result for $H \rightarrow (J/\psi)\gamma$	102
4.6. Conclusion and outlook	103
References	105
Appendix A. $J/\psi$ polarization	111
Appendix B. Background Simulation study in Muon Channel	113
Appendix C. Vector Bosons Fusion selection in muon channel	118
Appendix D. Auxiliary information and plots	121
D.1. Muon channel	121
D.2. Electron channel	137
D.3. $H \rightarrow (J/\psi)\gamma$	146
Appendix E. Effect of the Systematics on the Expected Limits	150

## List of Tables

1.1	Cross sections of the SM Higgs boson production and branching fraction of the $H \rightarrow \ell\ell\gamma$ decay process.	33
3.1	Number of expected signal events at $\sqrt{s} = 8$ TeV with $19.7 \text{ fb}^{-1}$ .	52
3.2	Photon ID scale factors applied per photon.	63
3.3	The expected signal yields and number of events in data.	67
3.4	Events break down by the data-taking periods and bins of $m_{\ell\ell\gamma}$ .	68
3.5	Effective width of the Higgs boson candidate mass distribution obtained from a gluon fusion MC signal sample.	70
3.6	Events per category in the muon channel after the selection.	73
3.7	Mean values of the $N_{Sig}^{FIT}/\sigma_{Sig}^{FIT}$ pull distributions in the muon channel.	81
3.8	Mean values of the $N_{Sig}^{FIT}/\sigma_{Bkg}^{FIT}$ pulls in the muon channel.	81
3.9	Mean values of the $N_{Sig}^{FIT}/\sigma_{Sig}^{FIT}$ pulls in the electron channel.	82
3.10	Mean values of the $N_{Sig}^{FIT}/\sigma_{Bkg}^{FIT}$ pulls in the electron channel.	82
3.11	Sources of the systematic uncertainties.	85
3.12	Per-event efficiency due to Muon ID.	89
B.1	Simulated samples of the background processes for $\mu\mu\gamma$ final state.	114



B.2	Number of events from data and MC backgrounds in the control and signal regions.	116
C.1	Event yield after full selection in VBF category.	119
D.1	Event yield after each selection criteria for data and signal with $m_{\text{H}} = 125 \text{ GeV}$ for $L = 19.7 \text{ fb}^{-1}$ in the muon channel.	122
D.2	Event yield after each selection criteria for data and signal with $m_{\text{H}} = 125 \text{ GeV}$ for $L = 19.7 \text{ fb}^{-1}$ in the electron channel.	137
D.3	Event yield after each selection criteria for data and $\text{H} \rightarrow (\text{J}/\psi)\gamma \rightarrow \mu\mu\gamma$ signal with $m_{\text{H}} = 125 \text{ GeV}$ for $L = 19.7 \text{ fb}^{-1}$ .	146

## List of Figures

1.1	Diagrams of the Higgs boson production processes at hadron colliders.	23
1.2	Predicted Higgs boson production cross sections vs $m_H$ at the LHC for $\sqrt{s} = 8$ TeV.	24
1.3	Cross sections of the SM processes at LHC.	25
1.4	Dominant diagrams for golden decay channels of the SM Higgs boson: a) $H \rightarrow ZZ^* \rightarrow 4\ell$ , and b) $H \rightarrow \gamma\gamma$ processes.	26
1.5	Invariant mass distributions of the Higgs boson candidates from $H \rightarrow ZZ^* \rightarrow 4\ell$ and $H \rightarrow \gamma\gamma$ analysis at CMS.	27
1.6	Diagrams contributing to $H \rightarrow \ell\ell\gamma$ process.	29
1.7	The invariant mass distribution of the two leptons from $H \rightarrow \ell\ell\gamma$ decay normalized by $\Gamma(H \rightarrow \gamma\gamma)$ in the electron and muon channels for $m_H = 125$ GeV.	31
1.8	Predicted Higgs boson decay branching fractions in SM.	34
1.9	Main diagrams contributing to the Higgs boson decay through a vector resonance, $H \rightarrow V\gamma \rightarrow (\ell\ell)\gamma$ .	36
2.1	The view of the CMS detector.	39
2.2	Schematic cross section through the CMS tracker.	40

		11
2.3	CMS tracker cross section view obtained by reconstructing the vertexes of the photon conversions, $\gamma \rightarrow e^+e^-$ .	41
2.4	The muon transverse momentum resolution as a function of the transverse momentum.	43
2.5	Average pileup distribution in pp data of 2012.	44
2.6	One of the CMS BPTX elements in the LHC tunnel.	46
2.7	A typical BPTX pulse.	46
2.8	Cogging measurement of BPTX versus time for a particular LHC fill. Average $z$ position of the beamspot as reconstructed by the tracking system.	47
3.1	Photon transverse momentum and $\eta$ distributions at generator level for $m_H = 125$ GeV.	50
3.2	Dilepton invariant mass distributions from $H \rightarrow \ell\ell\gamma$ Dalitz signal.	51
3.3	Event reconstruction efficiency as a function of dimuon invariant mass.	60
3.4	MVA response for signal and individual backgrounds (left), and combined background objects (right).	62
3.5	The invariant mass of the dilepton system in signal simulation for $m_H = 125$ GeV.	65
3.6	The invariant mass of the dilepton system in data for muon and electron channels.	66

		12
3.7	The $m_{\mu\mu\gamma}$ and $m_{ee\gamma}$ spectra in Dalitz analysis.	69
3.8	The $m_{\mu\mu\gamma}$ distribution for events within $2.9 < m_{\mu\mu} < 3.3$ GeV.	69
3.9	Reconstructed three-body mass distributions from the signal MC samples for $m_H = 125$ and $145$ GeV in muon and electron channels.	71
3.10	The $m_{\ell\ell\gamma}$ distributions in the muon channel for additional event categories.	73
3.11	Signal model fits.	75
3.12	Data events after the final selection and the fits of $m_{\mu\mu\gamma}$ distribution, in the range $110 < m_{\mu\mu\gamma} < 170$ GeV for three categories: <i>EB</i> , <i>EE</i> , <i>ml50</i> .	78
3.13	Examples of pull distribution obtained from the toy data with $m_H = 125$ GeV signal and the Exponential function as the true background model. Category 1 in muon channel.	79
3.14	Examples of the toy data generated from Exp, Bernstein $3^d$ order and Laurent functions.	80
3.15	Dimuon invariant mass distributions with different muon IDs.	87
3.16	Event efficiency associated with a specific muon ID selection vs dimuon invariant mass in MC signal sample.	88
3.17	$J/\psi \rightarrow \mu\mu$ peak and the fits in the $H \rightarrow J/\psi\gamma \rightarrow \mu\mu\gamma$ MC sample (left) and data events (right).	92

4.1	Exclusion upper limit on the $\mu$ -value for $H \rightarrow \mu\mu\gamma$ decay of a Higgs boson, in the muon channel.	96
4.2	Exclusion upper limit on the $\mu$ -value for $H \rightarrow \ell\ell\gamma$ decay of a Higgs boson, in the muon and electron channels.	97
4.3	The 95% CL exclusion limit on $\sigma(\text{pp} \rightarrow \text{H}) \times \mathcal{B}(\text{H} \rightarrow \ell\ell\gamma)$ , with $m_{\ell\ell} < 20 \text{ GeV}$ , for a Higgs-like particle, as a function of the mass hypothesis, $m_{\text{H}}$ .	98
4.4	Fit to the data events of $m_{\mu\mu\gamma}$ , where the plots correspond to one of the 7 bins in $m_{\mu\mu}$ .	100
4.5	Differential limit on the cross section times the branching fraction of a Higgs-like particle H, with $m_{\text{H}} = 125 \text{ GeV}$ ,	101
A.1	Distribution of polarization angle from $\text{J}/\psi \rightarrow \mu\mu$ and $\gamma^* \rightarrow \mu\mu$ .	112
B.1	$m_{\mu\mu\gamma}$ and $m_{\mu\mu}$ distributions in the Z peak control region.	114
B.2	Dimuon and photon $p_{\text{T}}$ distributions of events in the Z peak control region.	115
B.3	Distributions of jets' $p_{\text{T}}$ and $\Delta\eta$ in the Z peak control region.	116
B.4	$m_{\mu\mu\gamma}$ and $m_{\mu\mu}$ distributions in the SR, where the background normalization is taken from the CR.	116
B.5	Dimuon and photon $p_{\text{T}}$ and $p_{\text{T}}/m_{\mu\mu\gamma}$ distributions of the events in the signal region.	117
C.1	Input variables for the VBF selection in the muon channel.	118

C.2	Three body mass distribution in the VBF category.	120
D.1	Distributions of the $m_{\mu\mu}$ , after full selection in $110 < m_{\mu\mu\gamma} < 170$ GeV window.	123
D.2	Distributions of $\Delta R(\mu_1, \mu_2)$ for signal and data.	124
D.3	Distributions of $p_T^\gamma$ for signal and data.	125
D.4	Distributions of $\eta^\gamma$ for signal and data.	126
D.5	Distributions of the $p_T^{\mu\mu}$ .	127
D.6	Distributions of the $p_T^{\mu\mu}/m_{\mu\mu\gamma}$ .	128
D.7	Distributions of the $p_T^\gamma/m_{\mu\mu\gamma}$ .	129
D.8	Distributions of the leading muon $p_T$ .	130
D.9	Distributions of the sub-leading muon $p_T$ .	131
D.10	Distributions of the leading muon $\eta$ .	132
D.11	Distributions of the sub-leading muon $\eta$ .	133
D.12	Distributions of the $\Delta R_{\eta\phi}$ between the leading muon and the photon.	134
D.13	Resolutions of $m_{\mu\mu}$ , $m_{\mu\mu\gamma}$ and $\Delta R(\mu\mu)$ .	135
D.14	Resolution of $m_{\mu\mu}$ , in 6 bins of $m_{\mu\mu}$ : $0.2 - 0.5 - 1.0 - 2.0 - 4.0 - 9.0 - 20$ GeV.	136
D.15	Transverse momenta of the leading and trailing GSF tracks inside the Dalitz electron object.	138
D.16	Invariant mass and $\Delta R_{\eta\phi}$ of the two GSF tracks.	139
D.17	Photon distributions: $p_T, \eta, p_T/m_{e'\gamma}$ .	140

D.18	Dalitz electron object distributions: $p_T, \eta$ .	141
D.19	Dalitz electron object distributions: $p_T/m_{e'\gamma}, p_T^{e'}/p_T^\gamma$ .	142
D.20	Dalitz electron MVA ID input variables I.	143
D.21	Dalitz electron MVA ID input variables II.	144
D.22	Dalitz electron MVA ID input variables III.	145
D.23	$J/\psi \rightarrow \mu\mu$ peak and the three-body mass.	147
D.24	Distributions of the key variables from the $H \rightarrow (J/\psi)\gamma$ signal process.	148
D.25	Distributions of the key variables in data events after the full selection of the $H \rightarrow (J/\psi)\gamma$ search.	149
E.1	Expected limits vs $m_H$ with and without systematic uncertainties.	151

## CHAPTER 1

### Introduction

#### 1.1. Standard Model theory and Higgs Mechanism

The Standard Model (SM) theory of Particle Physics is one of the greatest achievements of human mind. Based on the principles of symmetry it provides a framework for describing the fundamental interactions between elementary particles. One of the successes of the theory was the prediction of  $W^\pm$  and  $Z^0$  bosons, the carriers of the *weak* interactions, which were discovered afterwards. Naively one expected those bosons to be mass-less, just as a photon is a mass-less carrier of the *electromagnetic* force, but they are not. In fact, quite the opposite, the mass of the  $W$  boson is now measured to be  $m_W = 80.4$  GeV, and the mass of the  $Z$  is  $m_Z = 91.2$  GeV. In order to explain the heavy weak bosons, a neat trick was invented by introducing a set of new scalar fields through what is now called the Englert-Brout-Higgs-Guralnik-Hagen-Kibble mechanism, or Higgs mechanism for short. The Higgs mechanism is of great relevance to the topic of this dissertation, hence I will describe it in more detail.

The SM is a Quantum Field Theory presented in the Lagrangian formalism. The Lorentz invariant Lagrangian density function of the SM (further in the text I will simply say, the Lagrangian) can be broken down into two parts:

$$(1.1) \quad \mathcal{L}_{SM} = \mathcal{L}_{QCD} + \mathcal{L}_{EW}.$$



The first term in (1.1) describes the interactions between quarks and gluons, and this theory is called Quantum Chromodynamics (QCD). The details of QCD is not discussed here, instead, one could refer to e.g. [1, 2] for this description. The second term in (1.1) represents the Electro-Weak theory (EW) and it is the term we are interested in.

The EW theory is based on the gauge group  $SU(2)_L \times U(1)_Y$ , with four gauge vector fields  $A^1, A^2, A^3, B$  and two coupling constants  $g$  and  $g'$ . The left-handed fermion fields transform as doublets under  $SU(2)_L$  group, while the right-handed fields transform as singlets under this group, that is:

$$(1.2) \quad \psi_i = \begin{pmatrix} \nu_i \\ \ell_i \end{pmatrix}_L \quad \begin{pmatrix} u_i \\ d_i \end{pmatrix}_L \quad (u_i)_R \quad (d_i)_R \quad (\ell_i)_R,$$

where  $i = 1, 2, 3$  for the three families of fermions. In addition, a complex doublet field  $\Phi$  is introduced in order to generate the masses of weak bosons and fermions:

$$(1.3) \quad \Phi \equiv \begin{pmatrix} \phi_1 \\ \phi_2 \end{pmatrix}$$

The EW Lagrangian can be written as:

$$(1.4) \quad \mathcal{L}_{EW} = \mathcal{L}_g + \mathcal{L}_\Phi + \mathcal{L}_f + \mathcal{L}_Y,$$

where the  $\mathcal{L}_g$  term describes the interactions of the  $A^i$  and  $B$  fields,  $\mathcal{L}_\Phi$  is a component for the scalar field,  $\mathcal{L}_f$  is the fermionic kinetic term, and  $\mathcal{L}_Y$  gives the Yukawa interaction between fermions and field  $\Phi$ .

In order to explain the Higgs mechanism, let's describe the bosonic plus scalar part of the theory in more detail. Its Lagrangian is given by:

$$(1.5) \quad \mathcal{L}_g + \mathcal{L}_\Phi = -\frac{1}{4}F_{\mu\nu}^a F_{\mu\nu}^a - \frac{1}{4}B_{\mu\nu}B_{\mu\nu} + (D_\mu\Phi)^\dagger D_\mu\Phi - \lambda \left( \Phi^\dagger\Phi - \frac{v^2}{2} \right)^2,$$

where:

$$(1.6) \quad F_{\mu\nu} = \partial_\mu A_\nu^a - \partial_\nu A_\mu^a + g\varepsilon^{abc}A_\mu^b A_\nu^c, \quad B_{\mu\nu} = \partial_\mu B_\nu - \partial_\nu B_\mu.$$

The co-variant derivative is defined as:

$$(1.7) \quad D_\mu\Phi = \partial_\mu\Phi - i\frac{g}{2}\tau^a A_\mu^a\Phi - i\frac{g'}{2}B_\mu\Phi,$$

where the Pauli matrices,  $\tau^a$ , act on the two-component field  $\Phi$ .

As stated above, the Lagrangian in (1.5) is invariant under  $SU(2) \times U(1)$  group, with the generators  $\mathbf{T}^a = \frac{1}{2}\boldsymbol{\tau}^a$  and  $\mathbf{Y} = \frac{1}{2}\mathbf{1}$ . This Lagrangian describes the interactions of the massless fields at high energies,  $E \gtrsim 1 \text{ TeV}$ . In order to describe the theory at low energies we need to determine the state of the system with minimal energy – the ground state, and rewrite the Lagrangian in terms of the excitations above the ground state. The fluctuations of the fields above that ground state correspond to particles.

Because the potential term of the scalar field in  $\mathcal{L}_\Phi$  is written in such a specific way (known as the Mexican hat potential), it produces degenerate ground states of the field. Following the conventions in [3], let's pick the ground state of the  $\Phi$  field as:

$$(1.8) \quad \Phi^{vac} = \begin{pmatrix} 0 \\ \frac{v}{\sqrt{2}} \end{pmatrix},$$

where  $v$  is a constant called Higgs vacuum expectation value, which has a value of 246 GeV.

Once the ground state of  $\Phi$  is chosen, the Lagrangian is no longer symmetric under  $SU(2) \times U(1)$ , but it remains symmetric under a new generator,  $\mathbf{Q}$ :

$$(1.9) \quad \mathbf{Q} = \begin{pmatrix} 1 & 0 \\ 0 & 0 \end{pmatrix},$$

which can also be expressed as:

$$(1.10) \quad \mathbf{Q} = \mathbf{T}^3 - \mathbf{Y}.$$

Here  $\mathbf{Q}$  is an generator of electric charge,  $\mathbf{T}^3$  is the generator of isospin and  $\mathbf{Y}$  is the hypercharge. Hence, the new Lagrangian is invariant under the new,  $U(1)_{EM}$  group, which is a sub-group of  $SU(2) \times U(1)_Y$ .

In order to write down the Lagrangian at low energies, we define the excitation of the field  $\Phi$  near its vacuum as:

$$(1.11) \quad \Phi = \begin{pmatrix} 0 \\ \frac{v}{\sqrt{2}} + \frac{\chi}{\sqrt{2}} \end{pmatrix},$$

where  $\chi(x)$  is a real scalar field. Substituting this in eq. (1.5) and carrying on the calculation (omitted here, see e.g. [3]), we can write the quadratic part of the Lagrangian as:

$$\begin{aligned}
(1.12) \quad \mathcal{L}^{(2)} = & -\frac{1}{2}\mathcal{W}_{\mu\nu}^+\mathcal{W}_{\mu\nu}^- + m_W^2 W_\mu^+ W_\mu^- - \frac{1}{4}F_{\mu\nu}F_{\mu\nu} - \\
& -\frac{1}{4}\mathcal{Z}_{\mu\nu}\mathcal{Z}_{\mu\nu} + \frac{m_Z^2}{2}Z_\mu Z_\mu + \frac{1}{2}(\partial_\mu\chi)^2 - \frac{m_\chi^2}{2}\chi^2,
\end{aligned}$$

where:

$$\mathcal{W}_{\mu\nu}^\pm = \partial_\mu W_\nu^\pm - \partial_\nu W_\mu^\pm, \quad F_{\mu\nu} = \partial_\mu A_\nu - \partial_\nu A_\mu, \quad \mathcal{Z}_{\mu\nu} = \partial_\mu Z_\nu - \partial_\nu Z_\mu$$

and the fields  $A^1, A^2, A^3, B$  are transformed into  $W^\pm, Z$  and  $A$  according to:

$$\begin{aligned}
(1.13) \quad W^\pm &= \frac{1}{\sqrt{2}}(A^1 \mp iA^2), \\
Z &= -B \sin \theta_W + A^3 \cos \theta_W, \\
A &= B \cos \theta_W + A^3 \sin \theta_W.
\end{aligned}$$

Here the  $\theta_W$  is called weak mixing angle and defined as:

$$\tan \theta_W = \frac{g'}{g}.$$

The masses in (1.12) are composed from parameters,  $g, g', \lambda$  from the original Lagrangian (1.5) and the Higgs vacuum expectation value,  $v$ , as follows:

$$(1.14) \quad m_W = \frac{gv}{2}, \quad m_Z = \frac{\sqrt{g^2 + g'^2}v}{2}, \quad m_\chi = \sqrt{2\lambda}v.$$

The fields in (1.13) now correspond to the well known, massive  $W^\pm$  and  $Z^0$  bosons, and the photon,  $\gamma$ . Hence, the constructed theory with Lagrangian (1.12) is a combined theory

of the electromagnetic and weak interactions. This, in essence, describes the Electroweak symmetry breaking and the Higgs mechanism. One of the consequences and the prediction of the theory is the existence of a new particle, corresponding to the scalar field  $\chi$ , called the Higgs boson, with the mass,  $m_\chi \equiv m_H = \sqrt{2\lambda}v$ .

As recent as 2012, a new particle with the mass of 125 GeV was discovered at the Large Hadron Collider (LHC) by the ATLAS<sup>†</sup> and CMS<sup>‡</sup> experiments ([4, 5]). This particle is now widely accepted as *the* Higgs boson predicted by the Standard Model, which is another success of the theory. Experimentally, the Higgs boson is studied at the LHC by colliding protons at very high energies, which enables its production, and detecting the decay products of the boson. In Section 1.2 I describe the physics mechanisms by which the Higgs boson is produced at the LHC and in Section 1.3 I give an overview of its decays and experimental sensitivity of detecting them.

Since the SM is fully constrained (there are no free parameters), the properties of the Higgs boson, including its decay branching fractions, are predicted by the theory. Hence, any deviations from these predictions, observed experimentally, would point out to the New Physics, also called the Physics Beyond the Standard Model (BSM). It is understood that the SM theory, in general, is not complete and deviations from it are expected. Therefore, a search for such deviations is now a priority of the LHC experiments. There are no evidence for any deviations found so far. In that respect the rare decays of the Higgs boson are interesting, because, while they are rare in the SM, they could be enhanced one way or another within the BSM models. The main topic of my dissertation is a search for the  $H \rightarrow \gamma^* \gamma \rightarrow \ell \ell \gamma$  rare decay, described in Section 1.4.

---

<sup>†</sup>A Toroidal LHC Apparatus

<sup>‡</sup>Compact Muon Solenoid

## 1.2. Higgs boson production at the LHC

The LHC [6] is a proton-proton synchrotron collider build in the underground circular tunnel at the European Organization for Nuclear Research (CERN) on the border between France and Switzerland. It has a circumference of 27 km and was designed to accelerate the proton beams to the energies of 7 TeV per beam. That energy however has not been reached yet and the main collision data, taken in 2011 and 2012, are with 3.5 and 4 TeV per beam, i.e. 7 and 8 TeV center-of-mass energy.

At high energies of the LHC, a proton is no longer a composite of just the  $uud$  quarks, but it consists of a spectrum of gluons and quarks of all flavors – commonly called *partons*. The relative composition of those partons and their dependence of the proton energy are described by the Parton Distribution Functions (PDF) [7]. It turns out that at the LHC the dominant component of the proton is a gluon, thus the hard collision processes are dominated by the gluon-gluon interactions.

In order to understand the production of the Higgs boson, we need to know its coupling to other particles of the SM. In the Lagrangian of the eq. (1.12) only quadratic terms are kept. If we were to expand it, the three-particle interactions with weak bosons emerge in the full Lagrangian, and the coupling of these interactions is given by:

$$(1.15) \quad g_{HVV} = \frac{2m_V^2}{v}.$$

Therefore, the interactions of the  $W$  and  $Z$  bosons with the Higgs boson is proportional to their mass squared. Furthermore, the fermionic part of the  $\mathcal{L}_{EM}$  was omitted in (1.5). Once included, after the symmetry breaking described in Sec. 1.1, the interaction term of

the fermions with the Higgs field is given by:

$$(1.16) \quad \mathcal{L}_F = \sum_f \frac{gm_f\chi}{2M_W} \bar{\psi}_f \psi_f,$$

which means that the coupling of the Higgs boson to the fermions is proportional to the mass of a fermion:

$$(1.17) \quad g_{Hf\bar{f}} = \frac{gm_f}{2M_W} = \frac{m_f}{v}.$$

The leading Higgs boson production processes at hadron colliders are shown in Fig. 1.1. The relative production rates for a SM Higgs boson with  $m_H = 125 \text{ GeV}$  at  $\sqrt{s} = 8 \text{ TeV}$  at the LHC are: gluon-gluon fusion (ggF) – about 88%; Vector Boson Fusion (VBF) – 7%; associated production with a Z or W boson (VH) – 5%; and  $t\bar{t}$  fusion (ttH) – 0.4%. Figure 1.2 shows the production cross sections versus a Higgs boson mass.

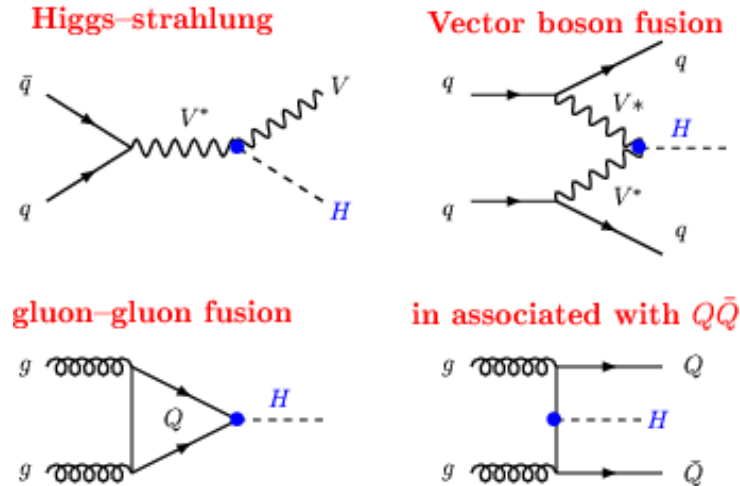


Figure 1.1. Diagrams of the Higgs boson production processes at hadron colliders, image from [8].

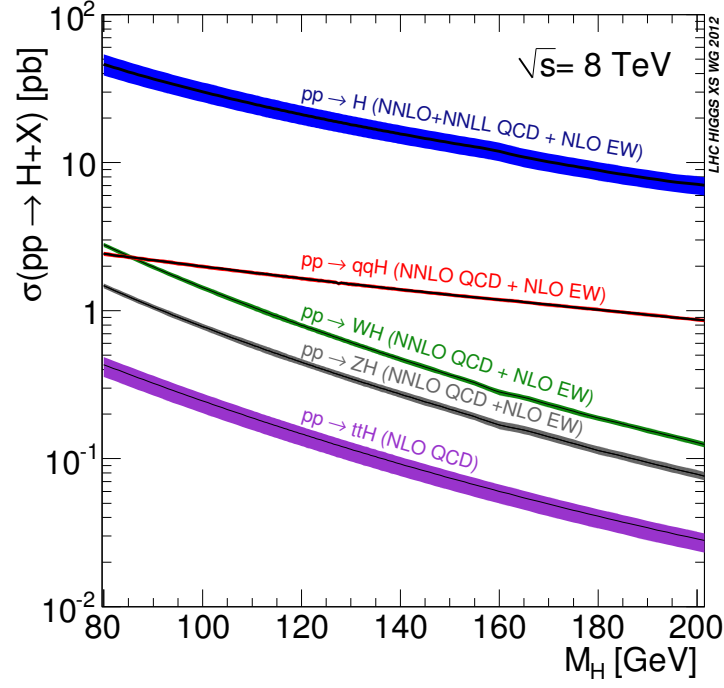


Figure 1.2. Predicted Higgs boson production cross sections vs  $m_H$  at the LHC for  $\sqrt{s} = 8$  TeV.

Even though the gluon fusion process dominates, there are experimental advantages of the VBF and VH modes: tagging events with extra particles and reducing the backgrounds. In the VH production, the tag is based on the leptonic decays of the Z/W bosons: missing transverse energy due to neutrinos ( $E_T^{miss}$ ), and/or the presence of charged leptons –  $W(\ell\nu)H$ ,  $Z(\ell\ell)H$  and  $Z(\nu\nu)H$ . Let me note the branching ratios of those decays:  $\mathcal{B}(W \rightarrow \ell\nu) \approx 10\%$ ,  $\mathcal{B}(Z \rightarrow \ell\ell) \approx 3.4\%$  per lepton,  $\mathcal{B}(Z \rightarrow \nu\nu) \approx 20\%$ . The typical VBF tag requires an event with two jets with large invariant mass,  $m_{jj} > 500$  GeV, and large angular separation between the jets.



### 1.2.1. Background processes

Since the protons are collided at the LHC, the QCD part of the SM presented in eq. (1.1) becomes quite relevant in experimental observation of the Higgs boson and studying its properties. The total inelastic cross section at  $\sqrt{s} = 7$  TeV is measured to be around 60 mb [9, 10] and the QCD processes contribute a large part to this cross section. Therefore, it is the dominant background, which we have to deal with when searching for new processes and particles. The Electroweak SM processes also have large cross sections, compared to the Higgs boson production. For example, the cross sections for the  $W$  or  $Z$  bosons production are on the order of  $10^4 - 10^5$  pb, while the total Higgs boson production cross section is about 20 pb. Figure 1.3 shows a summary of the cross sections of the EW processes measured by CMS [11].

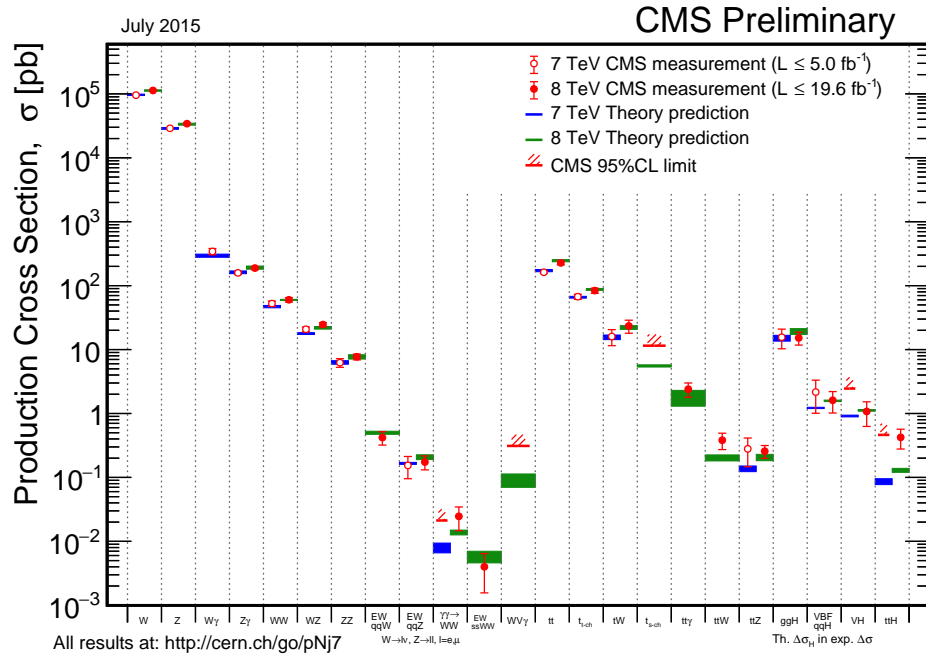


Figure 1.3. Cross sections of the SM processes at LHC.

### 1.3. Decays of the Higgs boson

Based on eqs. (1.15) and (1.17), and taking into account phase space constraint, the largest decay rates of the Higgs boson for  $m_H = 125 \text{ GeV}$  arise from  $H \rightarrow b\bar{b}$  and  $H \rightarrow WW$ . These two processes, however, are difficult from the experimental point of view. In the first one, the final state involves hadronic jets, hence it is overwhelmed by background processes, like  $pp \rightarrow b\bar{b}$ . The second process involves jets as well, from  $W \rightarrow qq$  decay, or missing energy from neutrinos in  $W \rightarrow \ell\nu$  mode, which makes it impossible to reconstruct accurately the invariant mass of the Higgs boson candidate. The two most sensitive decay channels at the LHC are  $H \rightarrow ZZ \rightarrow 4\ell$  and  $H \rightarrow \gamma\gamma$ , the so called *golden channels* of the Higgs boson decays. The leading diagrams for these processes are shown in Figure 1.4. The Higgs boson couples to the Z boson directly but it does not couple to the photon, therefore the  $H \rightarrow \gamma\gamma$  process occurs via loops as shown in Fig. 1.4b. The dominant contributions in the loops come from the heaviest candidates: top quark and W boson (which contribute to the total amplitude with opposite signs). Figure 1.5 shows the key plots from the two *golden channel* analyses at CMS – the invariant mass distributions

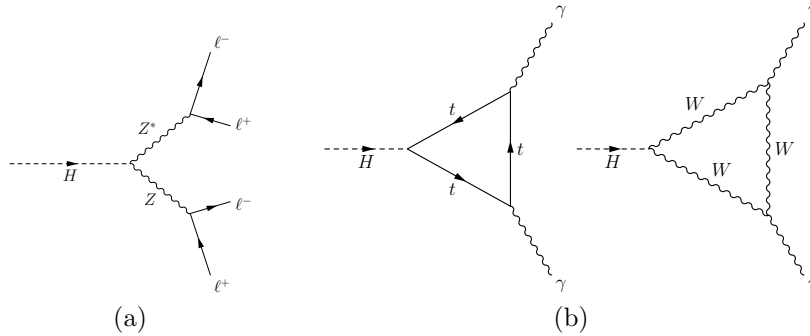


Figure 1.4. Dominant diagrams for golden decay channels of the SM Higgs boson: a)  $H \rightarrow ZZ^* \rightarrow 4\ell$ , and b)  $H \rightarrow \gamma\gamma$  processes.

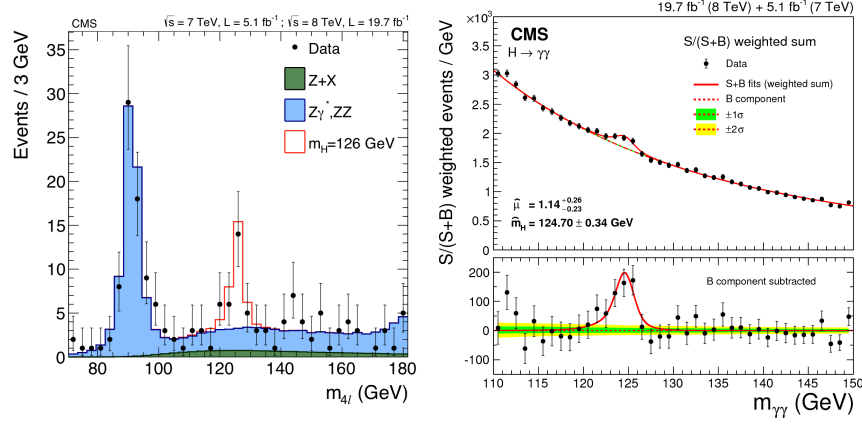


Figure 1.5. Invariant mass distributions of the Higgs boson candidates from  $H \rightarrow ZZ^* \rightarrow 4\ell$  and  $H \rightarrow \gamma\gamma$  analysis at CMS.

of the Higgs boson candidates. Clear resonant peaks at the same mass,  $m_H = 125$  GeV, manifest the existence of the particle. Surely, many other modes are searched for by both ATLAS and CMS. Particularly, a search for the direct decays of the Higgs boson to fermions [12] shows the evidence for  $H \rightarrow \tau\tau$  decay, with the same  $m_H$ .

Overall, the observed decay rates of the Higgs boson are in-line with the predictions of the SM. Now it is the time to look for the rare processes, such as  $H \rightarrow V\gamma \rightarrow \ell\ell\gamma$ , for example, where  $V = \gamma^*, Z, J/\psi$  or  $\Upsilon$ . While these processes are rare in the SM, they could be enhanced by the presence of the New Physics. In the next section I describe the  $H \rightarrow \ell\ell\gamma$  process in more detail.

#### 1.4. Higgs boson decays into $\ell^+\ell^-\gamma$ final state

The decay of the Higgs boson into  $\ell\ell\gamma$  final state ( $\ell = \mu$  or  $e$ ), although rare, provides valuable information to enhance our understanding of the properties of the newly discovered boson. The dominant contributions to this decay come from the loop-induced processes,  $H \rightarrow \gamma^*\gamma$  and  $H \rightarrow Z\gamma$ , where one of the photons or a Z boson converts internally into two leptons, as illustrated in diagrams (a),(b),(c) of Fig. 1.6. These are the so-called *loop* or *pole* diagrams, where the *pole* refers to the  $\gamma^*$  and  $Z^*$  poles. There are also contributions from the processes represented by box-diagrams, which do not have the  $Z^*/\gamma^*$  poles (d,e,f), and the final-state radiation (FSR) in the  $H \rightarrow \ell\ell$  process (g). Other contributions include  $H \rightarrow V(q\bar{q})\gamma \rightarrow \ell\ell\gamma$  processes, where  $V$  denotes a vector meson (like  $J/\psi$  and  $\Upsilon$ ) that decays to  $\ell\ell$  pair. This process is discussed in Sec.1.4.2.

The calculation of the various contributions to the  $H \rightarrow f\bar{f}\gamma$  decay (here  $f$  denotes all kinematically accessible charged fermions, i.e.  $f = e, \mu, \tau, u, d, s, c, b$ ) were demonstrated in Refs. [13, 14, 15, 16]. The phase space of the  $f\bar{f}\gamma$  final state can be naturally parametrized by the invariant mass,  $m_{f\bar{f}}$ , of the outgoing fermions. Hence, the decay rate of this process can be expressed as a function of  $m_{f\bar{f}}$  as:

$$(1.18) \quad \frac{d\Gamma(H \rightarrow f\bar{f}\gamma)}{dm_{f\bar{f}}^2} = \frac{1}{256\pi^3 m_H^3} \int_{(m_{f\bar{f}}^2)_{min}}^{(m_{f\bar{f}}^2)_{max}} dm_{f\bar{f}}^2 \sum_{spin} |\mathcal{M}|^2,$$

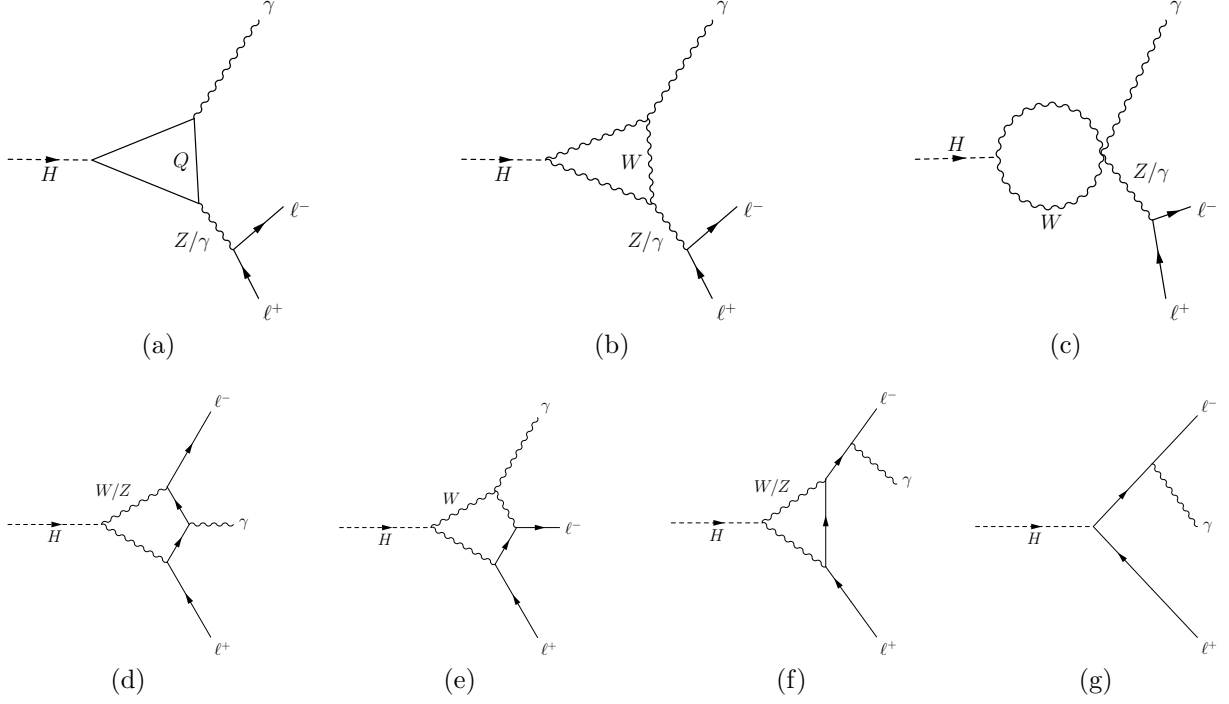


Figure 1.6. Diagrams contributing to  $H \rightarrow \ell\ell\gamma$  process. The contributions from diagrams (a), (b), and (c) dominate. Higher order contributions from diagrams (d), (e) and (f) are negligible. The final-state radiation of  $H \rightarrow \ell\ell$  decay (g) is important at high dilepton invariant mass.

where the limits of integration are given by

$$(1.19) \quad (m_{\bar{f}\gamma}^2)_{min} = m_f^2 + \frac{1}{2}(m_H^2 - m_{\bar{f}f}^2) \left( 1 - \sqrt{1 - \frac{4m_f^2}{m_{\bar{f}f}^2}} \right),$$

$$(1.20) \quad (m_{\bar{f}\gamma}^2)_{max} = m_f^2 + \frac{1}{2}(m_H^2 - m_{\bar{f}f}^2) \left( 1 + \sqrt{1 - \frac{4m_f^2}{m_{\bar{f}f}^2}} \right).$$

The full matrix-element,  $\mathcal{M}$ , can be expressed as:

$$(1.21) \quad \sum_{spin} |\mathcal{M}|^2 = C(\mathcal{A}_\gamma, \mathcal{A}_Z, \mathcal{B}_Z, \mathcal{B}_W),$$

where  $\mathcal{A}_\gamma$ ,  $\mathcal{A}_Z$  and  $\mathcal{B}_Z$ ,  $\mathcal{B}_W$  are the amplitudes for the pole and box diagrams of Fig. 1.6, respectively. The full expressions for these amplitudes, as well as the matrix elements of eq. (1.21), are given in Ref. [13]. It was found that the contribution from the box diagrams is quite small. If only the *pole* diagrams are considered, the expression for  $\frac{d\Gamma}{dm_{\bar{f}f}^2}$  (i.e.  $m_{\bar{f}f}$  distribution) can be written as:

$$(1.22)$$

$$\begin{aligned} \frac{d\Gamma}{dm_{\bar{f}f}^2} = & \frac{\alpha^4 m_W^2}{(8\pi)^3 \sin^6 \theta_W m_H^3} \left[ \sin^4 \theta_W \frac{|\mathcal{A}_\gamma(m_{\bar{f}f}^2)|^2}{m_{\bar{f}f}^2} + 2 \sin^2 \theta_W v_f \Re \left( \frac{\mathcal{A}_\gamma(m_{\bar{f}f}^2) \mathcal{A}_Z^*(m_{\bar{f}f}^2)}{(m_{\bar{f}f}^2 - m_Z^2) - i m_Z \Gamma_Z} \right) + \right. \\ & + \frac{(1 + v_f^2) m_{\bar{f}f}^2 |\mathcal{A}_Z(m_{\bar{f}f}^2)|^2}{(m_{\bar{f}f}^2 - m_Z^2)^2 + m_Z^2 \Gamma_Z^2} \Big] (m_H^2 - m_{\bar{f}f}^2) \sqrt{1 - \frac{4m_f^2}{m_{\bar{f}f}^2}} \left[ (m_H^2 + 2m_f^2 - m_{\bar{f}f}^2)^2 + \right. \\ & \left. \left. + \frac{1}{3} (m_H^2 - m_{\bar{f}f}^2)^2 \left( 1 - \frac{4m_f^2}{m_{\bar{f}f}^2} \right) \right] \right] \end{aligned}$$

The results of the calculations are illustrated in Fig. 1.7 for the muon and electron channels (i.e.  $f = \mu$  or  $e$ ). These distribution reveal a few features of the  $H \rightarrow \ell\ell\gamma$  process. First of all, there is an obvious peak at the  $Z$  mass, which arises from the  $Z^* \rightarrow \ell\ell$  pole contribution. Both ATLAS and CMS collaborations have performed a search for  $H \rightarrow Z\gamma \rightarrow \ell\ell\gamma$  decay, with  $m_{\ell\ell} > 50 \text{ GeV}$  selection [18, 19]. The results are consistent with the SM predictions and the upper limits on the  $\sigma/\sigma_{SM}$  are set at  $\sim 10 \times \text{SM}$ . Secondly, there is a peak at small  $m_{\ell\ell}$ , which is due to the photon pole  $\gamma^* \rightarrow \ell\ell$ . It is important to point out that there is no singularity at low mass. This can be seen from the integration limits in eq. (1.19), which become equal at  $m_{\ell\ell}^2 = 4m_\ell^2$ , hence the integral in eq. (1.18) vanishes. The effect due to the photon pole is significant, and compatible with the pole

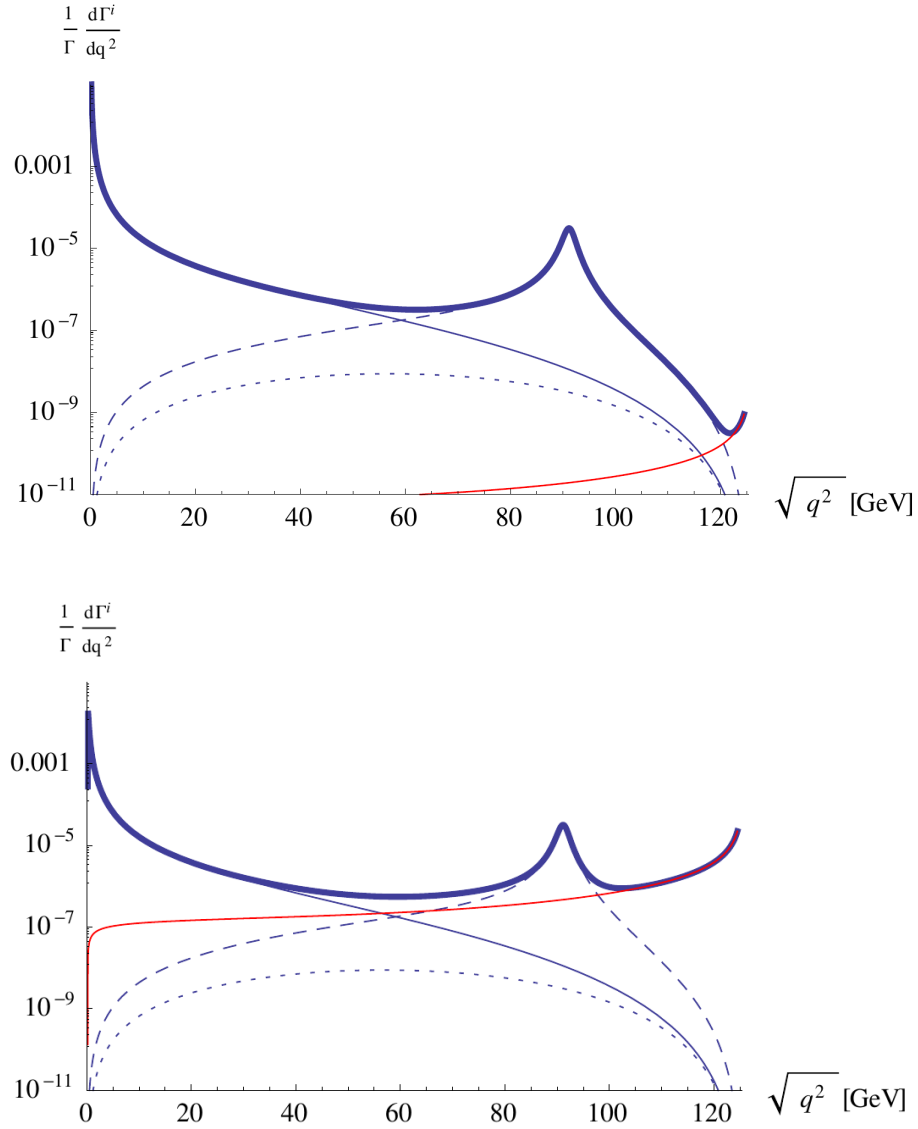


Figure 1.7. The invariant mass distribution of the two leptons from  $H \rightarrow \ell\ell\gamma$  decay normalized by  $\Gamma(H \rightarrow \gamma\gamma)$  in the electron (top) and muon (bottom) channels for  $m_H = 125$  GeV. The thin solid line denotes the contribution from the  $\gamma^*$  pole diagrams, the dashed line shows the contribution from the  $Z^*$  pole diagrams, the red line denotes the contribution of the tree diagrams of  $H \rightarrow \mu\mu$  with FSR photon, and the dotted line is the contribution from the four-point box diagrams. The thick blue line gives the total sum. Figures from Ref. [17].

at  $Z$  mass, hence one expects to obtain a similar search sensitivity. In fact, as a result of this dissertation, the sensitivity of the  $H \rightarrow \gamma^* \gamma$  channel for the SM Higgs boson search turns out to be higher than of the  $H \rightarrow Z^* \gamma$  channel. The small contributions of the box diagrams are also illustrated in the Fig. 1.7. They are usually neglected in the simulation by the Monte Carlo (MC) programs. Finally, at high invariant mass,  $m_{\ell\ell} > 100 \text{ GeV}$ , one observes a rise of the curve. It comes from the FSR process,  $H \rightarrow \ell\ell \rightarrow \ell\ell\gamma$ , which strength is proportional to the lepton mass ( $g_{Hf\bar{f}} = \frac{m_f}{v}$ ). Thus, it is more pronounced in the muon channel than in the electron channel. The  $H \rightarrow \mu\mu$  process by itself is crucial for understanding the SM, and, of course, it has been searched for by the ATLAS and CMS [20, 21]. The upper limits on the  $\sigma/\sigma_{SM}$  are set at  $\sim 8$  times the SM prediction, consistent with the expected sensitivity.

In the above description I am differentiating the individual processes  $H \rightarrow \gamma^* \gamma$  and  $H \rightarrow Z\gamma$ , with the final state of  $\ell\ell\gamma$ . Strictly speaking this is not correct, since these processes are ill-defined from the gauge invariance point of view. They interfere and have contributions from the non-pole diagrams, which are also mentioned. Therefore one should refer to the total  $H \rightarrow \ell\ell\gamma$  process instead. Nevertheless, I will continue using this notation, but one has to keep that subtlety in mind (see also discussion in Ref. [16]). Experimentally, the separation of the two processes is achieved by selecting on the dilepton invariant mass. For the main subject of this dissertation only the  $m_{\ell\ell} < 20 \text{ GeV}$  part of the  $H \rightarrow \gamma^* \gamma \rightarrow \ell\ell\gamma$  spectrum is considered. However, sometimes, a looser requirement of  $50 \text{ GeV}$  is used, as explicitly mentioned. This decay process is often referred to as *Higgs Dalitz decay* in analogy to the  $\pi_0 \rightarrow e^+e^-\gamma$  decay, induced by an internal conversion of one of the photons, and named after the physicist Richard Dalitz.



#### 1.4.1. Details on the $H \rightarrow \gamma^* \gamma \rightarrow \ell \ell \gamma$ process

The expected rate of the  $H \rightarrow \gamma^* \gamma \rightarrow f f \gamma$  decay for a Higgs boson mass of 125 GeV is about 7–10% of the rate of  $H \rightarrow \gamma \gamma$  decay [22, 23], while it is 54% for  $H \rightarrow Z \gamma$  process [24]. If only leptonic decay channels are considered, the corresponding fractions become:

$$\frac{\Gamma(H \rightarrow \gamma^* \gamma \rightarrow e e \gamma)}{\Gamma(H \rightarrow \gamma \gamma)} \sim 3.5\%, \quad \frac{\Gamma(H \rightarrow \gamma^* \gamma \rightarrow \mu \mu \gamma)}{\Gamma(H \rightarrow \gamma \gamma)} \sim 1.7\% \quad \text{and} \quad \frac{\Gamma(H \rightarrow Z \gamma \rightarrow \ell \ell \gamma)}{\Gamma(H \rightarrow \gamma \gamma)} \sim 2.3\%.$$

The full information of the Higgs boson production cross section [24], and the branching fraction of the Dalitz decay mode into leptonic final states is presented in Table 1.1. The branching fractions depend on the upper cut on the  $m_{\ell \ell}$  and on the mass of the lepton, as emphasized previously. The numbers reported in Table 1.1 are given for two selections:  $m_{\ell \ell} < 20$  and  $< 50$  GeV. The branching fractions are obtained using MCFM 6.6 program [25], where only the *poll* diagrams are included. MCFM reports the values of  $\sigma \cdot \mathcal{B}$ , the cross section times the branching fraction, without the NNLO corrections to the Higgs

$m_H$	$\sigma(\text{pp} \rightarrow H + X), \text{ fb}$				$\mathcal{B}(H \rightarrow \ell \ell \gamma) \times 10^{-5}$			
	gg	VBF	ZH	WH	$m_{\ell \ell} < 50 \text{ GeV}$		$m_{\ell \ell} < 20 \text{ GeV}$	
					$\mu \mu \gamma$	$e e \gamma$	$\mu \mu \gamma$	$e e \gamma$
120	20.9	1.65	0.47	0.81	3.73	7.75	3.21	7.25
125	19.3	1.58	0.42	0.70	3.83	8.07	3.33	7.45
130	17.9	1.51	0.37	0.62	3.83	8.01	3.28	7.37
135	16.6	1.45	0.33	0.54	3.64	7.62	3.09	6.97
140	15.4	1.39	0.29	0.48	3.32	6.87	2.82	6.42
145	14.5	1.33	0.26	0.42	2.89	5.96	2.48	5.62
150	13.6	1.28	0.23	0.37	2.35	4.87	2.00	4.49

Table 1.1. Cross sections of the SM Higgs boson production at  $\sqrt{s} = 8$  TeV for each production channel; and the branching fraction of the  $H \rightarrow \ell \ell \gamma$  decay process in the muon and electron channels, for  $m_{\ell \ell} < 50$  GeV and  $m_{\ell \ell} < 20$  GeV.

boson production. This correction is about  $\sim 1.16$ , almost independent of the  $m_H$ , and taken into account in the values given in Table 1.1. Muons in the MCFM calculations are assumed to be massless. Once their mass is taken into account, it changes the low  $m_{\ell\ell}$  part of the spectra and results in the reduction of the branching fraction by  $\sim 3\text{--}4\%$ , which is also taken into account in Table 1.1.

For comparison with other processes, Fig. 1.8 shows the branching fractions of the Higgs boson decays into various relevant final states. The  $\mathcal{B}(H \rightarrow \ell\ell\gamma)$  for the Dalitz mode is shown for  $m_{\ell\ell} < 20 \text{ GeV}$ . Even though the Dalitz decay rate is the smallest, there are certain advantages of searching for this process:

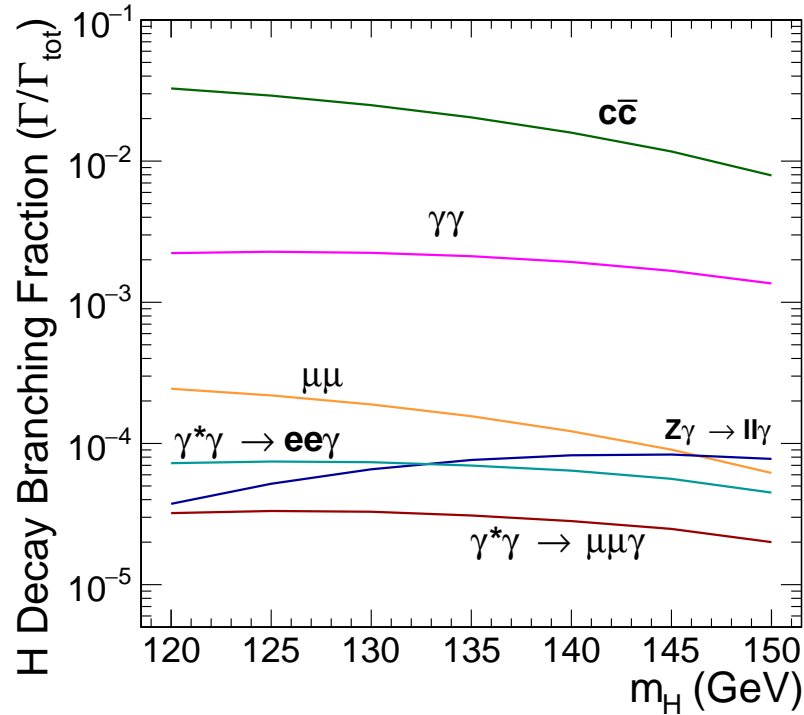


Figure 1.8. Predicted Higgs boson decay branching fractions of selected processes. Here the  $\mathcal{B}(H \rightarrow \ell\ell\gamma)$  is shown with  $m_{\ell\ell} < 20 \text{ GeV}$  requirement.

- It is sensitive to new physics (NP) beyond the standard model (BSM) via loops. That is, the existence of a new particle could enhance the rate of this decay. In the absence of the NP, it gives an extra handle on the measurement of the Higgs boson couplings. Particularly, it offers a reliable determination of the primary vertex, which becomes useful in *high pile-up* environment (see Sec. 2.1.2), while, e.g. in the  $H \rightarrow \gamma\gamma$  decay the vertex would become harder to reconstruct.
- The  $H \rightarrow \gamma^*\gamma \rightarrow ee\gamma$  decay is distinct from the  $H \rightarrow \gamma\gamma$  followed by a conversion of a photon to an  $e^+e^-$  pair in the detector. Experimentally, however, these two processes may be difficult to distinguish if the photon conversions are not properly identified. Hence, one process can become a background for another, and it is important to understand their relative contributions for the crucial measurement of the  $H \rightarrow \gamma\gamma$  decay.
- It consists of non-trivial angular correlations that could result in a forward-backward asymmetry in the presence of the NP, manifested itself through CP violation in  $H_{\bar{f}f}$  effective coupling [17, 26]. This feature provides an additional test for the SM and the properties of the Higgs boson.

It may be also of an interest to mention that the same effective coupling, with inverted diagrams, is involved in  $e^+e^- \rightarrow H\gamma$  process, which is possibly accessible at the future linear electron-positron colliders. The calculation of this process was performed in Ref. [27].

In this dissertation the search for  $H \rightarrow \gamma^*\gamma \rightarrow \ell\ell\gamma$  is presented. The search is performed in muon and electron channels, for the Higgs boson mass range between 120 and 150 GeV, and it is described in Section 3. All results are based on proton-proton collision

data recorded in 2012 with the CMS detector at the LHC at  $\sqrt{s} = 8 \text{ TeV}$ , corresponding to the integrated luminosity of  $19.7 \text{ fb}^{-1}$ .

#### 1.4.2. $H \rightarrow V\gamma \rightarrow \ell\ell\gamma$

In addition to the Higgs Dalitz decay, the result for the  $H \rightarrow (J/\psi)\gamma \rightarrow \mu\mu\gamma$  search, at  $m_H = 125 \text{ GeV}$ , will be presented in Section 4.5. This decay, allows us to test the Higgs boson couplings to the charm quark, as suggested in Refs. [28, 29]. It is a promising way to measure this coupling at the LHC. There are two mechanisms through which the  $H \rightarrow V\gamma \rightarrow \ell\ell\gamma$  decay occurs (see the diagrams in Fig. 1.9):

- A direct process, where the Higgs boson couples to a  $Q\bar{Q}$  pair ( $Q = c, b$ ), with an FSR radiation of a photon. In this process the  $q\bar{q}$  pair hadronizes into a vector meson ( $V = J/\psi, \Upsilon$ ), which decays to a pair of leptons.
- An indirect process, where the Higgs boson decays through a usual  $t/W$  loop to a  $\gamma\gamma^*$  pair with a subsequent decay of the  $\gamma^*$  to the vector meson, through the  $Q$ -loop.

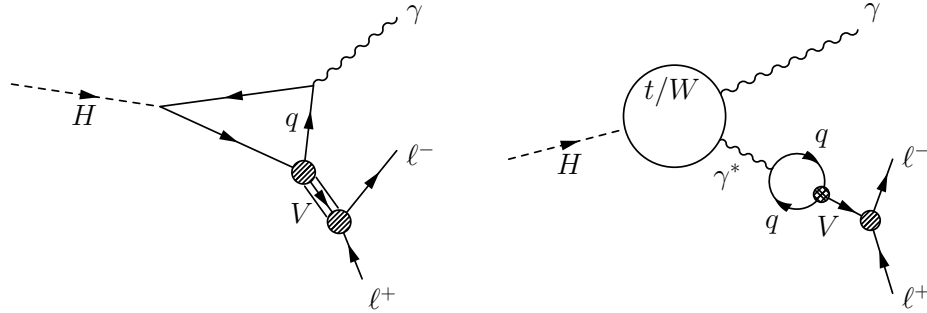


Figure 1.9. Main diagrams contributing to the Higgs boson decay through a vector resonance,  $H \rightarrow V\gamma \rightarrow (\ell\ell)\gamma$ .

It was calculated in Ref. [29] that the contribution from the indirect process is in fact larger, and the interference between the two processes is destructive. In the case of  $\Upsilon$ , this interference is nearly complete. The widths of these decays are expected to be:

$$(1.23) \quad \Gamma_{J/\psi\gamma} = 1.42 \times [(1.0 \pm 0.017)\kappa_\gamma - (0.087 \pm 0.012)\kappa_c]^2 \times 10^{-8} \text{ GeV},$$

$$(1.24) \quad \Gamma_{\Upsilon\gamma} = 0.11 \times [(1.0 \pm 0.009)\kappa_\gamma - (1.058 \pm 0.045)\kappa_b]^2 \times 10^{-8} \text{ GeV},$$

where  $\kappa_\gamma$ ,  $\kappa_c$  and  $\kappa_b$  parametrize the strength of the  $H\gamma\gamma$  and  $HQQ$  couplings. Taking the total width of the Higgs boson at  $\Gamma_H = 4.20 \text{ MeV}$  and  $\kappa_\gamma = \kappa_c = \kappa_b = 1$ , they obtain:

$$(1.25) \quad \mathcal{B}_{SM}(H \rightarrow J/\psi + \gamma) = 2.79_{+0.16}^{-0.15} \times 10^{-6},$$

$$(1.26) \quad \mathcal{B}_{SM}(H \rightarrow \Upsilon + \gamma) = 8.4_{+19.3}^{-8.2} \times 10^{-10}.$$

ATLAS has performed the search for these decays, see Ref. [30] for their results. First estimates of the bounds on the  $HQQ$  couplings are discussed in Ref. [31], based on the ATLAS and CMS results.

## CHAPTER 2

# Experimental Apparatus

## 2.1. Compact Muon Solenoid

Compact Muon Solenoid (CMS) [32] is a general purpose detector located at one of the four points of the LHC ring, where the beams collide. It was designed to reconstruct most of the outgoing particles of the collision: charged leptons and hadrons, neutral hadrons, and photons. A detailed description of the CMS detector can be found in Ref. [32], below I provide only a short overview of the detector. The CMS coordinate system is oriented such that the  $x$ -axis points to the center of the LHC ring, the  $y$ -axis points vertically upward and the  $z$ -axis along the anticlockwise-beam direction. The azimuthal angle  $\phi$  is measured in the  $xy$  plane, with  $\phi = 0$  along the positive  $x$  axis and  $\phi = \pi/2$  along the positive  $y$  axis and the radial coordinate in this plane is denoted by  $r$ . The polar angle  $\theta$  is defined in the  $rz$  plane and pseudorapidity variable is defined as  $\eta = -\ln[\tan(\theta/2)]$ . The momentum component transverse to the beam direction, denoted by  $p_T$ , is computed from the  $x$ - and  $y$ -components, and the transverse energy is defined as  $E_T = E \sin \theta$ . The central feature of the CMS apparatus is a superconducting solenoid of 6 m internal diameter, providing a magnetic field of 3.8 T. The magnet largely determines the geometry of the detector, see Fig. 2.1. Within the superconducting solenoid volume are a silicon pixel and strip tracker, a lead tungstate ( $\text{PbWO}_4$ ) crystal electromagnetic calorimeter (ECAL), and a brass and scintillator hadron calorimeter (HCAL), each composed of a

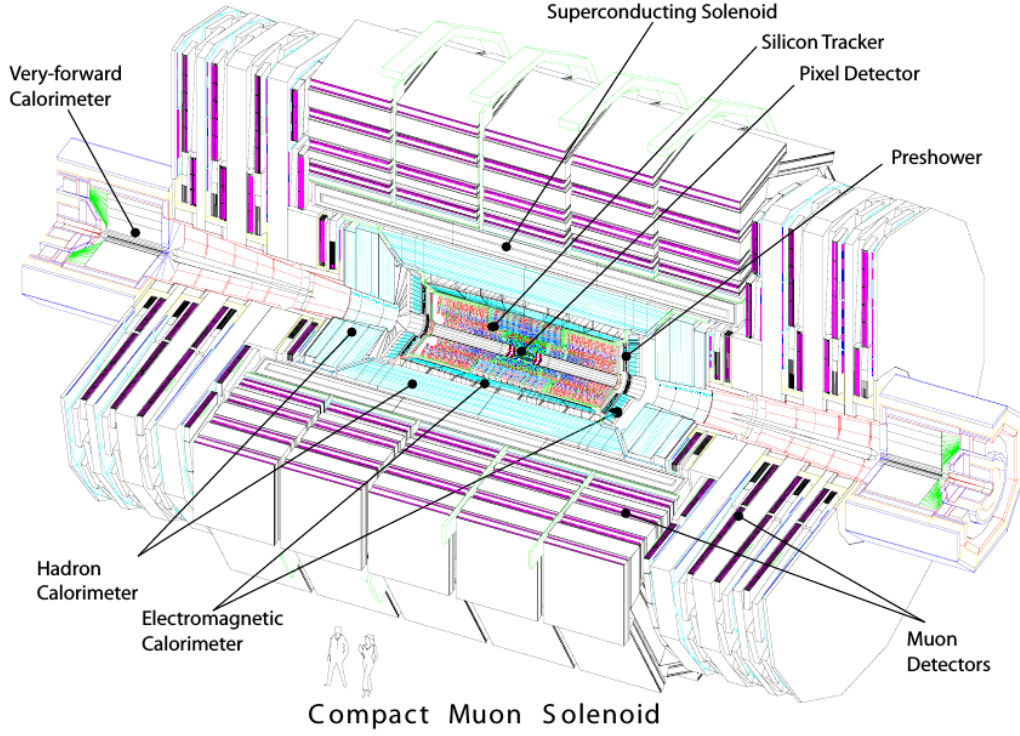


Figure 2.1. The view of the CMS detector.

barrel and two endcap sections. The muon system is composed of the gas-ionization detectors embedded in the steel flux-return yoke outside the solenoid. Extensive forward calorimetry complements the coverage provided by the barrel and endcap detectors. The detector is nearly hermetic, i.e. covers almost full  $4\pi$  open angle. This allows to perform energy balance measurements in the plane transverse to the beam direction, thus provide a measurement of missing transverse energy,  $E_T^{\text{miss}}$ , associated to neutrinos or other weakly interacting particles.

The silicon tracker measures charged particles within the pseudorapidity range  $|\eta| < 2.5$ . It consists of 1440 silicon pixel and 15 148 silicon strip detector modules. The inner pixel detector is housed in a cylindrical volume of 1 m long and 30 cm in diameter. It

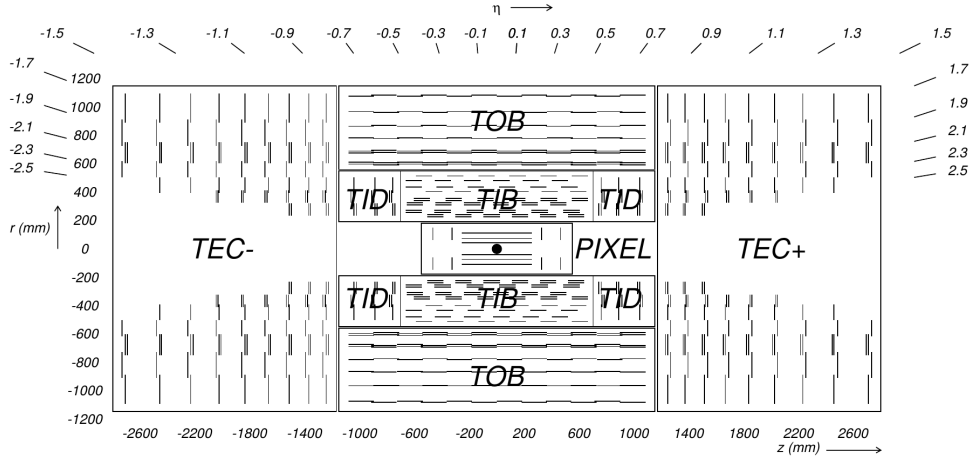


Figure 2.2. Schematic cross section through the CMS tracker. Each line represents a detector module. Double lines indicate back-to-back modules which deliver stereo hits.

consists of about 66 M pixels of size  $100 \times 150 \mu\text{m}$ , distributed over three barrel layers and two endcap disks. With analogue signal interpolation, a hit resolution of  $10 \times 20 \mu\text{m}$  is achieved. The silicon strip tracker is divided into four sub-detectors: outer barrel, inner barrel, inner disk, and endcap. All active components are housed in a cylindrical volume of length 5.4 m and diameter of 2.4 m. Modules laying within  $r < 60 \text{ cm}$  have a strip pitch between 80 and  $120 \mu\text{m}$ , which is increased to  $\sim 120$  to  $200 \mu\text{m}$  for  $r > 60 \text{ cm}$ . A schematic view of the tracker system is shown in Fig. 2.2.

Material of the tracking volume itself affects the overall event topology and reconstruction through electron bremsstrahlung, photon conversions and nuclear interactions. It also affects the trajectories of charged tracks because of multiple scattering and energy loss. Photon conversions are used by CMS as “radiographic” measurements of the tracker material [33] by reconstructing the vertex position of the two electrons from  $\gamma \rightarrow e^+e^-$ , as illustrated in Fig. 2.3. On this figure the LHC beam pipe is also clearly visible. In fact, the beam pipe is a physical boundary between the  $\gamma^* \rightarrow ee$  process, where the photon



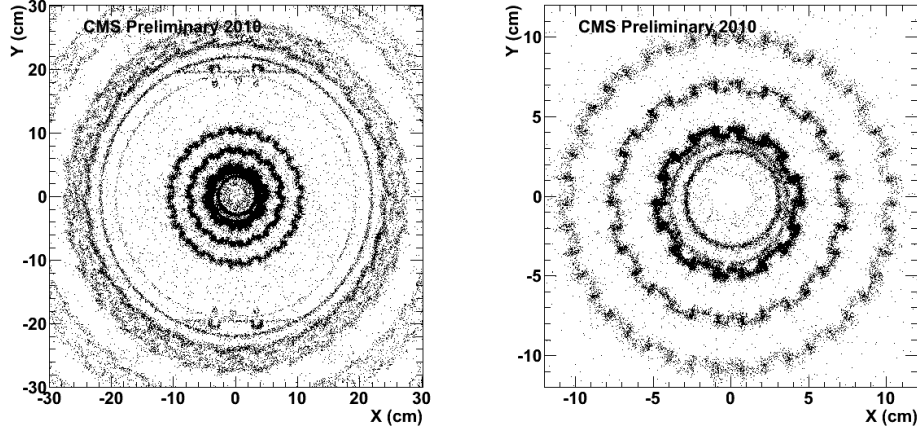


Figure 2.3. CMS tracker cross section view obtained by reconstructing the vertices of the photon conversions,  $\gamma \rightarrow e^+e^-$ .

converts internally, and the  $\gamma \rightarrow ee$ , where the conversion occurs on the beam pipe or in the detector. This information is used in the analysis to separate the two processes.

Large magnetic field allows for a precise measurement of the tracks momenta. For non-isolated particles of  $1 < p_T < 10$  GeV and  $|\eta| < 1.4$ , the track resolutions are typically 1.5% in  $p_T$ , and 25–90 (45–150)  $\mu\text{m}$  in the transverse (longitudinal) impact parameter [34]. For a muon with  $p_T = 100$  GeV the resolution on the  $p_T$  measured in the tracker alone is about 2% in the barrel region. The pixel and tracker systems also play an important role in the reconstruction of the primary interaction vertices, and identification of the converted photons by recovering the electron track, see Sec. 3.4.

The ECAL is distributed in a barrel region  $|\eta| < 1.48$  and two endcaps that extend up to  $|\eta| = 3$ . A lead and silicon-strip preshower detector is located in front of the ECAL endcaps in order to improve the identification of  $\pi^0 \rightarrow \gamma\gamma$  events. Initial calibration of the calorimeter was done with the test beam and the achieved resolution can be parametrized as follows:

$$(2.1) \quad \left(\frac{\sigma}{E}\right)^2 = \left(\frac{0.028}{\sqrt{E}}\right)^2 + \left(\frac{0.12}{E}\right)^2 + (0.003)^2.$$

Further calibration of the calorimeter is performed with collision data, using  $Z \rightarrow ee$  events, where electrons are reconstructed as photons, and  $Z \rightarrow \mu\mu\gamma$  events, where the photon is radiated off the muon in the final state.

The HCAL surrounds the ECAL volume and covers the region  $|\eta| < 3$ . Iron forward calorimeters with quartz fibers, read out by photomultipliers, extend the detector coverage up to  $|\eta| = 5$ . The resolution of HCAL obtained after the calibration with the test beam is:

$$(2.2) \quad \begin{aligned} \left(\frac{\sigma}{E}\right)^2 &= \left(\frac{0.9}{\sqrt{E}}\right)^2 + (0.045)^2 \quad \text{in Barrel and Endcap;} \\ \left(\frac{\sigma}{E}\right)^2 &= \left(\frac{1.72}{\sqrt{E}}\right)^2 + (0.09)^2 \quad \text{in Forward.} \end{aligned}$$

With collision data the calibration of HCAL is performed using isolated charged tracks, with momenta between 40 and 50 GeV. The momentum measurement of the tracks is obtained in the tracker with high accuracy. When a (hadron) track reaches the calorimeters, it deposits all of its energy, thus allowing to calibrate HCAL using the energy measured in the tracker [35]. For this purpose only the tracks with small energy deposits in ECAL (minimum ionizing particles) are selected.

Muons penetrate the whole detector with minimal interaction and are identified in gas-ionization detectors. Figure 2.4 shows the improvement of the momentum resolution of muons on top of the tracker system. Before the start of the LHC, the alignment and

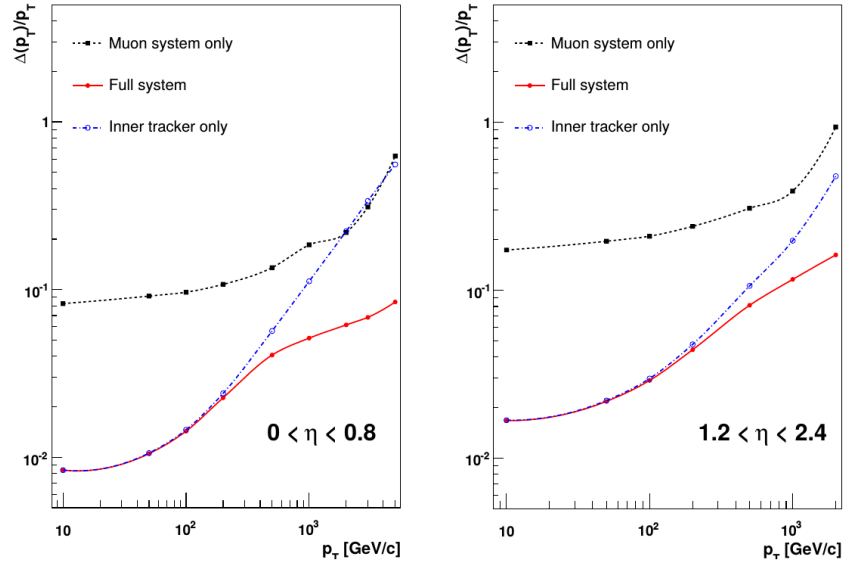


Figure 2.4. The muon transverse momentum resolution as a function of the transverse momentum ( $p_T$ ) using the muon system only, the inner tracking only, and both. Left panel:  $|\eta| < 0.8$ , right panel:  $1.2 < |\eta| < 2.4$

calibration of the muon sub-detectors was performed with data, using atmospheric muons reaching the detector. Then, with collision data the momentum of the muons is calibrated using  $J/\psi \rightarrow \mu\mu$  and  $Z \rightarrow \mu\mu$  events.

### 2.1.1. Trigger

Two-tier online trigger system is implemented in CMS in order to reduce the rate of the events collected on tape. The first tier, called the Level-1 (L1) trigger, composed of custom hardware processors, uses the basic information from the calorimeters and muon detectors to select the most interesting events in a fixed time interval of less than  $4\mu\text{s}$ . If the event satisfies the L1 selection criteria, it is processed further; if not, then it is discarded. The L1 trigger reduces the event rate to  $\sim 100\text{ kHz}$ . At the second tier, called the high level trigger (HLT), more sophisticated selection is performed. It combines the

kinematic information of multiple trigger objects (particle candidates), in order to keep the most interesting events for the offline analysis. Total HLT rate is about 100 Hz, i.e. about  $\sim 100$  events per second is saved on tape for further analysis.

### 2.1.2. Pile-up

Each bunch of the LHC beam contains more than  $10^{10}$  protons in it, hence there is a large probability for multiple p-p interactions per bunch. In 8 TeV collisions, there was on average 21 interactions per bunch crossing, shown in Fig. 2.5. This phenomena is called *pile-up* and it results in the reconstructing of multiple primary interaction vertices. Luckily, the signal processes that are interesting for physics analysis are so rare that they never happen twice in the same bunch crossing. Thus, only one primary vertex is chosen per event, which is most likely to correspond to the hardest interaction, see Sec. 3.4. However, the extra interactions spoil the purity of the event reconstruction and this needs to be taken into account at the analysis level.

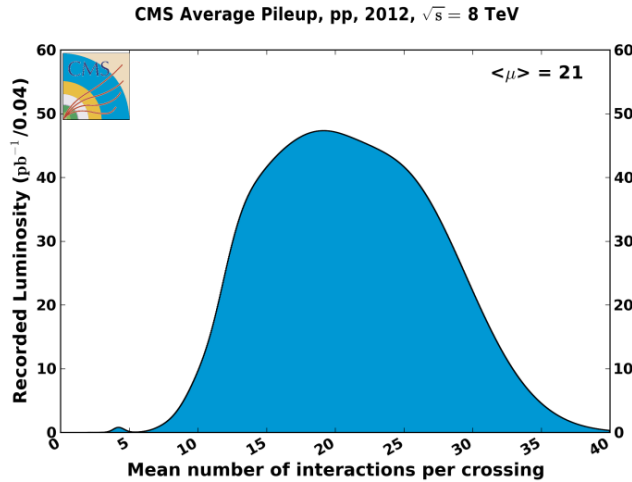


Figure 2.5. Average pileup distribution in pp data of 2012.

## 2.2. Beam timing measurement at CMS

For measuring the position of the beam in the beam pipe, there are 1032 beam position monitors (BPM) installed around the LHC. The majority of the BPMs (860 of the 1032) are built out of four electrostatic button pick-up electrodes that are installed symmetrically around the beam pipe. A more detailed description of the BPMs can be found in Refs. [36, 37, 38]. When a proton bunch travels around the pipe, it induces a mirror current of free-moving electrons on the surface of the pipe. Traveling over the electrode surface of the button pick-up, this current gives rise to a signal on the button surface. This signals from the BPM provides an opportunity for a precise measurement of the timing and structure of the incoming beams, as well as the characteristics of individual bunches.

The two BPMs closest to the interaction point of each LHC experiment are reserved for the timing measurements and are called the Beam Pick-up Timing eXperiment (BPTX) detectors, which for CMS are located approximately 175 m on either side of the interaction point. One BPM element contains four pickup buttons located in a single vertical plane and orientated  $90^\circ$  with respect to each other, see Fig. 2.6. For the BPTX use at CMS all four buttons are connected in parallel to provide the maximum signal. Each pickup only sees a single beam.

When the signal arrives at the counting room at CMS, it is split into four equal copies. One copy is dedicated to the trigger and enters the BPTX logic crate. The other signals are available for monitoring with high sampling oscilloscopes. The signals serve a dual purpose; they are used both for monitoring of timing related beam conditions and for the L1 trigger. Figure 2.7 shows a typical BPTX pulse signal. Its characteristics are a steep

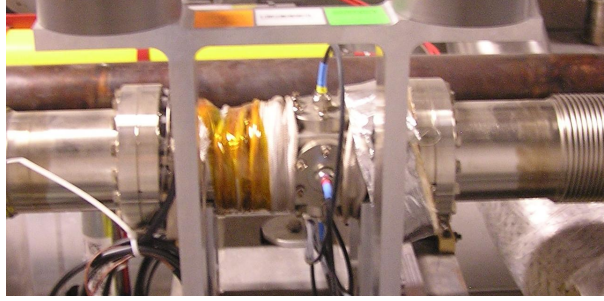


Figure 2.6. One of the CMS BPTX elements in the LHC tunnel. Three of the four button connectors (blue) can be seen.

leading flank, followed by a shallow trough after which the signal slowly returns to the baseline.

The BPTX trigger electronics is implemented in NIM modules. The key module of the system is the Ortec's constant fraction discriminator (CFD). This module is designed to operate at 200 MHz frequency [39]. For BPTX purposes it experiences 40 MHz frequency

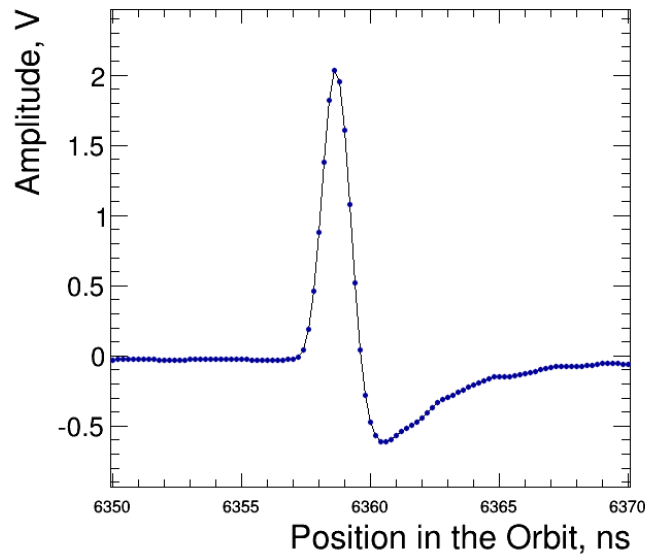


Figure 2.7. A typical BPTX pulse as seen on the oscilloscope. The markers represent the measured points.

during nominal 25 ns bunch spacing beams, or 20 MHz with 50 ns bunch spacing. The threshold of the discriminator is manually adjustable on the module. As the intensity of the beam changes one may need to adjust the threshold accordingly in order to maintain 100% efficiency. The plain NIM BPTX(1,2) trigger signals are taken to various logic units in order to provide an AND, an OR and exclusive AND signals. Then the signals are sent to the L1 Trigger. The logical AND of the two BPTX signals is used to gate other triggers (both at the L1 and HLT) with collidable beam crossings.

Upon injection of the beam into LHC an estimate of the beam crossing position near the IPs can be obtained from a BPTX based timing measurement. As mentioned above the copies of the analog BPTX signals are also fed into the oscilloscopes (LeCroy WR 104MXi-A [40]). The timing measurements is then performed on those oscilloscopes. The time resolution of the BPTX-based timing is better than 0.1 ns, which is sufficient to distinguish between adjacent RF buckets (2.5 ns). The result of this measurement,

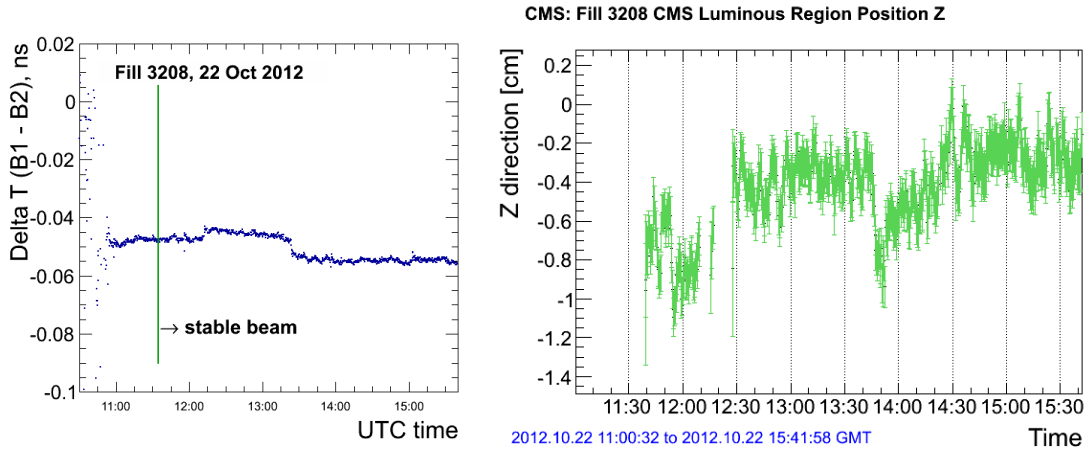


Figure 2.8. Cogging measurement of BPTX versus time for a particular LHC fill (left); Average  $z$  position of the beamspot as reconstructed by the tracking system (right). The correlations between the two indicate the sensitivity of the beamspot to the moving beams.

the relative time difference between the two BPTX signals in nanoseconds, is published through the LHC data interchange protocol (DIP) [41] and picked up for publication on the LHC Vistar web page [42] as *BPTX: deltaT of IP (B1 - B2)* and displayed for the world to see. This is commonly referred to as the *cogging measurement* (Fig. 2.8), and provides a first estimate of the beam interaction position along  $z$  direction.

At the time of writing this dissertation the Run-2 of the LHC operation is started. The BPTX system of CMS is one of the first to see the beams from the LHC. Normal operation of the BPTX detector is now re-established with beams and shows excellent performance. New developments of the electronics and software for the system are also ongoing. First of all, the NIM based logic is to be replaced with a programmable VME board, the V1495 module by CAEN, which would do the analog logic of the two beams and provide signals to the L1 trigger system. Secondly, the oscilloscope based measurement is to be replaced with the hardware, using the newly developed ADC uTCA board.



## CHAPTER 3

### Physics Analysis: Search for $H \rightarrow \ell\ell\gamma$

#### 3.1. Features of the decay

Before going into details of the event reconstruction and selection, the basic features of the  $H \rightarrow \gamma^*\gamma \rightarrow \ell\ell\gamma$  final state are described.

Due to a heavy Higgs boson, the  $\gamma$  and  $\gamma^*$  from its decay are highly energetic (boosted), and predominantly central, see Fig. 3.1. Therefore, a stringent selection on their  $p_T$ , as well as  $\Delta R$ , is possible, and those requirements reject a large part of the backgrounds. Because the  $\gamma^*$  is boosted, the two leptons from its decay are anti-correlated in their transverse momenta. Also because of the boost and low dilepton invariant mass of the  $\gamma^* \rightarrow \ell\ell$  decay, the leptons in the final state are very close to each other in  $\Delta R_{\eta,\phi}$ . In the case of electron channel, this feature prevents us from reconstructing two electrons: they are merged into a single shower in the ECAL and can not be resolved. In order to overcome this problem a dedicated identification criteria was developed, based on the multivariate analysis (MVA) technique, described in Section 3.4.6. In the muon channel the situation is better: both muons can be well reconstructed. However, a *loose* identification (ID) criteria has to be used in order to increase the reconstruction efficiency. The invariant mass,  $m_{\ell\ell}$ , of the two leptons is close to the photon pole mass,  $m_{\gamma^*} = 2m_\ell$ , for the majority of events, see Fig. 3.2. Hence, in order to isolate the contribution from the Dalitz decay, the main analysis is limited to the phase space with  $m_{\ell\ell} < 20$  GeV.

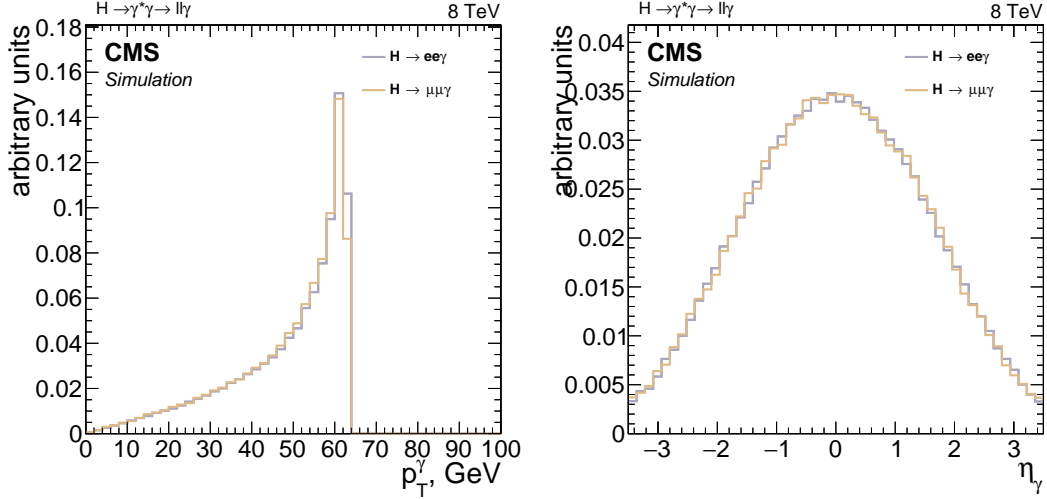


Figure 3.1. Photon transverse momentum and  $\eta$  distributions at generator level for  $m_H = 125$  GeV. The  $p_T$  distribution illustrates the fact that the photon is energetic (peaked at 60 GeV). From the  $\eta$  distribution we can see that the signal events are produced predominantly centrally in  $\eta_\gamma$ .

### 3.2. Simulated samples

The first challenge of the analysis was to produce a proper simulation of the signal samples, in order to obtain the description of the Higgs boson signal events to be used in the search. The samples for Dalitz signal are produced at the leading-order of QCD, using the MADGRAPH 5 matrix-element generator with anomalous Higgs Effective coupling model [43, 44]. The output events of MADGRAPH are further showered with PYTHIA 6.426 [45] and undergo the full CMS detector simulation with GEANT 4. The samples are generated for the gluon-gluon and vector bosons fusion, and associated production with a vector boson production processes. Associated Higgs boson production with a  $t\bar{t}$  pair is ignored due to its small contribution. The kinematic distributions of the MADGRAPH samples were also cross-checked with the output of MCFM program and found to be consistent. The parton distribution function (PDF) set used to produce these samples is

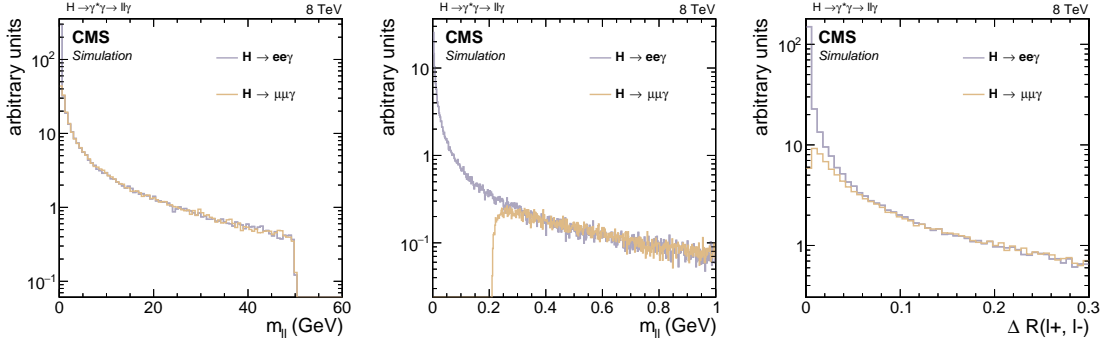


Figure 3.2. The dilepton invariant mass distributions from  $H \rightarrow \ell\ell\gamma$  Dalitz signal (Left: full range; Middle: zoomed into the low mass region, which shows the effect of non-zero lepton masses). Right:  $\Delta R(\ell_1, \ell_2)$  distribution. All plots are made at generator level for  $m_H = 125$  GeV, before FSR.

CTEQ6L1 [46]. The pile-up events are also introduced in the simulation using a sample of the minimum bias events. The simulated samples are often referred to as Monte Carlo (MC) samples and I will use those terms interchangeably in the later text.

In order to obtain the correct results for the Dalitz signal process one has to take into account the mass of the leptons:  $m_e = 0.000511$  GeV,  $m_\mu = 0.1057$  GeV. The masses make a difference to the natural cut-off from  $\gamma^* \rightarrow \ell\ell$  process at  $m_{\ell\ell} > 2m_\ell$ , which can be seen in Fig. 3.2 of  $m_{\ell\ell}$  and  $\Delta R(\ell\ell)$  distributions..

A sample for  $H \rightarrow (J/\psi)\gamma$  signal is produced using PYTHIA 8 generator [47]. The polarization of the  $J/\psi$  is not correctly taken into account by the generator. Therefore, this sample is additionally reweighted to simulate 100% polarization of the  $J/\psi$ , see Appendix A.

The SM Higgs boson production cross sections are taken from Ref. [24]. The branching fractions for the  $H \rightarrow \gamma^*\gamma \rightarrow \ell\ell\gamma$  signal processes are estimated at the next-to-leading order (NLO) in QCD using MCFM, as described in Sec. 1.4. Using those numbers one

Table 3.1. Number of signal events within  $m_{\ell\ell} < 50$  GeV, and  $m_{\ell\ell} < 20$  GeV expected to be produced at  $\sqrt{s} = 8$  TeV with  $19.7 \text{ fb}^{-1}$ , before acceptance and reconstruction effects, in gluon fusion process.

$m_H$	$m_{\ell\ell} < 50 \text{ GeV}$		$m_{\ell\ell} < 20 \text{ GeV}$	
	$H \rightarrow \mu\mu\gamma$	$H \rightarrow ee\gamma$	$H \rightarrow \mu\mu\gamma$	$H \rightarrow ee\gamma$
120	15.0	30.7	12.9	23.9
125	14.4	29.4	12.2	22.6
130	13.3	27.2	11.3	20.9
135	11.7	23.9	10.0	18.5
140	9.9	20.3	8.4	15.5
145	8.2	16.6	6.9	12.7
150	6.3	12.8	5.4	9.9

can estimated the total number of signal events produced with  $19.7 \text{ fb}^{-1}$  of integrated luminosity, which are given in Table 3.1 for the gluon fusion process. Only part of those events could be reconstructed, when all of the final state particles have large enough momenta to reach the detector volume. This fraction, called the signal event acceptance,  $a = \frac{N^{sel}}{N^{tot}}$ , depends on the selection. With the basic selection<sup>†</sup> applied to the generator level particles, an acceptance of  $\sim 55\%$  is obtained, i.e. about half of the events from the Table 3.1 could be reconstructed in the detector. Efficiencies of the reconstruction will be discussed in Section 3.4 after the event reconstruction is described.

For the  $H \rightarrow (J/\psi)\gamma$  decay the branching fraction is taken from Ref. [29], where for a SM Higgs boson the prediction is  $\mathcal{B}(H \rightarrow (J/\psi)\gamma) = (2.8 \pm 0.2) \times 10^{-6}$ .

The pile-up event simulation does not match exactly the pile-up conditions in data. Hence, in order to achieve a better agreement, the simulated samples are reweighted based on the number of simulated primary vertices. Furthermore, the reconstruction efficiencies of the physics object do not match exactly between the data and simulation. In some

---

<sup>†</sup>Typical selection consists of a photon with  $p_T > 30$  GeV in  $|\eta^\gamma| < 2.5$  and two leptons with  $p_T^{\ell_1} > 23$  GeV and  $p_T^{\ell_2} > 4$  GeV, both in  $|\eta^\mu| < 2.4$ , see Section 3.5 for the motivation of these choices.

cases this is also accounted for by reweighting of the sample, in other cases a systematic uncertainty is applied, see Section 3.7 for details. Overall, the effect of the reweightings is smaller than 2% on the predicted yield of the signal. The energy and momentum resolution of the photon and muons in simulated events are also corrected to match the resolution in data.

### 3.3. Background Estimation and Analysis Strategy

The background estimation is data-driven: it is determined from a fit to the data distribution of the reconstructed three-body invariant mass,  $m_{\ell\ell\gamma}$ . The strategy of the analysis is to use that fit as the background model and search for the signal peaks on top of it.

#### 3.3.1. Background Composition: Muon Channel

The main irreducible background is the Drell–Yan (DY) initial state radiation (ISR) process:  $pp \rightarrow \gamma^* + \gamma \rightarrow \mu\mu\gamma$ , with low dilepton invariant mass. There is also a contribution from FSR events off the Z-peak:  $pp \rightarrow \gamma^*/Z \rightarrow \mu\mu\gamma$ . However the contribution from the second process has to be small in the signal region, which is far from the Z-mass peak,  $m_{\mu\mu\gamma} > 110$  GeV.

Major reducible background is a DY+jet process,  $pp \rightarrow \gamma^* + jet \rightarrow \mu\mu + jet$ , where a *jet* in the final state is mis-identified as a photon.

Even though the background estimation in the analysis is data-driven, I have also made an attempt to describe the backgrounds with MC simulation, see Appendix B. It is however not used in the analysis because the agreement between data and simulation

was found not satisfactory. The reason for the disagreement is due to the difficulty to implement the jet matching between the NLO process generated by MADGRAPH and its showering by PYTHIA [48]. Nevertheless from this study, I can conclude that  $DY+\gamma$  consists of approximately 40% of the total background, while  $DY+jet$  is the rest, about 60%.

### 3.3.2. Background Composition: Electron Channel

Backgrounds in the electron channel are like in the muon channel, but in addition, there is a large contribution from QCD events due to the topology of two very close electrons, and from  $\gamma\gamma$  events, where one of the photons converts in the detector material or on the beam pipe. See Section 3.4.6 for details. The fit to the three-body mass distribution in data is used as the background model.

### 3.4. Event reconstruction

#### 3.4.1. Primary vertex

As mentioned in Section 2.1.2 multiple pp-interactions occur per-collision. A deterministic annealing algorithm [34] is used to identify all vertices from those interactions. A vertex with the highest scalar sum of the  $p_T^2$  of its associated tracks is chosen as *the* primary vertex (PV). The PV must have the reconstructed longitudinal position ( $z$ ) within 24 cm of the geometric center of the detector and the transverse position ( $x$ - $y$ ) within 2 cm of the beam interaction region.

#### 3.4.2. Particle-Flow algorithm

The global event reconstruction (also called particle-flow (PF) event reconstruction [49, 50]) is based on reconstructing and identifying each single particle with an optimized combination of the information from all subdetectors. In this process, the identification of the particle type (photon, electron, muon, charged hadron, neutral hadron) plays an important role in the determination of the particle direction and energy. Photons are identified as ECAL energy clusters not linked to the extrapolation of any charged particle trajectory to the ECAL. Electrons are identified as a primary charged particle track and potentially many ECAL energy clusters corresponding to this track extrapolation to the ECAL and to possible bremsstrahlung photons emitted along the way through the tracker material. Muons are identified as a track in the central tracker consistent with either a track or several hits in the muon system, associated with an energy deficit in the calorimeters. Charged hadrons are identified as charged particle tracks neither identified as electrons, nor as muons. Finally, neutral hadrons are identified as HCAL energy clusters

not linked to any charged hadron trajectory, or as ECAL and HCAL energy excesses with respect to the expected charged hadron energy deposit.

The energy of photons is directly obtained from the ECAL measurement, corrected for zero-suppression effects. The energy of electrons is determined from a combination of the track momentum at the main interaction vertex, the corresponding ECAL cluster energy, and the energy sum of all bremsstrahlung photons attached to the track. The energy of muons is obtained from the corresponding track momentum. The energy of charged hadrons is determined from a combination of the track momentum and the corresponding ECAL and HCAL energy, corrected for zero-suppression effects and for the response function of the calorimeters to hadronic showers. Finally, the energy of neutral hadrons is obtained from the corresponding corrected ECAL and HCAL energy.

Based on the PF candidates it is useful to construct isolation variables as follows. For an object reconstructed with transverse momentum,  $p_{T0}$ , in a given direction,  $(\eta_0, \phi_0)$ , one defines a cone in  $\eta - \phi$  plane, with radius  $R_0$ , such that  $\Delta R_{\eta\phi} \equiv \sqrt{(\eta - \eta_0)^2 + (\phi - \phi_0)^2} < R_0$ . One then calculates the transverse energy of all particle candidates within this cone, relative to  $p_{T0}$ , separating them by type:  $I_{ch} = \sum_{pf}^{\Delta R < R_0} p_T^{charged}/p_{T0}$  for charged hadrons,  $I_{neu} = \sum p_T^{neu}/p_{T0}$  for neutral hadrons, and  $I_{pho} = \sum p_T^{pho}/p_{T0}$  for the photons. Of course, the original object, for which the isolation variable is constructed, is excluded from the sums. The energy of the particles associated to the pile-up interaction vertex is also measured,  $I_{PU} = \sum p_T^{PU}/p_{T0}$ . Furthermore, the average energy associated to pile-up particles,  $\rho$ , is calculated. All these isolation variables are used in the identification criteria (ID) of the photons and muons, as discussed below.



### 3.4.3. Photons

The photons are reconstructed using the electromagnetic calorimeter and their energy is obtained from a sum of ECAL crystals. A set of crystals with energy deposition are combined into clusters. The arrays of clusters, which contain all of the energy of a photon are called superclusters. In the barrel section of the ECAL, an energy resolution of about 1% is achieved for unconverted or late-converting photons in the tens of GeV energy range. The remaining barrel photons have a resolution of about 1.3% up to a pseudorapidity of  $|\eta| = 1$ , rising to about 2.5% at  $|\eta| = 1.4$ , see Ref. [51].

After the basic reconstruction in ECAL, the identification criteria are applied in order to better separate photons from jets and electrons. The observables used in the photon ID are: the ratio of the energy in the hadron calorimeter towers behind the supercluster to the electromagnetic energy in the supercluster; the transverse width in  $\eta$  of the electromagnetic shower; the PF isolation variables,  $I_{ch}, I_{neu}, I_{pho}, \rho$ , calculated in the cone  $R_0 = 0.3$ . Specific selection based on these variables was initially optimized on simulated samples of  $W + \gamma$  and  $W + jet$  events to maintain approximately 80% identification efficiency for a photon. Furthermore, a veto on the hits in the innermost layer of the pixel detector is applied to avoid misidentifying an electron as a photon. Such veto however, allows for the electrons produced from the conversion of the photon on the material of the pixel detector. The efficiency of the photon identification is measured with the “tag-and-probe” method using  $Z \rightarrow e^+e^-$  events in data and MC, where the electrons are reconstructed as photon showers. The efficiency of the pixel veto is estimated with  $Z \rightarrow \mu\mu\gamma$  events, where the photon is produced via FSR. The total efficiency is found to be 80% (88%) for a photon with  $E_T > 30$  (50) GeV and  $|\eta^\gamma| < 1.44$ .

The photon energy resolution is further improved by using a multivariate regression technique developed for  $H \rightarrow \gamma\gamma$  analysis. See Ref. [52] for an extended description of the technique. The energy scale corrections are applied to the reconstructed photons in data and the smearing corrections to the photons in MC events. These corrections are necessary due to imperfect knowledge of the detector and its simulation. The underlying causes are known to be from: a) tracker material simulation, b) underestimation of uncertainty in the individual crystal calibration and c) residual differences between the actual ECAL geometry and its simulation. These corrections are also derived using  $Z \rightarrow ee$  events, where the electrons are reconstructed as photons.

#### 3.4.4. Converted photons

A photon interacting in the material of the detector often converts to a pair of electrons,  $e^+e^-$ . The probability of such interaction to occur before the last three layers of the tracker is 20–50% in the barrel, and up to 60% in the endcap [52]. A method of reconstructing the tracks from the conversion electrons was developed in Ref. [53] and used in  $H \rightarrow \gamma\gamma$  analysis, as described in Ref. [52]. Fully reconstructed conversions are used in the PF reconstruction algorithm: the association of electron-track pairs with energy deposits in the ECAL avoids the photons being misidentified as charged hadrons, thus improving the determination of the photon isolation, as already discussed.

#### 3.4.5. Muons

Muons are measured in the pseudorapidity range  $|\eta| < 2.4$ , with detection planes made using three technologies: drift tubes, cathode strip chambers, and resistive plate chambers.

Matching muons to tracks measured in the silicon tracker results in a relative transverse momentum resolution for muons with  $20 < p_T < 100$  GeV of 1.3–2.0% in the barrel and better than 6% in the endcaps. The  $p_T$  resolution in the barrel is better than 10% for muons with  $p_T$  up to 1 TeV [54]. For low- $p_T$  muons used in the analysis the resolution is between 0.8% and 3% depending on  $\eta$ .

For this analysis, the muon candidates must be selected by the PF algorithm and satisfy the following requirements. The fit of the resulting track in the pixel detector must pass  $\chi^2/n_{DoF} < 3$  criterion. In CMS, this ID criteria is considered *loose* and the motivation for this choice is driven by the dedicated studies of the event reconstruction efficiency. Due to the properties of the signal, described in Section 3.1, it is important to maintain the reconstruction efficiency for events with small  $\Delta R(\mu\mu)$  separation, which corresponds to low  $m_{\mu\mu}$ . Figure 3.3 shows the event reconstruction efficiency vs. dimuon invariant mass for different muon IDs. From this figure one can see that a more commonly used *tight* ID would be inefficient for the region with  $m_{\mu\mu} < 10$  GeV. However with the selected *loose* ID we maintain a high efficiency, which is independent of the dimuon invariant mass. Figure 3.3 includes additional kinematic requirements: muon with the highest- $p_T$  (called *leading* lepton) has to have  $p_T > 23$  GeV, and the next to highest- $p_T$  muon (called *subleading*) has to have  $p_T > 4$  GeV; photon with  $p_T > 25$  GeV is also selected. Full event selection of the analysis is described in Section 3.5.

Additionally, the PF isolation in the cone  $R_0 = 0.4$  is then calculated for the leading muon:

$$(3.1) \quad I_{PF} = I_{ch} + \max(0, I_{nue} + I_{pho} - 0.5 \cdot I_{PU}).$$

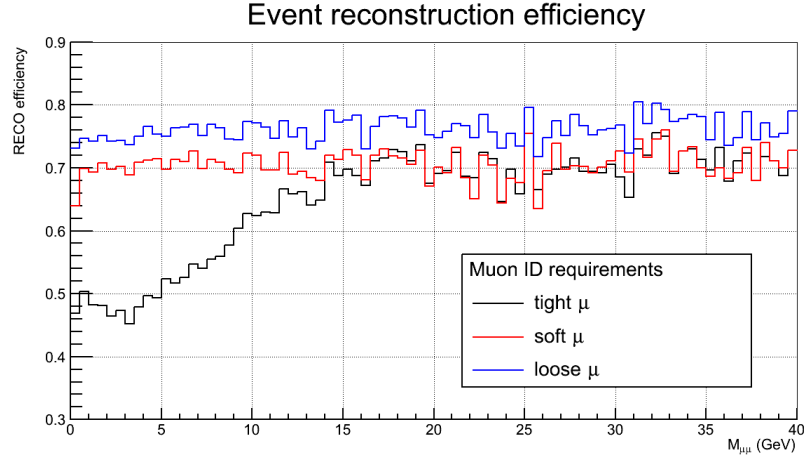


Figure 3.3. Comparison of three common muon IDs: event reconstruction efficiency as a function of dimuon invariant mass. This efficiency is calculated with the full events selection, described in Section 3.5.

The isolation is required to be less than 0.4 for the leading muon. No isolation requirement is applied for the subleading muon since those muons are already within the isolation cone of the leading muon in most events. The isolation requirement rejects misidentified leptons and background arising from hadronic jets. Full dimuon identification and isolation efficiency of about 80% is obtained.

The energy scale (in data events) and resolution (in MC) of the muons are corrected using  $Z \rightarrow \mu\mu$  events.

#### 3.4.6. Electrons

Similar to the photon reconstruction, electrons in CMS are built from the superclusters in ECAL. The shape of the supercluster is different from the photons, because electrons bend in the magnetic field along  $\phi$  direction. The superclusters are then matched to tracks in the silicon tracker [55, 56].

In the electron channel of the  $H \rightarrow \gamma^* \gamma \rightarrow \ell\ell\gamma$  decay, the two electrons produced by  $\gamma^*$  are rather close to each other. Even more so than in the muon channel, since the  $m_{\ell\ell}$  is smaller in  $\gamma^* \rightarrow ee$  process, see Fig. 3.5. Therefore, their energy deposits in the electromagnetic calorimeter are merged into one supercluster by the CMS reconstruction algorithms, giving rise to a very special signature. In order to identify these merged electrons, at least two tracks reconstructed with Gaussian Sum Filter (GSF) algorithm [57] associated to the supercluster are required. Also at least two basic ECAL clusters within a supercluster are required. The supercluster of the reconstructed *merged* electrons must have  $p_T > 30$  GeV,  $|\eta| < 1.44$ , and  $p_T^{e_1} + p_T^{e_2} > 44$  GeV for the corresponding two GSF tracks. Both GSF tracks must have no more than one missing hit in the pixel detector in order to reduce the background from photon converting into  $e^+e^-$  induced by interactions with the detector material. These criteria remove 92% of the QCD  $\gamma\gamma$  events, 80% of the QCD dijet events and 36% of the  $Z \rightarrow ee$  background events, while losing 19% of signal events.

Furthermore, a multivariate discriminator is trained to separate the  $\gamma^* \rightarrow ee$  objects from jets and single electrons. The MVA used for the ID is Boosted Decision Tree (BDT), implemented in TMVA [58]. The variables used as inputs to the BDT training include lateral shower shape variables, the energy median density per unit area in the event ( $\rho$ ), and the kinematic information of supercluster energy and GSF tracks.

There are three kinds of major backgrounds for the *merged* electrons signature:

- prompt photon conversion, which is suppressed by requiring missing hits and conversion veto, mentioned above;

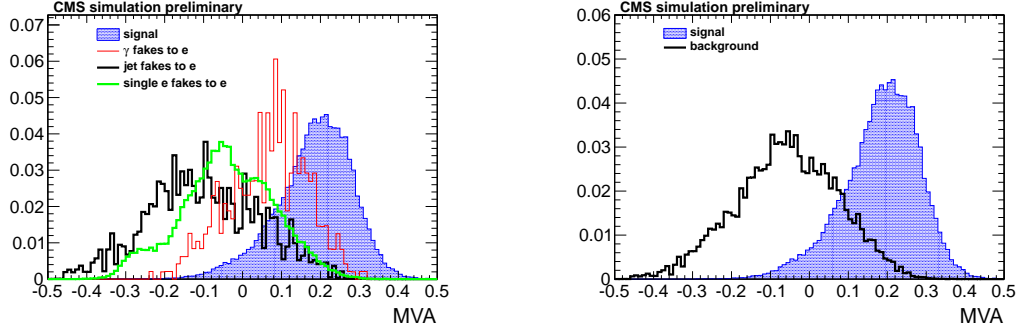


Figure 3.4. MVA response for signal and individual backgrounds (left), and combined background objects (right).

- fake photons from jets, that fragment to neutral mesons and then decay to the photon pair;
- prompt electron with a second (fake) GSF track close to the real GSF track, or a photon from bremsstrahlung which converts into GSF tracks.

The BDT output discriminator is trained with simulated samples, where the signal objects of  $\gamma^* \rightarrow ee$  are taken from the Higgs signal samples and background objects are taken from various MC background samples:  $\gamma + jet$ , QCD processes, and DY+jet. As an input to the BDT training, both signal and background electrons must pass the selection described in the beginning of this section. In order to validate the results of the MVA training the events are divided evenly between the *training* and *testing* sub-samples. Comparing the BDT output of the two samples we've concluded that there is no overtraining and the quality of the BDT discriminant is good. Figure 3.4 shows the MVA response for the signal and backgrounds. The final cut on the BDT output of 0.12 is used in the analysis.

### 3.4.7. Data/MC scale factors

Efficiency of certain object ID selection or trigger may not be properly simulated in the MC samples. Hence, event scale factors are applied to the MC samples in order to compensate for those differences. Specifically, the scale factors are applied due to the photon ID. Those corrections are *standard* in CMS and derived using a tag-and-probe method from  $Z \rightarrow ee$  events on both data and MC, see Table 3.2 for a summary. On the other hand, the muon scale factors needed to be estimated for our event topology. This was done using MC signal samples and  $J/\psi \rightarrow \mu\mu$  events in data. It was found that the uncertainty on the scale factors is larger than the correction itself. Hence, no correction is applied, and the systematic uncertainty is assigned instead. Those uncertainties are summarized in Section 3.7. Similarly, efficiency in the electron channel is not measured in data, instead the uncertainty is assigned based on the studies of the simulated signal samples.

Table 3.2. Photon ID scale factors applied per photon.

$\eta/p_T$ range	40–50 GeV	> 50 GeV
ID		
$0 <  \eta  < 0.8$	$0.9804 \pm 0.0005$	$0.9787 \pm 0.0009$
$0.8 <  \eta  < 1.5$	$0.9840 \pm 0.0006$	$0.9822 \pm 0.0011$
Conv. electron veto		
$0 <  \eta  < 1.44$	$0.993 \pm 0.029$	$1.0 \pm 0.0$

### 3.5. Event selection

Initial event selection is performed during the data-taking by the HLT. In the muon channel, the trigger requires a muon and a photon, both with  $p_T > 22$  GeV. In the electron channel, the  $\gamma^* \rightarrow ee$  process at low dielectron invariant mass mimics a photon at the trigger level. For this reason, a diphoton trigger is used in the electron channel, to select the  $\gamma^*\gamma$  final state events. The trigger requires a leading (subleading) photon with  $p_T$  greater than 26 (18) GeV. The diphoton trigger is inefficient for events with high dielectron invariant mass ( $m_{ee} > 2$  GeV) due to the isolation and shower shape requirements. The available dielectron triggers cannot be used to select events with  $2 < m_{ee} < 20$  GeV either, because they require isolation, and their  $p_T$  threshold on the subleading lepton is too stringent.

The efficiency of the triggers for the signal events after the selection requirements described bellow is 85% (90%) in the muon (electron) channel, as obtained from the simulated samples.

In the offline selection, the events are required to have at least one primary vertex, as described in Section 3.4.1. The lepton tracks from  $\gamma^* \rightarrow \mu\mu$  ( $ee$ ) are required to originate from the primary vertex, and to have transverse and longitudinal impact parameters with respect to that vertex smaller than 2.0 (0.2) mm and 5 (1) mm, respectively.

The muons (electrons) are required to be within  $|\eta| < 2.4$  (1.44), while the photon must have  $|\eta| < 1.44$ . The three-body invariant mass is required to satisfy  $110 < m_{\ell\ell\gamma} < 170$  GeV. The photon and dilepton momenta must satisfy  $p_T^\gamma > 0.3 \cdot m_{\ell\ell\gamma}$  and  $p_T^{\ell\ell} > 0.3 \cdot m_{\ell\ell\gamma}$  requirements, which are optimized for high signal efficiency and background rejection. The muons must be oppositely charged, and have  $p_T$  greater than 23 (4) GeV



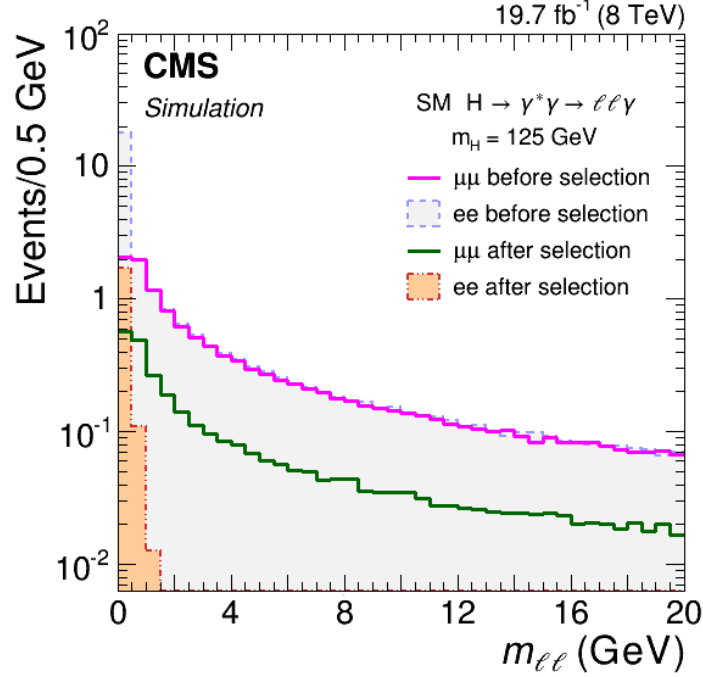


Figure 3.5. The invariant mass of the dilepton system in signal simulation for  $m_H = 125$  GeV. Distributions are shown for muon and electron channels, before and after selection. The invariant mass before selection is obtained from the leptons at the generator level, while after selection the reconstructed invariant mass is used.

for the leading (subleading) muon. The  $p_T$  requirement on the leading muon is driven by the trigger threshold, and on the subleading muon by the minimum energy needed for a particle to reach the muon system, while maintaining high reconstruction efficiency. In the electron channel, no additional selection on  $p_T$  of the GSF tracks is necessary, beyond those described in Section 3.4.6. Finally, in both muon and electron channels, the separation between each lepton and the photon is required to satisfy  $\Delta R > 1$  in order to suppress Drell–Yan background events with FSR.

The dilepton invariant mass in the muon channel is required to be less than 20 GeV to reject contributions from  $pp \rightarrow Z\gamma$  and to suppress interference effects from  $H \rightarrow Z\gamma$

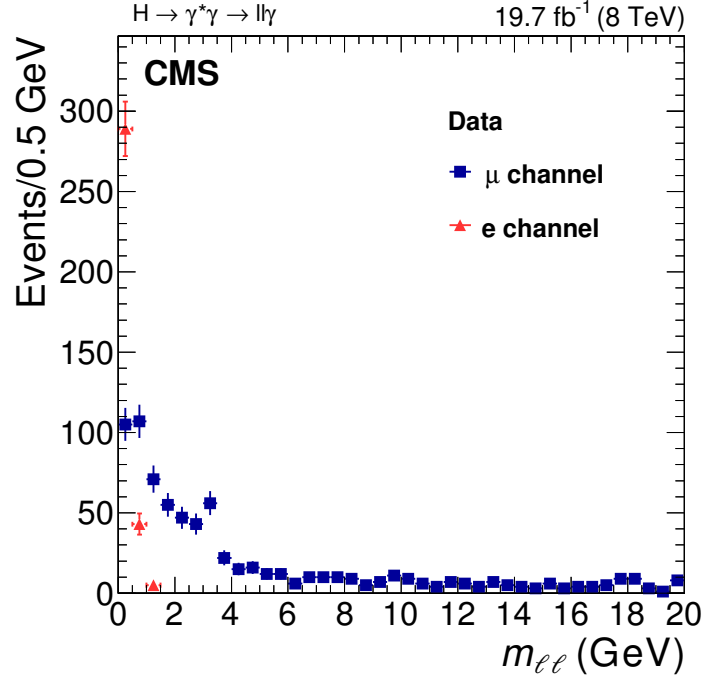


Figure 3.6. The invariant mass of the dilepton system in data for muon and electron channels. The distributions produced after the selection described in the text, but without rejecting the  $V \rightarrow \mu\mu$  contributions in data.

process and box diagrams shown in Fig. 1.6. Events with a dimuon mass  $2.9 < m_{\mu\mu} < 3.3$  GeV and  $9.3 < m_{\mu\mu} < 9.7$  GeV are rejected to avoid the  $J/\psi \rightarrow \mu\mu$  and  $\Upsilon \rightarrow \mu\mu$  contamination. In the electron channel the invariant mass, constructed from the two GSF tracks, is required to satisfy  $m_{ee} < 1.5$  GeV. There are almost no events in the electron channel for  $m_{ee} > 1.5$  GeV due to the trigger requirement mentioned before. The  $m_{\ell\ell}$  distributions for the simulated signal events are shown in Fig. 3.5 in the muon and electron channels. The  $m_{\ell\ell}$  distributions in data are shown in Fig. 3.6. The distributions of the data events should be thought of as the background, thus the shapes of the background and signal events in Fig. 3.5 are to be compared.

Table 3.3. The expected signal yield and the number of events in data, for an integrated luminosity of  $19.7 \text{ fb}^{-1}$ . Signal events are presented before and after applying the full selection criteria described in the text. In the  $(J/\psi)\gamma$  sub-category only  $J/\psi \rightarrow \mu\mu$  decay is considered, and the signal yield is a sum of two contributions:  $H \rightarrow (J/\psi)\gamma \rightarrow \mu\mu\gamma$  and  $H \rightarrow \gamma^*\gamma \rightarrow \mu\mu\gamma$ , where dimuon mass distribution is non-resonant.

Sample	Signal events $m_H = 125 \text{ GeV}$		Number of events in data $120 < m_{\ell\ell\gamma} < 130 \text{ GeV}$
	before selection	after selection	
$\mu\mu\gamma$	13.9	3.3	151
$ee\gamma$	25.8	1.9	65
$(J/\psi \rightarrow \mu\mu)\gamma$	0.065 (J/ $\psi$ ) + 0.32 (non-res.)	0.014 (J/ $\psi$ ) + 0.078 (non-res.)	12

In the special case of the search for  $H \rightarrow (J/\psi)\gamma \rightarrow \mu\mu\gamma$ , both  $p_T^\gamma > 40 \text{ GeV}$  and  $p_T^{\mu\mu} > 40 \text{ GeV}$  are required, and the events are selected within  $2.9 < m_{\mu\mu} < 3.3 \text{ GeV}$ .

The expected signal yields for  $m_H = 125 \text{ GeV}$  and the observed yield in the  $10 \text{ GeV}$  mass bins after the full event selection are listed in Table 3.3. Additionally, Table 3.4 shows the event yield in data, broken down into four data-taking periods of CMS. The beam conditions (e.g. pileup) and the integrated luminosity were different in those periods. The data show the yields statistically consistent with the integrated luminosity per period, mostly independent of the different conditions.

After the full selection one can look at the distributions of interest:  $m_{\ell\ell}$ ,  $p_T^{\ell_1}$ ,  $p_T^{\ell_2}$ ,  $p_T^\gamma$ ,  $\Delta R(\ell, \gamma)$ , etc. These figures are presented in Appendix D. The shapes of all these distributions in data end up looking very similar to those in simulated signal sample, which suggests no further kinematic separation can be achieved using these variables.

In the muon channel, about 3.4 signal events are expected for  $m_H = 125 \text{ GeV}$  Higgs boson, while the background is about  $92 \pm 9$  events within  $122 < m_{\ell\ell\gamma} < 128 \text{ GeV}$  (estimated from the fit to the data, as discussed in Section 3.6). In the electron channel

$m_{\ell\ell\gamma}$ range, GeV		A	B	C	D	Total
$\mu$ channel	110–120	14	40	81	69	204
	120–130	6	33	49	63	151
	130–140	13	29	39	36	117
	140–150	3	18	41	24	86
	150–160	5	15	19	28	67
	160–170	1	12	17	13	43
Total in 110–170		42	147	246	233	668
e channel	110–120	7	23	37	34	101
	120–130	2	13	21	29	65
	130–140	3	16	24	17	60
	140–150	2	15	14	9	40
	150–160	2	4	12	14	32
	160–170	2	2	10	8	22
Total in 110–170		18	73	118	111	320
Integrated luminosity, $\text{fb}^{-1}$		0.88	4.41	7.06	7.36	19.7

Table 3.4. Events break down by the data-taking periods and bins of  $m_{\ell\ell\gamma}$ .

the signal-to-background ratio is much smaller, which results in a weaker limit on the SM signal strength. It should be also mentioned that in the electron channel there is a contribution from the  $H \rightarrow \gamma\gamma$  process due to unidentified conversions, which is about 15% of the  $H \rightarrow \gamma^*\gamma$  signal (0.2 events at  $m_H = 125$  GeV). This contribution is considered as a background to  $H \rightarrow \gamma^*\gamma$ , and it is negligible compared to the continuum background estimated from the fit to data described in the next section.

From Table 3.3, the total signal efficiency is  $\varepsilon_{tot} = 3.3/13.9 \approx 0.24$ , i.e. 24%, in the muon channel for  $m_H = 125$  GeV. It rises to  $\sim 25\%$  for  $m_H = 150$  GeV. Correspondingly, in the electron channel,  $\varepsilon \approx 7\%$ , which rises to  $\sim 9\%$  for  $m_H = 150$  GeV. For the  $H \rightarrow (J/\psi)\gamma$  signal,  $\varepsilon \approx 22\%$ .

Finally, the  $m_{\ell\ell\gamma}$  distributions are shown in Fig. 3.7 for the Dalitz search and in Fig. 3.8 for the  $H \rightarrow (J/\psi)\gamma$  search. A smooth polynomial fit to these spectra in data is used as a

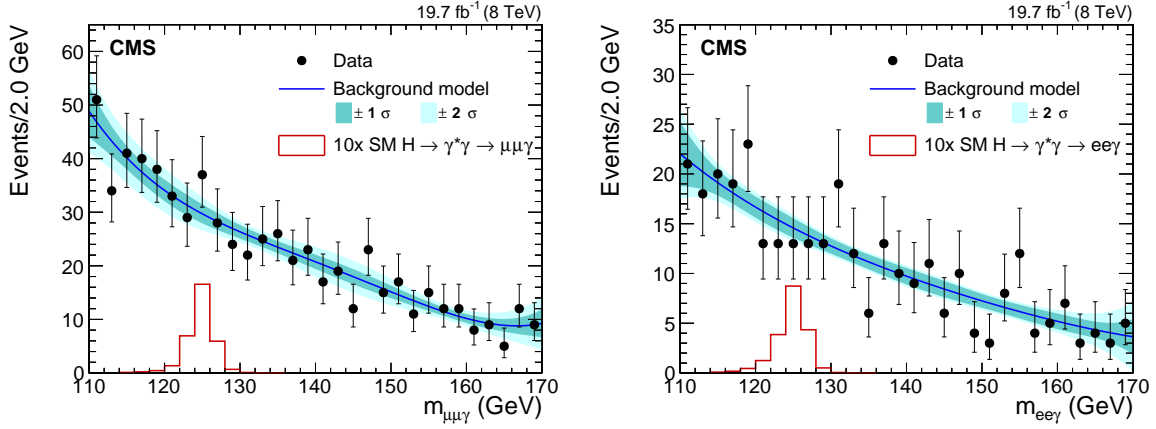


Figure 3.7. The  $m_{\mu\mu\gamma}$  (left) and  $m_{ee\gamma}$  (right) spectra for 8 TeV data (points with error bars), together with the result of a background-only fit to the data. The  $1\sigma$  and  $2\sigma$  uncertainty bands represent the uncertainty in the parameters of the fitted function. The expected contribution from the SM Higgs boson signal with  $m_H = 125$  GeV, scaled up by a factor of 10, is shown as a histogram.

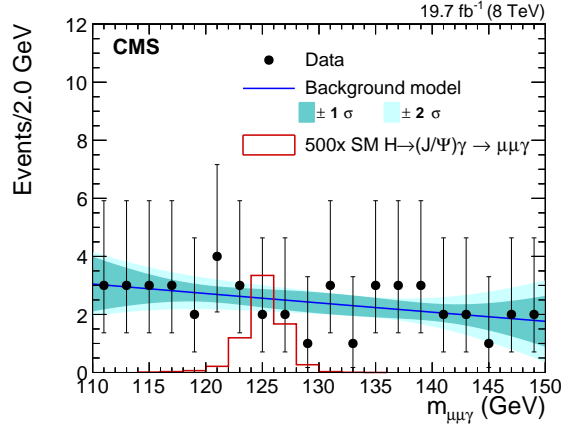


Figure 3.8. The  $m_{\mu\mu\gamma}$  distribution for events within  $2.9 < m_{\mu\mu} < 3.3$  GeV for 8 TeV data (points with error bars), together with the result of a background-only fit to the data. The  $1\sigma$  and  $2\sigma$  uncertainty bands represent the uncertainty in the parameters of the fitted function. The expected contribution from the  $H \rightarrow (J/\psi)\gamma \rightarrow \mu\mu\gamma$  process of the SM Higgs boson,  $m_H = 125$  GeV, scaled up by a factor of 500, is shown as a histogram.

background prediction. An excess of events in data above the background curve, at any particular mass point, could indicate a presence of a signal peak. The strength of the signal is then determined using the statistical methods described in Section 3.6.

Resolution of the  $m_{\ell\ell\gamma}$  variable plays a crucial role in the analysis sensitivity. Table 3.5 shows the effective width of the  $m_{\ell\ell\gamma}$  distributions obtained from the MC signal samples. It is calculated as an RMS of the  $m_{\ell\ell\gamma}$  dataset obtained from the MC signal sample, considering only the points within  $0.9 \times m_H < m_{\ell\ell\gamma} < 1.1 \times m_H$ . Examples of the mass distributions for  $m_H = 125$  and  $145$  GeV are shown in Fig. 3.9. The resolution of  $\sim 1.6\%$  is achieved in the muon channel and  $\sim 1.8\%$  in the electron channel. For comparison, in the  $H \rightarrow \gamma\gamma$  search the resolution of the  $m_{\gamma\gamma}$  varies from  $0.9\%$  to  $2\%$  for  $m_H = 125$  GeV, depending on the event category [52].

$m_H$	$\sigma_{\ell\ell\gamma}^{eff}$ , GeV; $(\sigma_{\ell\ell\gamma}^{eff}/m_H)$	
	$\mu$ channel	e channel
120	1.79 (1.5%)	2.13 (1.8%)
125	1.97 (1.6%)	2.24 (1.8%)
130	2.09 (1.6%)	2.28 (1.8%)
135	2.12 (1.6%)	2.40 (1.8%)
140	2.22 (1.6%)	2.43 (1.7%)
145	2.27 (1.6%)	2.50 (1.7%)
150	2.35 (1.6%)	2.54 (1.7%)

Table 3.5. Effective width of the Higgs boson candidate mass distribution obtained from a gluon fusion MC signal sample.

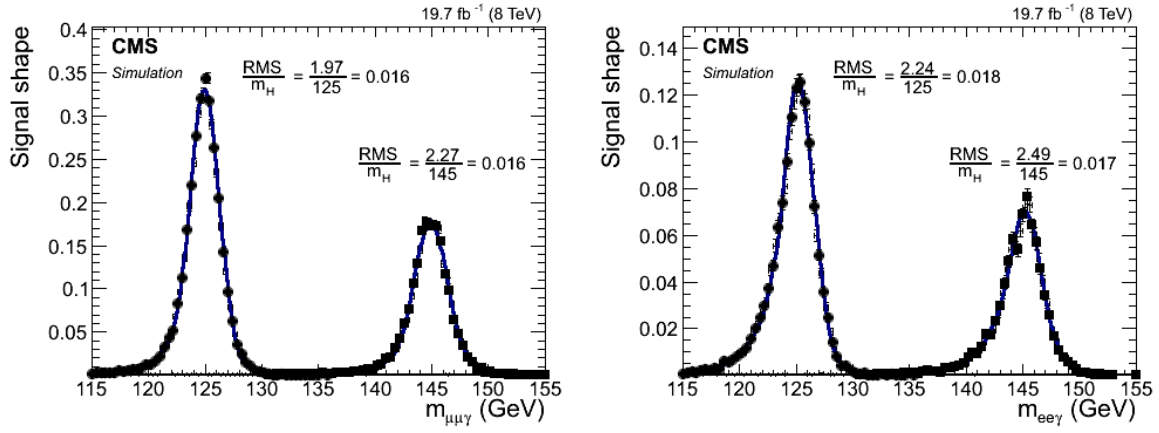


Figure 3.9. Reconstructed three-body mass distributions from the signal MC samples for  $m_H = 125$  and  $145$  GeV in muon (left) and electron (right) channels. These distributions are clearly non-Gaussian. The blue curves represent the fits to a Crystal Ball plus a Gaussian function, discussed in the next section.

### 3.5.1. VBF tag in the muon channel

An importance of the VBF/VH event tagging for the purpose of increasing the sensitivity of an analysis was mentioned in Sec. 1.2. At the current stage, however, such tagging does not bring much to the sensitivity. For example, after a basic selection for the VBF tag, very little signal is expected. In addition, there are too few events left in the data to perform the fit for the background estimation. I describe this result in the Appendix C. Due to these two reasons, no VBF/VH tagging is used throughout the analysis at present, although it will be useful in the future data-taking at 13 TeV, with larger data sample.

### 3.5.2. Additional categories in the muon channel

The selection described in the previous section can be extended in various ways, in order to increase the sensitivity of the search. Let me remind that the main analysis only includes the photons in the barrel,  $|\eta_{SC}^\gamma| < 1.4$ , and low dilepton invariant mass,  $m_{\mu\mu} < 20$  GeV (labeled *EB* further in the text). Hence, the two obvious choices to extend the analysis selection, are:

- To extend the pseudorapidity of the photons to the endcap:  $1.6 < |\eta_{SC}^\gamma| < 2.5$  (labeled *EE*)
- To extend the  $m_{\mu\mu}$  range to  $20 < m_{\mu\mu} < 50$  GeV, while  $|\eta_{SC}^\gamma| < 1.4$  (labeled *mll50*)

These two categories can be included in the analysis and the number of events in each category are shown in Table 3.6. Already from this table once can see that the signal-to-background ratios in the two extra categories is much lower than in the main category.



Table 3.6. Events per category in the muon channel after the selection described in the text.

Category	Total signal $m_H = 125 \text{ GeV}$	Data events in $120 < m_{\mu\mu\gamma} < 130 \text{ GeV}$
(1) $EB$	3.25	151
(2) $EE$	0.80	91
(3) $mll50$	0.56	67

This will manifest itself in a lower sensitivity. Figure 3.10 shows the final distributions of the three-body invariant mass in the two additional categories.

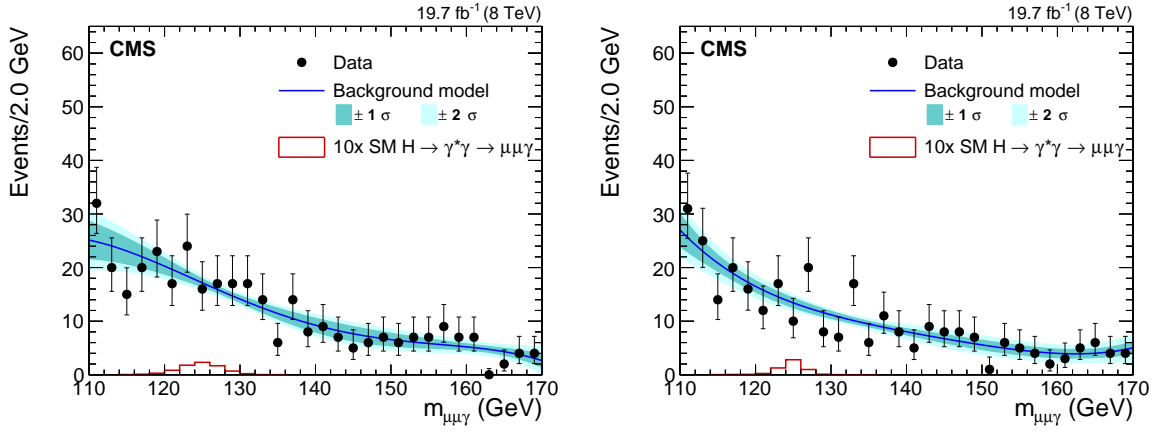


Figure 3.10. The  $m_{\ell\ell\gamma}$  distributions in muon channel for two additional event categories,  $EE$  (left) and  $mll50$  (right), described in the text.

### 3.6. Statistical Methods

The  $m_{\ell\ell\gamma}$  distributions are used to obtain the background prediction with a fit to the data events. An un-binned fitting to a polynomial is performed, over the range of  $110 < m_{\mu\mu\gamma} < 170$  GeV for the Dalitz search (Fig. 3.7) and the range of  $110 < m_{\mu\mu\gamma} < 150$  GeV for the  $H \rightarrow (J/\psi)\gamma$  search (Fig. 3.8). The fit chosen for the background model is a *Bernstein* polynomial of degree 4, and its probability density function (pdf) is:

$$(3.2) \quad b = \text{Bern}(p_1, p_2, p_3),$$

with 3 free parameters,  $p_1, p_2, p_3$ . The degree of the polynomial is the lowest that gives an unbiased fit in the full mass range and for the most of the MC toy models (see Section 3.6.1 below regarding the bias studies).

Similarly, the pdf of the signal model is obtained from the un-binned fit of the three-body mass in the signal MC sample. The fit function is *Crystal Ball* [59] *plus a Gaussian*:

$$(3.3) \quad s = CB(m, \sigma_1, n, \alpha) + f_G \cdot \mathcal{G}(m, \sigma_2),$$

with the same mean,  $m$ . The same pdf form is used for the ggF, VBF and VH samples, as well as the  $H \rightarrow (J/\psi)\gamma$  sample. Figure 3.11 shows the distributions of the signal pdfs obtained from the ggF MC sample. Once the fit for a particular signal mass is obtained, the parameters of the fit are frozen, and two nuisance parameters,  $\kappa_m$  and  $\kappa_\sigma$ , are introduced, as multiplicative factors to the mean and width of the signal peaks:

$$(3.4) \quad m' = \kappa_m \cdot m, \quad \sigma' = \kappa_\sigma \cdot \sigma.$$

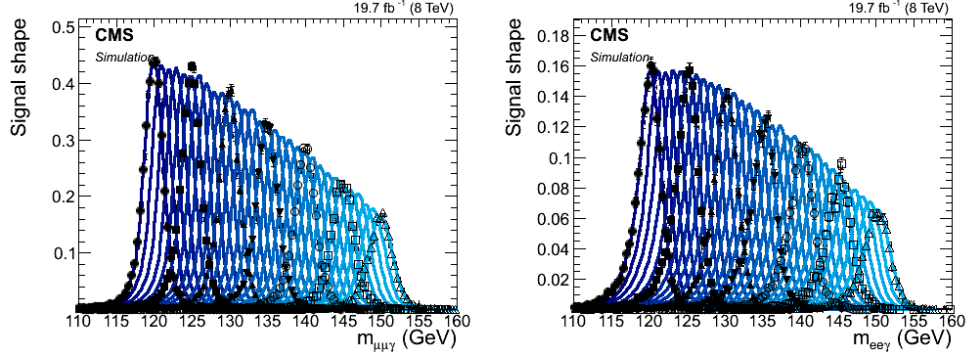


Figure 3.11. Signal model fits are shown for ggH production mode in muon channel (left) and electron channel (right). The simulated samples are produced for masses at every 5 GeV and indicated by marker points. The functions in between are obtained by an interpolation of the two near-by mass points at 1 GeV intervals.

These nuisances are used to incorporate the systematic uncertainties, described in the Section 3.7. That is,  $\kappa_m = 1 \pm \delta\kappa_m$   $\kappa_\sigma = 1 \pm \delta\kappa_\sigma$ , where  $\delta\kappa_m$  and  $\delta\kappa_\sigma$  are the one-sigma uncertainties on the scale and resolution of the signal peak.

Then, following the limit setting procedure described in Ref. [60], the Likelihood function can be written as:

$$(3.5) \quad \mathcal{L}(\mu, \theta) = \text{Poisson}(\mu \cdot s(\kappa_m, \kappa_\sigma) + b(p_1, p_2, p_3)) \cdot p(\tilde{\theta}|\theta),$$

where  $\mu$  is a signal strength, and  $\theta$  represents all other nuisance parameters in the model,  $\theta = \{\kappa_m, \kappa_\sigma, p_1, p_2, p_3\}$ . In this expression  $p(\tilde{\theta}|\theta)$  is the pdf for the nuisance parameters  $\theta$ , from a fictional auxiliary measurement  $\tilde{\theta}$ . Including the nuisance pdf in this way allows us to constrain the likelihood using a pure frequentist calculation [60]. The function in eq. (3.5) can be used to represent the *background only* hypothesis,  $\mathcal{L}_b = \mathcal{L}(\mu = 0)$ , and *backgrounds plus signal* hypothesis,  $\mathcal{L}_{s+b} = \mathcal{L}(\mu = 1)$ , where  $\mu$  is equal to 1 for the nominal SM Higgs boson hypothesis.

For the purpose of hypothesis testing, the Likelihood ratio  $\mathcal{L}_{s+b}/\mathcal{L}_b$  provides the most powerful test, according to Neyman&Pearson [61]. This Likelihood ratio is called *test statistic* and can be written as:

$$(3.6) \quad t(\mu) = \frac{\mathcal{L}_{s+b}}{\mathcal{L}_b} = \frac{\mathcal{L}(\mu, \theta)}{\mathcal{L}(0, \theta)}.$$

However, given that the expected signal from the SM Higgs boson is quite small, we are not sensitive to determine the presence of the signal (that is  $\mathcal{L}_{s+b}$  and  $\mathcal{L}_b$  hypotheses can not be strictly separated). Hence, the statistical analysis is instead set up to place an upper limit on the signal strength parameter,  $\mu$ . For this purpose, according to Ref. [62], a different test statistic is used:

$$(3.7) \quad \tilde{\lambda}(\mu) = \begin{cases} \frac{\mathcal{L}(\mu, \hat{\theta}_\mu)}{\mathcal{L}(\hat{\mu}, \hat{\theta})} & \text{if } \hat{\mu} \geq 0 \\ \frac{\mathcal{L}(\mu, \hat{\theta}_\mu)}{\mathcal{L}(0, \hat{\theta}_{\mu=0})} & \text{if } \hat{\mu} < 0 \end{cases},$$

where  $\hat{\theta}_\mu$  denotes the value of  $\theta$  that maximizes  $\mathcal{L}$  for the specified  $\mu$  (thus it is a function of  $\mu$ ), and the denominator is an unconditional maximum likelihood function, i.e.  $\hat{\mu}$  and  $\hat{\theta}$  are their maximum likelihood estimators for  $\mathcal{L}$ . The second part of this definition restricts negative signals, which is the case in our situation.

Furthermore, for the purpose of setting an upper limit on  $\mu$ , one should not regard the data with  $\hat{\mu} > \mu$  as representing less compatibility with  $\mu$  than the data obtained.

Thus, we define:

$$(3.8) \quad \tilde{q}_\mu = \begin{cases} -2 \ln \tilde{\lambda}(\mu) & \text{if } \hat{\mu} \leq \mu \\ 0 & \text{if } \hat{\mu} > \mu \end{cases}.$$

Using this test statistic and setting the confidence level at 95% with  $\text{CL}_s$  criterion [60, 63, 64], the upper limit on  $\mu$  is obtained given the observed data. Moreover, in order to evaluate the expected limits based on the pdfs of the signal and background (not looking at the data) the *asymptotic methods* are used as described in Ref [62].

The results of this statistical approach are presented in Section 4, after describing the treatment of systematic uncertainties,  $\theta$ , in Section 3.6.1 and 3.7.

### 3.6.1. Background Fit Bias Study

The true form of the background  $m_{\ell\ell\gamma}$  distribution is unknown. Hence the analysis described in the previous section can suffer from a mis-modeling of this distribution obtained from the fit in data. The effect of this mis-modeling can lead to biases in the analysis sensitivity. These biases can be quantified with a Monte Carlo toy study, which I describe in this section.

As can be seen from Fig. 3.12, many different functions would result in a good fit to the data. Some of these functions are chosen for this test and are used as a truth model when generating the toy events. The following list of functions is used:

- Exponential,  $e^{-ax}$ ;
- Power law,  $ax^{-b}$ ;
- Laurent polynomials of the form  $ax^{-4} + bx^{-6}$ ;

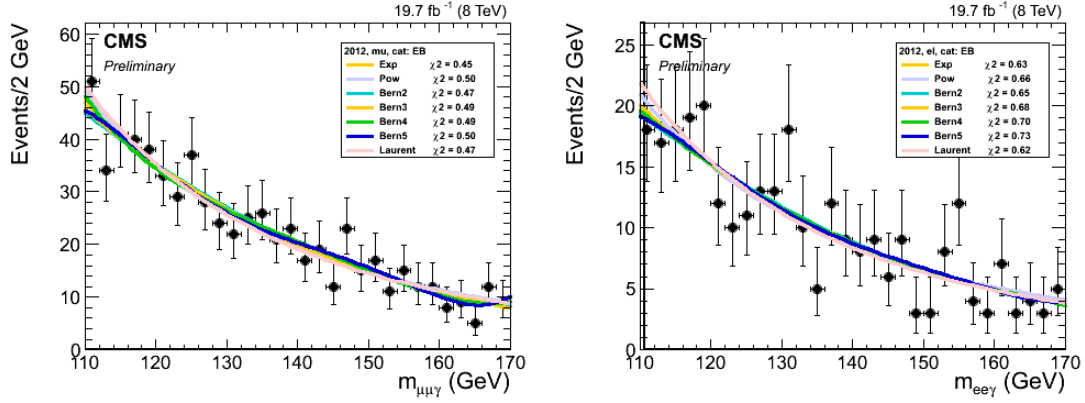


Figure 3.12. Data events after the final selection and the fits of  $m_{\mu\mu\gamma}$  distribution, in the range  $110 < m_{\mu\mu\gamma} < 170$  GeV for three categories: *EB*, *EE*, *ml50*.

- Bernstein polynomials of degrees 2 to 5.

First, the chosen function is fit to the data events, then a toy dataset is generated from the fit. No signal is introduced. Then, the resulting toy dataset is fit to the Bernstein polynomials *plus* the signal pdf (which can be negative). Fig. 3.14 shows a few examples of the toy data and the fits to it for  $m_H = 125$  GeV signal. Repeating this toy experiment many times, we expect on average zero signal events predicted by the fit. To quantify if that is the case, two pull distributions are obtained,  $N_{Sig}^{FIT}/\sigma_{Sig}^{FIT}$  and  $N_{Sig}^{FIT}/\sigma_{Bkg}^{FIT}$ , and the following criteria are used to identify an unbiased fit:

- The pull distribution of  $N_{Sig}^{FIT}/\sigma_{Sig}^{FIT}$  have to be Gaussian with mean zero and width one. Here,  $N_{Sig}^{FIT}$  is the number of signal events predicted by the fit and  $\sigma_{Sig}^{FIT}$  is the error on that number. This distribution is constructed from 50 000 toys. If its mean is less than 0.2, for a particular background function, then that fit function is considered unbiased. This criterion ensures that a possible bias is at least five times smaller than the statistical fluctuation.

- A modified pull distribution,  $N_{Sig}^{FIT}/\sigma_{Bkg}^{FIT}$ , should also have the mean less than 0.2 for an unbiased fit. Here  $\sigma_{Bkg}^{FIT}$  is the error on the number of background events from the fit.

As an example, the pull distributions for  $m_H = 125$  GeV, obtained with the *Exponential* function as true model are shown on Figure 3.13. A complete set of the means of the distributions are presented in Tables 3.7, 3.8 for the muon channel and 3.9, 3.10 for the electron channel. One can see that the Bernstein polynomials of degree 3 do not satisfy the criteria of the mean being less than 0.2. On the other hand, the degree 4 polynomial does pass this condition (except for a few cases), thus it is chosen as the background model, both in the muon and electron channels.

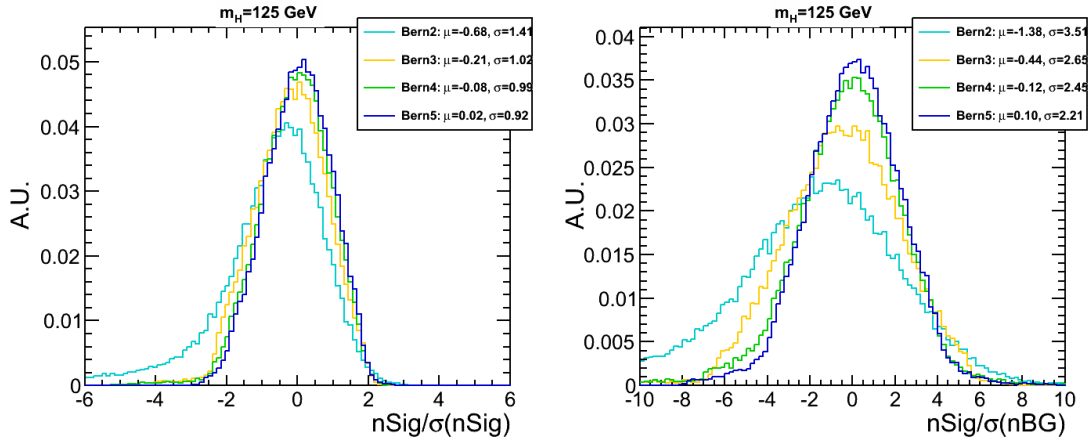


Figure 3.13. Examples of pull distribution obtained from the toy data with  $m_H = 125$  GeV signal and the Exponential function as the true background model. Category 1 in muon channel.

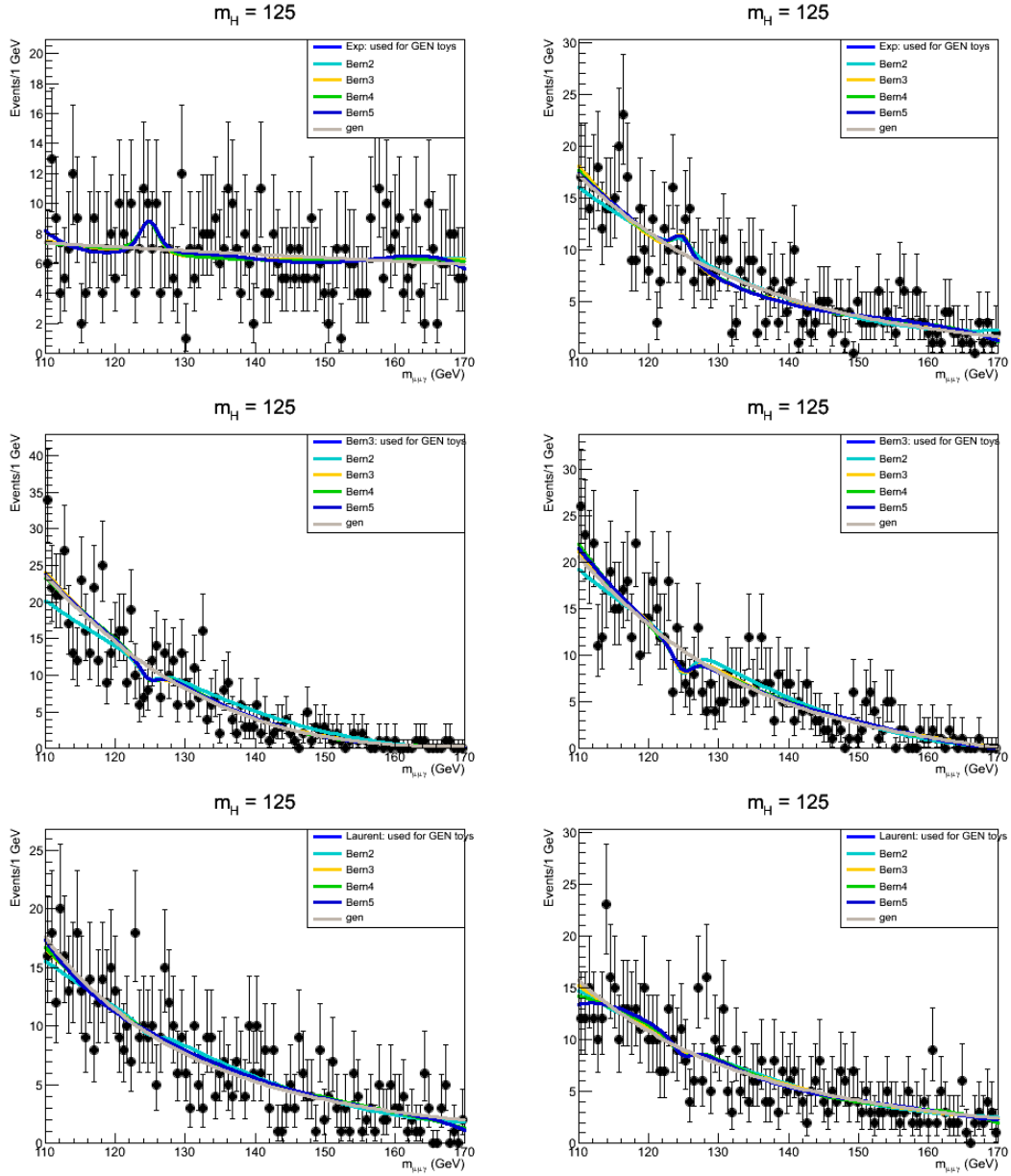


Figure 3.14. Examples of the toy data generated from Exp (top), Bernstein  $3^d$  order (middle) and Laurent (bottom) functions. Generator function is indicated by gray colored line (background only) and light-blue (for background plus signal). The fits of Bernstein functions of degrees 2 to 5 with a signal at  $m_H = 125$  GeV are shown in other colors. Negative fluctuations of the signal are allowed. On average we expect zero signal within 1 sigma of the statistical fluctuation of the background.



Table 3.7. Mean values of the  $N_{Sig}^{FIT}/\sigma_{Sig}^{FIT}$  pull distributions in the muon channel. Three true models (gen. functions) are used, each is fit to a polynomial of degrees 3, 4 and 5.

Gen func:	Exp			Pow			Laurent		
	Mean of the pull, using Bernstein polynomial of degree:								
$m_H$	3	4	5	3	4	5	3	4	5
120	-0.19	-0.13	-0.08	-0.29	-0.18	-0.10	-0.06	0.01	0.04
125	-0.21	-0.08	0.02	-0.38	-0.15	0.03	-0.10	-0.01	0.01
130	-0.13	0.01	0.04	-0.26	0.01	0.08	-0.02	0.03	0.03
135	-0.11	0.03	0.01	-0.12	0.05	0.03	0.02	-0.00	-0.01
140	-0.04	0.03	-0.01	0.06	0.09	0.01	0.06	-0.01	-0.02
145	0.05	-0.01	-0.06	0.15	0.05	-0.05	0.05	-0.04	-0.05
150	0.08	-0.01	-0.05	0.19	0.00	-0.04	-0.01	-0.07	-0.05

Table 3.8. Mean values of the  $N_{Sig}^{FIT}/\sigma_{Bkg}^{FIT}$  pulls in the muon channel.

Gen func:	Exp			Pow			Laurent		
$m_H$	Mean of the pull, using Bernstein polynomial of degree:								
	3	4	5	3	4	5	3	4	5
120	-0.41	-0.20	-0.07	-0.66	-0.30	-0.08	-0.08	0.08	0.12
125	-0.44	-0.12	0.10	-0.87	-0.22	0.14	-0.17	0.07	0.06
130	-0.31	0.12	0.21	-0.67	0.13	0.28	0.09	0.17	0.13
135	-0.04	0.19	0.12	-0.25	0.26	0.18	0.19	0.10	0.08
140	0.11	0.18	0.07	0.31	0.33	0.11	0.26	0.10	0.04
145	0.31	0.12	-0.04	0.61	0.26	-0.01	0.24	0.05	-0.00
150	0.41	0.12	0.00	0.65	0.17	0.04	0.11	-0.03	0.01

Table 3.9. Mean values of the  $N_{Sig}^{FIT}/\sigma_{Sig}^{FIT}$  pulls in the electron channel.

Gen func:	Exp			Pow			Laurent		
$m_H$	Mean of the pull, using Bernstein polynomial of degree:								
	3	4	5	3	4	5	3	4	5
120	-0.29	-0.20	-0.14	-0.39	-0.21	-0.09	-0.09	-0.02	0.03
125	-0.40	-0.25	-0.16	-0.35	-0.08	0.02	-0.08	0.01	0.04
130	-0.47	-0.28	0.02	-0.27	-0.07	0.05	-0.06	-0.01	-0.01
135	-0.09	0.02	0.00	-0.15	0.03	0.03	-0.00	0.00	-0.01
140	-0.07	-0.02	-0.05	-0.07	0.03	-0.03	-0.01	-0.04	-0.06
145	0.02	-0.02	-0.07	0.09	0.04	-0.03	0.01	-0.05	-0.05
150	0.09	-0.04	-0.09	0.16	-0.01	-0.06	-0.06	-0.12	-0.09

Table 3.10. Mean values of the  $N_{Sig}^{FIT}/\sigma_{Bkg}^{FIT}$  pulls in the electron channel.

Gen func:	Exp			Pow			Laurent		
$m_H$	Mean of the pull, using Bernstein polynomial of degree:								
	3	4	5	3	4	5	3	4	5
120	-0.62	-0.41	-0.26	-0.85	-0.40	-0.10	-0.09	0.08	0.21
125	-1.00	-0.51	-0.19	-0.85	-0.05	0.21	-0.05	0.20	0.21
130	-0.68	-0.25	0.19	-0.65	0.00	0.28	0.04	0.15	0.10
135	-0.02	0.23	0.16	-0.22	0.27	0.25	0.23	0.16	0.12
140	0.10	0.14	0.04	0.14	0.29	0.10	0.21	0.10	0.00
145	0.32	0.18	-0.01	0.55	0.37	0.11	0.22	0.09	0.05
150	0.54	0.17	-0.01	0.71	0.25	0.07	0.11	-0.07	0.01

### 3.7. Systematic uncertainties

Systematic uncertainties are propagated to the final results through the nuisance parameters,  $\theta$ , in the likelihood function and test statistic of eq. (3.7). These uncertainties are caused by the incomplete understanding of the detector, and theoretical uncertainties on the signal production and decay mechanisms. The background prediction is taken from a fit to the data with no systematic uncertainties assigned to its estimation. Only the uncertainty on the fit itself, provided by RooFit [65] for each parameter of the fit function, and the statistical uncertainty of the background prediction are considered. The procedure to ensure that the fits are unbiased is followed as described in Section 3.6.1.

In this section I discuss the uncertainties on the simulated signal. We account for them by propagating every uncertainty to the estimation of the signal yield and/or its shape, using the MC samples. There are three distinct classes of uncertainties that are assigned to the signal modeling:

- (1) **Uncertainty on the predicted yield.** The main source for it is the theoretical uncertainty on the cross section due to PDFs and scale (up to 8%) [7, 66, 67, 68], and the branching fraction of the Higgs decay, 10% [24, 16].

Second source of this uncertainty is due to the detector simulation of the reconstructed objects, which leads to a different reconstruction and ID efficiencies in the simulated events and data. The uncertainty due to the dimuon reconstruction efficiency, 11%, is obtained from data using  $J/\psi \rightarrow \mu\mu$  events. It is dominated by the statistical uncertainty of the data sample (see Sec. 3.7.2 for more details). In the electron channel, the corresponding uncertainty 3.5%, is obtained from simulation, because no data-driven methods are available for the

unique object of merged electrons (see Sec. 3.7.4). The 11% uncertainty estimated for the muons is sufficiently small that it has no impact on the result, thus although it is probable that a simulation study could greatly reduce the uncertainty, no such study was attempted.

The uncertainty due to the photon ID is quite small and comes from the errors on the scale factors presented in Table 3.2.

- (2) **Uncertainty on the energy scale.** It arises from the uncertainties on the energy scale of the muons, electrons and photons, and propagated to the uncertainty on the mean of the Higgs boson mass peak in the simulated samples. Technically, it is implemented as a multiplicative nuisance parameter,  $\kappa_\mu$  on the mean of the signal fit function (see Section 3.6). The uncertainty of  $\delta\kappa_\mu = 0.1\ (0.5)\%$  is assigned in the muon (electron) channel.
- (3) **Uncertainty on the energy resolution.** It comes from the same sources as the scale uncertainty and implemented as a multiplicative nuisance parameter  $\kappa_\sigma$  on the width of the signal model function. Conservatively, a  $\delta\kappa_\sigma = 10\%$  is assigned in both muon and electron channels.

Details on the photon, muon and electron scale and resolution can be found in Sections 3.7.1, 3.7.3 and 3.7.4 respectively.

The full list of uncertainties are listed in Table 3.11, while more details on some of them are presented in the next subsections.

Table 3.11. Sources of the systematic uncertainties.

Source	Uncertainty
Integrated luminosity (ref. [69])	2.6%
Theoretical uncertainties:	
PDF	2.6–7.5%
Scale	0.2–7.9%
$H \rightarrow \gamma^* \gamma \rightarrow \ell\ell\gamma$ branching fraction	10%
Signal modeling:	
Pilup reweighting	0.8%
Trigger efficiency, muon (electron) channel	4 (2)%
Muon reconstruction efficiency	11%
Electron reconstruction efficiency	3.5%
Photon reconstruction efficiency	0.6%
$m_{\ell\ell\gamma}$ scale, muon (electron) channel	0.1 (0.5)%
$m_{\ell\ell\gamma}$ resolution, muon (electron) channel	10 (10)%

### 3.7.1. Photons

Photons in this analysis are well identified, isolated and have large transverse energy. Calibration for such photons was well understood in CMS for the purpose of  $H \rightarrow \gamma\gamma$  search. The uncertainty due to energy scale and resolution of the photons is discussed in detail in  $H \rightarrow \gamma\gamma$  legacy paper [52], and here we use those results. The uncertainties taken from Ref. [52] and propagated to the signal MC sample result in  $< 1\%$  uncertainty on the width of the Higgs peak and  $< 0.06\%$  on its mean (scale), which are quite small compared to the other uncertainties of the analysis.

### 3.7.2. Dimuon ID efficiency from $J/\psi \rightarrow \mu\mu$ events

In order to derive the uncertainty due to muon reconstruction efficiency we need a way to determine this efficiency in data. Usually,  $Z \rightarrow \mu\mu$  events are used to do this job, but in our case there is no Z-peak, since  $m_{\mu\mu} < 20$  GeV. Hence, we make use of  $J/\psi \rightarrow \mu\mu$  peak data events in order to extract these efficiencies. Moreover, the two muons are close to each other and anti-correlated in  $p_T$ , due to the selection requirements applied. Therefore, we do not attempt to derive the efficiency per-muon, instead we get them per-event.

In order to obtain unbiased results we use a statistically independent dataset triggered by the double-photon trigger for this study. From this dataset we select events that have a photon with  $p_T > 40$  GeV and two muons with  $p_T^1 > 23$  GeV and  $p_T^2 > 4$  GeV, using the most trivial muon ID, the **tracker** (TR) ID. *No ID criteria is applied to the photon in order to factorize its efficiency.* We also require  $\Delta R(\mu, \gamma) > 0.4$  for each selected muon. We then plot the dimuons mass distributions, as shown in Fig. 3.15 (left). After that, we apply the muon ID criteria used in the analysis, i.e. **loose** ID, described in Section 3.4; and finally we select events, which pass the Mu22\_Ph022 trigger (TRIG). After both those selections we also plot the  $m_{\mu\mu}$  distribution, shown in Fig. 3.15.

The  $J/\psi \rightarrow \mu\mu$  peak is clearly seen in all three distributions and we extract the number of  $J/\psi$  events from them. This is done by subtracting the background within the  $J/\psi$  region, which in turn is estimated by a fit to a third order polynomial in the side-bands. The result is the three numbers,  $N_{TR}$ ,  $N_{ID}$  and  $N_{TRIG}$ , presented in Table 3.12. The dimuon reconstruction efficiency is now determined as the ratios,  $\varepsilon_{ID} = \frac{N_{ID}}{N_{TR}}$  and  $\varepsilon_{TRIG} = \frac{N_{TRIG}}{N_{ID}}$ , and it is also shown in Table 3.12. Notice that this is a per-event

efficiency, not a per-muon efficiency. The uncertainty on these efficiencies are statistical and come from the uncertainty on the number of  $J/\psi$  events extracted from the fits.

In the MC signal sample the determination of efficiencies is straightforward, since we have true information at generator level. Similar to what was described above, we use two muon IDs: **tracker** and **loose**, and the trigger selection at the end. For each selection we plot directly the efficiencies vs  $m_{\mu\mu}$  using the MC sample of  $m_H = 125$  GeV, as shown in Fig. 3.16. Here efficiencies are defined as:  $\varepsilon_{TR} = \frac{N_{TR}}{N_{Acc}}$ ,  $\varepsilon_{ID} = \frac{N_{ID}}{N_{TR}}$ ,  $\varepsilon_{TRIG} = \frac{N_{TRIG}}{N_{ID}}$ ,

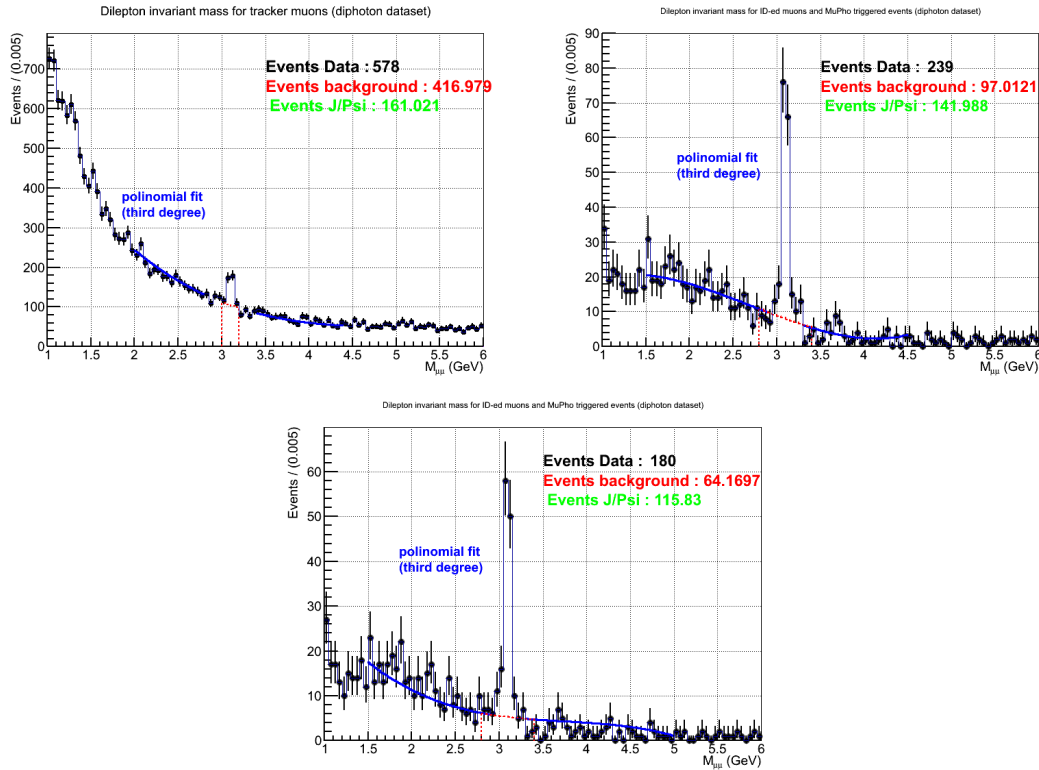


Figure 3.15. Dimuon invariant mass distributions with different muon IDs from the Double Photon dataset; Top-left: tracker ID muons; top-right: loose ID (i.e. analysis muon); bottom: ID plus MuEG trigger. A polynomial fit is applied to the side-bands in order to estimate the background in the region of the  $J/\psi$  resonance, thus extracting the  $J/\psi$  yield.

where  $N_{Acc}$  is the number of events with generator level particles in kinematic acceptance (this can only be obtained in MC). We can see a dependence of those efficiencies on the dimuon invariant mass. In order to be consistent with the results obtained in data we should take the numbers at around  $m_{\mu\mu} = 3.1$  GeV, which are presented in Table 3.12.

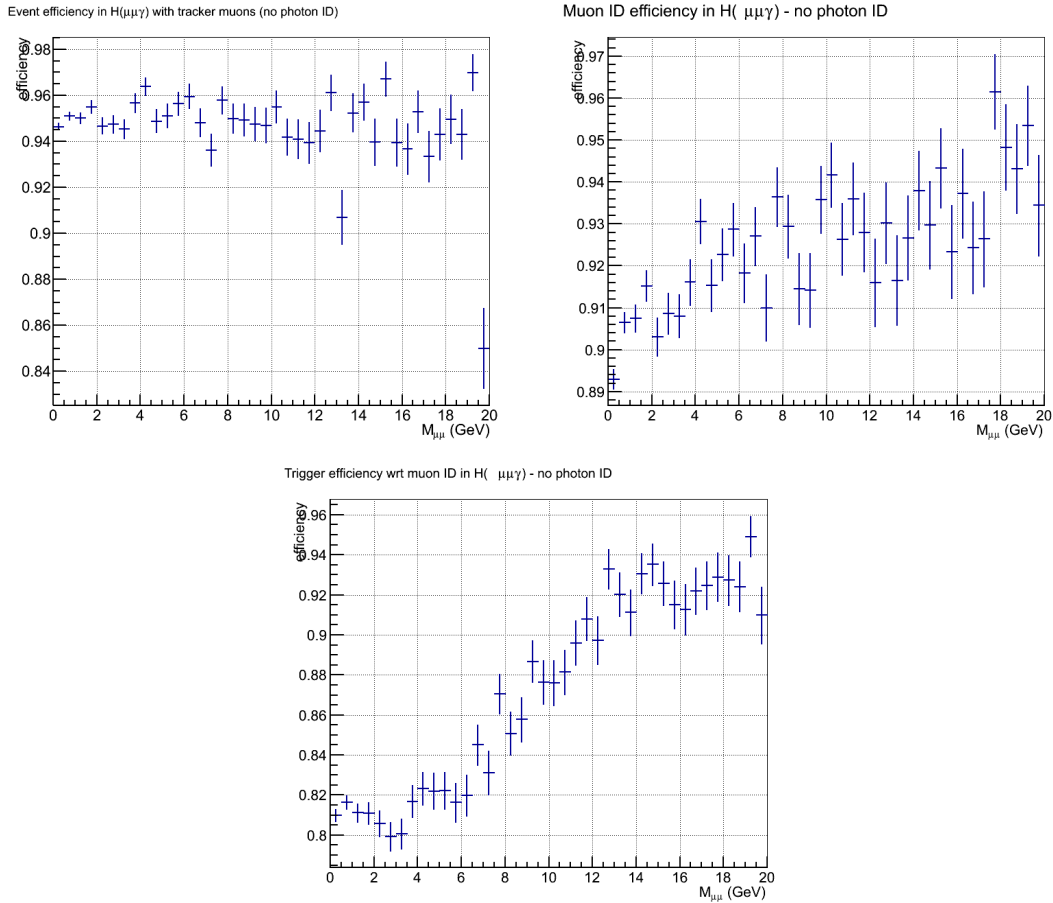


Figure 3.16. Event efficiency associated with a specific muon ID selection (other sources are factored out) vs dimuon invariant mass in MC signal sample. Top-left: tracker muon ID; top-right: loose muon ID, as adopted in the analysis (the tracker muon is implicitly a part of the full ID). Bottom: event trigger efficiency associated with the muon part of the trigger used in the analysis.



Table 3.12. Per-event efficiency due to Muon ID.  $J/\psi$  yield in data is extracted from the Double Photon dataset, as described in text.

Muon ID	$J/\psi$ yield	Per-event efficiency, %	
		Data	MC at $m_{\mu\mu} = 3.1$ GeV
Tracker muon	$161 \pm 16$	-	95
+ <i>Loose</i>	$142 \pm 10$	$88 \pm 9$	96
+ Mu22_Ph022 trigger	$116 \pm 5$	$82 \pm 4$	80

We should note that the **loose ID** efficiency is obtained with respect to the *tracker* ID. We don't have a way to determine the tracker ID efficiency in data. However, we do know it in the MC sample, it is  $\sim 95\%$  and mostly independent of  $m_{\mu\mu}$ , as shown in Fig. 3.16 (left). Thus, being conservative, we assign another 5% uncertainty to the dimuon ID efficiency.

In conclusion, for the dimuon ID from data we obtain  $\varepsilon_{ID} = 0.88 \pm 0.10$ , which we declare consistent with the efficiency in MC,  $\varepsilon_{ID} = 0.96$ , and do not apply any MC/data scale factors. Instead we assign an 11% systematic uncertainty on the MC signal yield.

There is a caveat with the trigger efficiency obtained with this method: in the data it only accounts for the Mu22 leg of the Mu22\_Ph022 trigger, used in the main analysis, because the double-photon trigger has tighter photon ID. In order to estimate the efficiency of the Pho22 leg we make use of yet another dataset, triggered by the single muon trigger **Single\_MuIso**, and select events that pass the full analysis selection (without the trigger requirement). Then, the ratio of the number of events triggered with (**Single\_MuIso** + Mu22\_Ph022) to the number of events triggered only by **Single\_MuIso** gives the trigger efficiency for the Pho22 part of the Mu22\_Ph022 trigger (that is what we want). We can do the same in the signal MC. Finally we get:  $\varepsilon_{Data}^{Pho22} = 0.975 \pm 0.007$  and

$\varepsilon_{MC}^{Pho22} = 0.9992 \pm 0.0002$ . The 2% difference is assigned as another systematic uncertainty due to the Mu22\_Ph22 trigger efficiency.

### 3.7.3. Muon momentum scale and resolution from $J/\psi \rightarrow \mu\mu$

It is common for CMS simulation that the resolution of Monte Carlo samples is better than it is in real data. Hence, a smearing correction is applied to muons and photons. In addition to this correction, a corresponding uncertainty is assigned. The uncertainty provided with the standard muon momentum corrections are small – when propagated to Higgs mass in MC sample it yields to less than 1% difference in the width and less than 0.05% in the mean. However, those corrections were derived from  $Z \rightarrow \mu\mu$  events, in mass window,  $60 < m_{\mu\mu} < 120$  GeV, and for the muons with  $p_T^\mu > 20$  GeV, hence they do not fully cover our kinematics (low dimuon invariant mass and low trailing muon  $p_T$ .) Therefore, in order to make sure that the scale and resolution of the muons are good, we once again make use of the  $J/\psi \rightarrow \mu\mu$  events in data. (And we also use the  $H \rightarrow (J/\psi)\gamma \rightarrow \mu\mu\gamma$  MC signal sample for this study). Indeed, looking at Fig. 3.17, one can see that  $J/\psi \rightarrow \mu\mu$  peak is narrower in the MC sample than in data. Events in those plots have a photon with  $p_T > 40$  GeV, two muons with  $p_T^1 > 23$  GeV,  $p_T^2 > 4$  GeV, and  $p_T^{\mu\mu} > 40$  GeV, which is close to the selection in the main analysis. The muon momentum corrections have been applied.

To quantify the scale and resolution, we fit the  $J/\psi$  peak in MC with a Breit-Wigner function convoluted with the Guassian:

$$f_{J/\psi}(m, \sigma) = BW(m, \Delta) \otimes \mathcal{G}(0, \sigma),$$

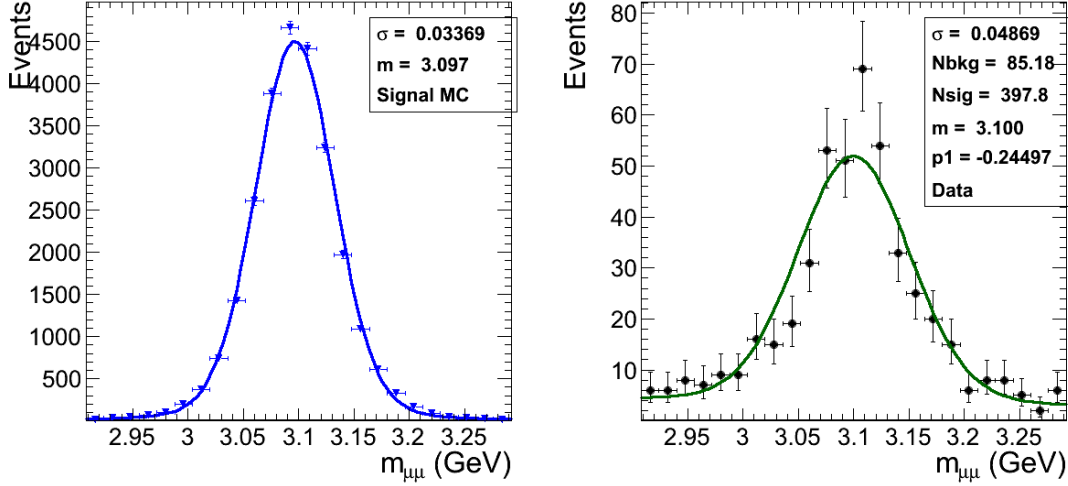


Figure 3.17.  $J/\psi \rightarrow \mu\mu$  peak and the fits in the  $H \rightarrow J/\psi\gamma \rightarrow \mu\mu\gamma$  MC sample (left) and data events (right).

where parameter  $\Delta$  is fixed to 0.01, while  $m$  and  $\sigma$  are subject to the fit. For the data events, the fit contains a linear background contribution:

$$f_{data} = N_{sig} \times f_{J/\psi}(m, \sigma) + N_{bkg} \times (1 + p_1 m).$$

The following resolution from the fit are obtained:  $\sigma_{MC} = 34$  MeV,  $\sigma_{data} = 49$  MeV. This difference suggests that there is indeed a residual resolution difference not accounted for in the MC sample. We do not attempt to derive a new corrections for this. Instead we assign an uncertainty on the resolution of the Higgs boson candidate mass, of 10%, which covers any possible differences in resolution between data and simulation (including the uncertainties due to photon energy resolution).

### 3.7.4. Electron ID, Energy Scale and Resolution

Unfortunately, there is no  $J/\psi \rightarrow ee$  peak available in the electron channel. This is due to the trigger and electron ID implemented in the analysis, which effectively lead to  $m_{ee} < 1.5 \text{ GeV}$  selection, see Fig. 3.5. Hence, we don't have a method of estimating electron ID efficiency in data. Instead, we make use of various simulation samples to evaluate the relevant systematic uncertainties. We follow the approach developed in [52] and produce the MC signal samples, varying parameters of the simulation:

- the tracker material budget;
- the underlying event modeling;
- the pile-up simulation.

In each of those samples we can measure the electron ID efficiency and assign the largest difference as systematic. The total uncertainty on the dielectron ID obtained from these studies is 3.5%.

As for the energy scale and resolution, we use a 10% uncertainty on the width and 0.5% on the scale, same as in muon channel analysis.

## CHAPTER 4

### Results

Due to the absence of a signal, the data are used to derive upper limits on the Higgs boson production cross section times the branching fraction,  $\sigma(\text{pp} \rightarrow \text{H}) \times \mathcal{B}(\text{H} \rightarrow \gamma^* \gamma \rightarrow \ell\ell\gamma)$ , divided by that expected for a SM Higgs boson, for  $m_{\ell\ell} < 20 \text{ GeV}$ . No significant excess above background is observed in the full mass range,  $120 < m_{\text{H}} < 150 \text{ GeV}$ , with a maximum excess of less than two standard deviations. In the electron channel a correction is made to account for the events that are removed by the requirement of  $m_{\text{ee}} < 1.5 \text{ GeV}$  due to the trigger and reconstruction inefficiencies described above. The exclusion limits are calculated using the modified frequentist  $\text{CL}_s$  method, as described in Sec. 3.6. An unbinned evaluation over the full mass range of data is used, as shown in Figs. 3.7 and 3.10. The uncertainty in the limit is dominated by the size of the data sample. The systematic uncertainties have a small impact, which effect is further quantified in Appendix E.

#### 4.1. Muon channel

In the muon channel, the 95% CL exclusion upper limits are shown in Fig. 4.1, separately for three event categories, and their combination. The limits are calculated for  $m_{\text{H}}$  hypotheses in the 120–150 GeV range with 1 GeV intervals. In the main *EB* category the expected exclusion limits are between 7 and 13 times the SM prediction depending on  $m_{\text{H}}$ . Combination with two other categories improves the limit by about 6%. For instance, at  $m_{\text{H}} = 125 \text{ GeV}$  the median expected upper limit of the *EB* category alone is  $\sim 7.6$  times

the SM prediction and it improves to  $\sim 7.2 \times \text{SM}$  when the three categories are combined. The observed limit for  $m_H = 125 \text{ GeV}$  is  $\sim 10.8 \times \text{SM}$  prediction for *EB* category alone and it degrades a little, to  $\sim 10.9 \times \text{SM}$  for the combination.

#### 4.2. Combination with the Electron Channel

As expected, the sensitivity of the electron channel is weaker than of the muon channel. On the top-right of the Fig. 4.2 the 95% CL exclusion limit is shown for the electron channel alone. For comparison, the limits in the muon channel of the *EB* category with the same  $y$ -axis scale is shown on the left of the same figure. For the combination of the muon and electron channels only the *EB* category of the muon channel is used. The resulting upper limit plot is presented on the bottom of the Fig. 4.2. The observed (expected) 95% CL upper limit for  $m_H = 125 \text{ GeV}$  is  $6.7$  ( $5.9^{+2.8}_{-1.8}$ ) times the SM prediction.

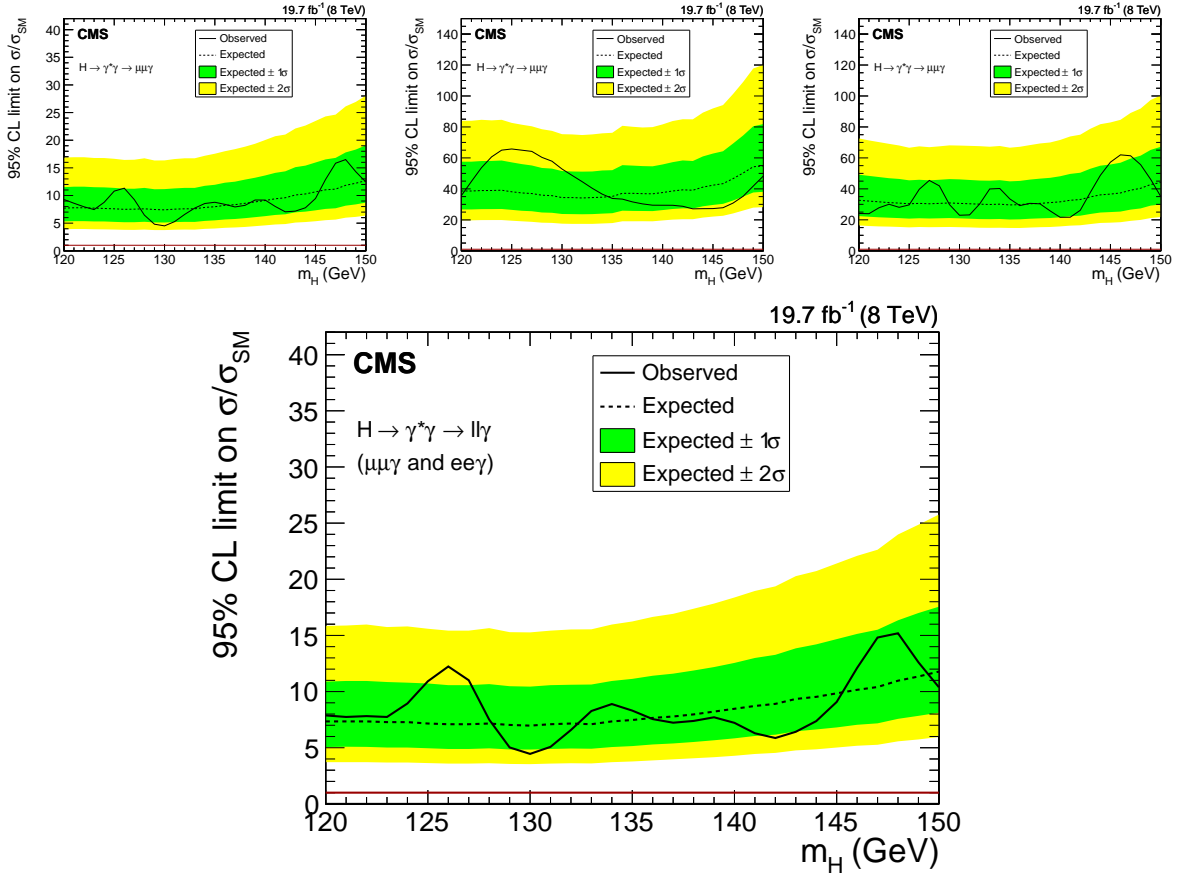


Figure 4.1. Exclusion upper limit at 95% CL on the cross section times the branching fraction for  $H \rightarrow \mu\mu\gamma$  decay of a Higgs boson divided by the SM prediction ( $\mu$ -value). Top plots show three categories:  $EB$ ,  $EE$ ,  $mll50$ . Bottom plot shows the combination of them. The result is dominated by the most sensitive,  $EB$  category.



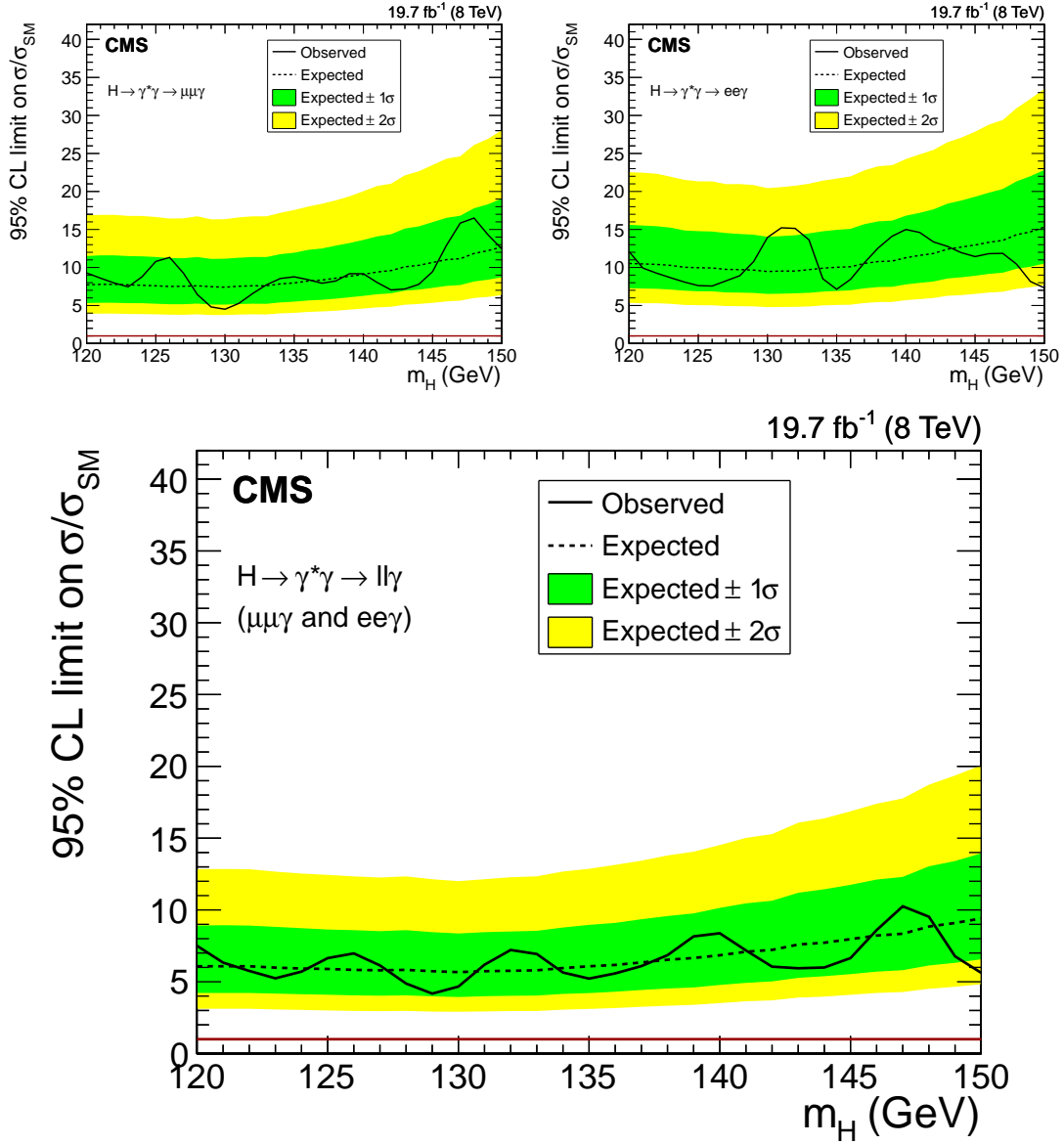


Figure 4.2. The 95% CL exclusion upper limit, as a function of the mass hypothesis,  $m_H$ , on the  $\sigma/\sigma_{SM}$ , the cross section times the branching fraction of a Higgs-like particle decaying into a photon and a lepton pair with  $m_{\ell\ell} < 20$  GeV, divided by the SM value. (Upper) left: muon, right: electron channels; (lower) a statistical combination of the results in the two channels

### 4.3. Model independent limits

In addition to the limits on the SM process one can re-interpret the results in a more general way to obtain a limit on the inclusive cross section times the branching fraction of the  $H \rightarrow \ell\ell\gamma$  decay, where  $H$  now denotes a Higgs-like scalar particle of any BSM theory. No theoretical uncertainties of the Higgs boson production cross sections are needed for this limit. The result of the 95% CL upper limits is now expressed in femtobarns, and shown in Fig. 4.3. One should use these results with care though. In the muon channel, the total signal efficiency is about 24% and almost independent of the dimuon invariant mass. In the electron channel, efficiency depends on the dielectron mass, since it is strongly shaped by the selection. For this reason, the result in the electron channel is really *not* model independent. In the muon channel, however, it can be interpreted as such. The observed (expected) 95% CL upper limit of 7.3 ( $5.2^{+2.4}_{-1.6}$ ) fb is obtained at  $m_H = 125$  GeV for  $H \rightarrow \mu\mu\gamma$  decay.

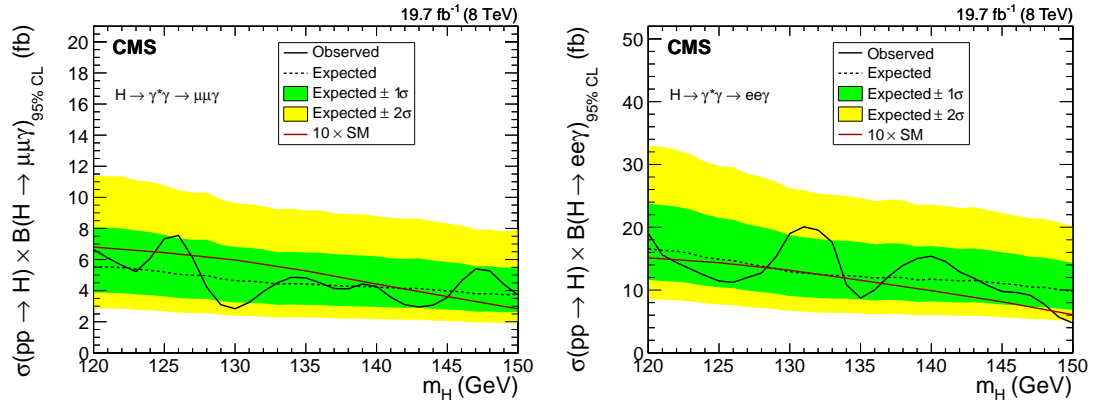


Figure 4.3. The 95% CL exclusion limit on  $\sigma(pp \rightarrow H) \times \mathcal{B}(H \rightarrow \ell\ell\gamma)$ , with  $m_{\ell\ell} < 20$  GeV, for a Higgs-like particle, as a function of the mass hypothesis,  $m_H$ .

#### 4.4. Differential limits in bins of $m_{\mu\mu}$

Since we know of the existence of the Higgs-like particle with 125 GeV mass, it is interesting to look at  $m_H = 125$  GeV specifically and ask for the differential cross section measurements. For example, in  $H \rightarrow \gamma\gamma$  decay the differential cross sections are measured for many kinematic variables, including  $p_T^{\gamma\gamma}$ ,  $|y_{\gamma\gamma}|$  [70]. In our channel, among other variables, it is interesting to perform the differential measurement of the dilepton invariant mass. Currently we are not yet sensitive to the signal, thus instead of measuring the cross section I present a differential limit for it in bins of  $m_{\ell\ell}$ . This is done only in the muon channel because of the shaped  $m_{ee}$  distribution due to selection in the electron channel. In order to produce this result I introduce 7 bins in  $m_{\mu\mu}$  variable, with the edges: 0.2 – 0.5 – 1 – 2 – 4 – 9 – 20 – 50 GeV. These bins are chosen so that they approximately contain the same number of signal events (corresponding to  $\sim 0.1$  fb of  $\sigma \cdot \mathcal{B}$ ). In each of those bins, the fit of the data events to a Bernstein polynomial of degree 4 is performed (see Fig. 4.4). And the upper limits in each bin are determined in the same manner as it is done for the limits presented in the previous section. The result is shown in Figure 4.5.

It is important to note that there is no migration of events between  $m_{\mu\mu}$  bins, therefore no unfolding is necessary. In Appendix D.1.1 I show the resolution of the dimuon mass for every mass bin. The resolution is good, varying from 1.1% in high  $m_{\mu\mu}$  bins to 2.4% in the lowest bin.

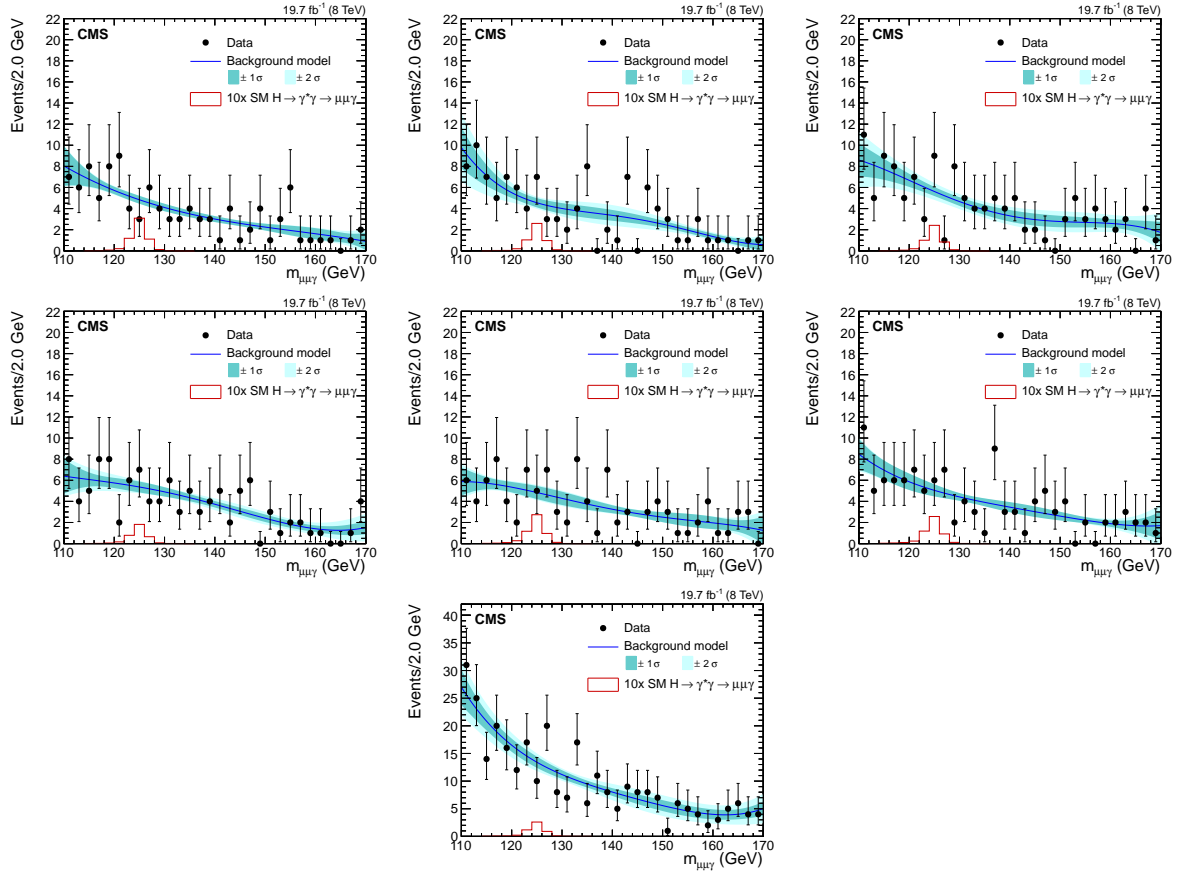


Figure 4.4. Fit to the data events of  $m_{\mu\mu\gamma}$ , where the plots correspond to one of the 7 bins in  $m_{\mu\mu}$  (described in the text and ordered from left to right).

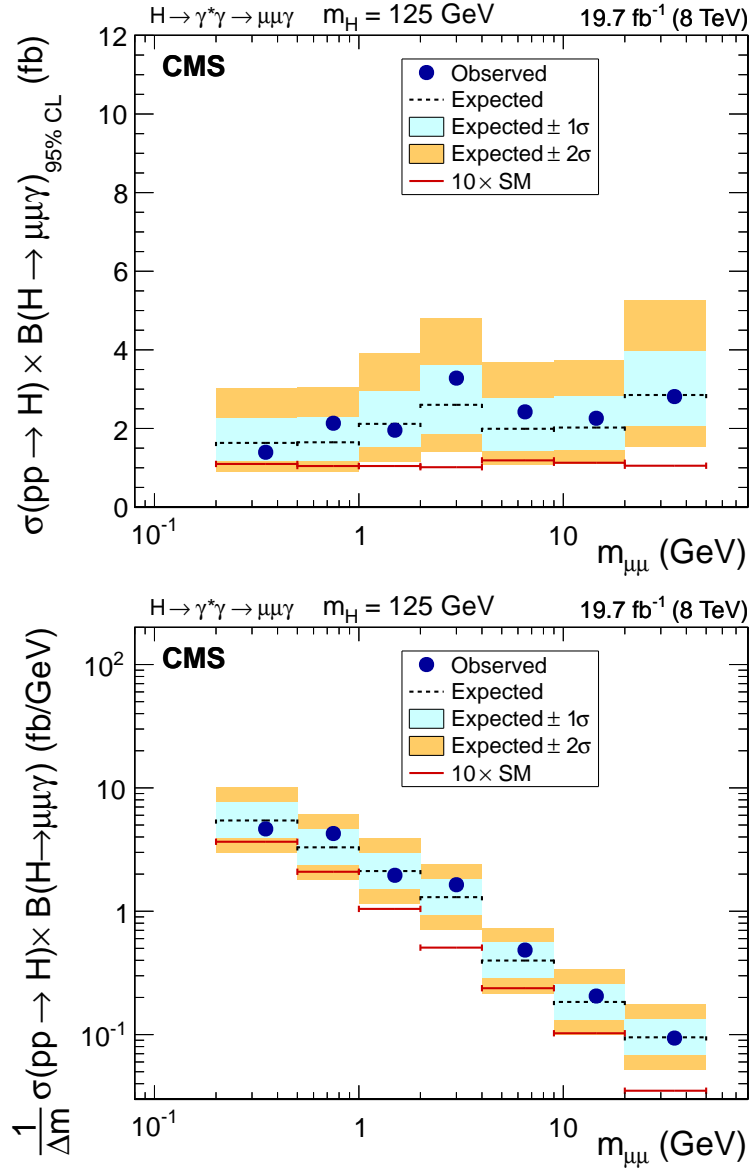


Figure 4.5. Differential limit on the cross section times the branching fraction of a Higgs-like particle  $H$ , with  $m_H = 125$  GeV, decaying into a photon and a muon pair within bins of  $m_{\mu\mu}$ . Two plots show the same result but the second one is scaled by the bin size,  $\Delta m$ , and shown in the logarithmic scale.

#### 4.5. Result for $H \rightarrow (J/\psi)\gamma$

As it is described in Section 3, a region with  $2.9 < m_{\ell\ell} < 3.3$  GeV in the muon channel is selected for a special case – a search for the  $H \rightarrow (J/\psi)\gamma \rightarrow \mu\mu\gamma$  process. After the complete event selection, just like in the muon Dalitz search analysis, the  $m_{\mu\mu\gamma}$  distribution in data is fitted to a Bernstein polynomial of degree 2, in the range  $110 < m_{\mu\mu\gamma} < 150$  GeV, see Figure 3.8. The signal model function is Crystal-Ball plus a Gaussian, and only  $m_H = 125$  GeV is considered.

The 95% CL upper limit is placed on the cross section times the branching fraction,

$$(4.1) \quad \sigma(\text{pp} \rightarrow H) \times \mathcal{B}(H \rightarrow \mu\mu\gamma) < 1.80 \text{ fb},$$

while the expected limit is  $1.90 \pm 0.97$  fb. One can interpret this result as an upper limit on  $\sigma(\text{pp} \rightarrow H) \times \mathcal{B}(H \rightarrow (J/\psi)\gamma \rightarrow \mu\mu\gamma)$  and obtain for the branching fraction,

$$(4.2) \quad \mathcal{B}(H \rightarrow (J/\psi)\gamma) < 1.5 \times 10^{-3}$$

at 95% CL, which is about 540 times the prediction in Ref. [29]. At 90% CL,  $\mathcal{B}(H \rightarrow (J/\psi)\gamma) < 1.2 \times 10^{-3}$ . The number of events present in the 2.9–3.3 GeV mass window coming from the  $H \rightarrow \gamma^*\gamma \rightarrow \mu\mu\gamma$  process is large compared to the  $H \rightarrow (J/\psi)\gamma \rightarrow \mu\mu\gamma$  (see Table 3.3). On the other hand it is small compared to the total background, hence it is considered as a part of the background when extracting the limit on  $\mathcal{B}(H \rightarrow (J/\psi)\gamma)$ . The interference between the  $H \rightarrow \gamma^*\gamma \rightarrow \mu\mu\gamma$  and  $H \rightarrow (J/\psi)\gamma \rightarrow \mu\mu\gamma$  signal processes is negligible due to small  $\Gamma_{J/\psi}/m_{J/\psi}$  ratio.

#### 4.6. Conclusion and outlook

In this dissertation I presented the search analyses of the rare decays of the Higgs boson at CMS:  $H \rightarrow \gamma^* \gamma \rightarrow \ell \ell \gamma$ , where  $\ell = \mu, e$ , and  $H \rightarrow (J/\psi) \gamma \rightarrow \mu \mu \gamma$ . No signal is observed due to insufficient statistical power of the recorded data. The upper limits are set on the decay rate of these processes. For the  $H \rightarrow \gamma^* \gamma$  process the observed limit is 6.7 times the SM prediction, which comes from the combination of the muon and electron channels. This result is dominated by the sensitivity in the muon channel. The sensitivity in the electron channel is suppressed due to the difficulty of reconstructing two close-by electrons that are merged into a single shower in the electromagnetic calorimeter. Nevertheless, it seems important to present the result of the electron channel in the hopes that in the future analysis the techniques and the reconstruction algorithms can be improved and better sensitivity will be achieved. Furthermore, this challenge in the electrons reconstruction can lead to a solution in the design of the future particle detectors.

In the next data taking of the LHC operation, in addition to a higher collision energy, the increase of the integrated luminosity is anticipated. In the Run-2, the LHC plans to deliver  $300 \text{ fb}^{-1}$  of data at  $\sqrt{s} = 13 \text{ TeV}$ , while in the high luminosity (HL) run,  $\mathcal{L}_{int} = 3000 \text{ fb}^{-1}$  is expected. With such luminosity the sensitivity to the SM Higgs boson decay,  $H \rightarrow \gamma^* \gamma$ , will be greatly increased. At  $300 \text{ fb}^{-1}$  one expects to achieve the signal significance greater than  $2\sigma$ , while at  $3000 \text{ fb}^{-1}$  the Higgs boson signal with  $>5\sigma$  significance can be observed. This would allow us to determine the rate of this decay and its compatibility with the SM predictions.

For the  $H \rightarrow (J/\psi) \gamma \rightarrow \mu \mu \gamma$  decay the obtained limit on the branching ratio is  $1.5 \times 10^{-3}$ , which is 540 times higher than the SM prediction. This means that even after the

HL run one would not be sensitive to this decay at the SM rates. It is possible, however, that in some BSM models the  $Hcc$  coupling is larger than it is in the SM. In that case the  $H \rightarrow (J/\psi)\gamma$  could be interesting to look at.

I think further improvements to this analysis can be done. First of all, a better simulation of the background processes is needed. This will allow us to better understand the background composition and could lead to an optimization of the event selection, including the MVA techniques. Secondly, the developments in the electron channel for a better identification of the merged electrons topology could boost the sensitivity. The improvements here could come from further exploitation of the results obtained by CMS for a photon conversion process  $\gamma \rightarrow ee$ . Also, the development of a dedicated trigger for this channel is anticipated, and it is expected to improve the total signal selection efficiency.

I hope you enjoyed the reading of this dissertation. If you have any questions or comments, please send them to me at [Andrey.Pozdnyakov@cern.ch](mailto:Andrey.Pozdnyakov@cern.ch).



## References

- [1] M. E. Peskin and D. V. Schroeder, “An introduction to quantum field theory”. Addison-Wesley, 1995.
- [2] Particle Data Group Collaboration, “Review of Particle Physics”, *Chin. Phys. C* **38** (2014) 090001, doi:10.1088/1674-1137/38/9/090001.
- [3] V. A. Rubakov, “Classical theory of gauge fields”. Princeton University Press, Princeton, N.J, 2002.
- [4] ATLAS Collaboration, “Observation of a new particle in the search for the Standard Model Higgs boson with the ATLAS detector at the LHC”, *Phys. Lett. B* **716** (2012) 1, doi:10.1016/j.physletb.2012.08.020, arXiv:1207.7214.
- [5] CMS Collaboration, “Observation of a new boson at a mass of 125 GeV with the CMS experiment at the LHC”, *Phys. Lett. B* **716** (2012) 30, doi:10.1016/j.physletb.2012.08.021, arXiv:1207.7235.
- [6] O. Brüning, H. Burkhardt, and S. Myers, “The Large Hadron Collider”, *Prog. Part. Nucl. Phys.* **67** (2012), no. CERN-ATS-2012-064, 705.
- [7] A. D. Martin, W. J. Stirling, R. S. Thorne, and G. Watt, “Parton distributions for the LHC”, *Eur. Phys. J. C* **63** (2009) 189, doi:10.1140/epjc/s10052-009-1072-5, arXiv:0901.0002.
- [8] A. Djouadi, “Higgs Physics: Theory”, *Pramana* **79** (2012) 513–539, doi:10.1007/s12043-012-0361-y, arXiv:1203.4199.
- [9] ATLAS Collaboration, “Measurement of the Inelastic Proton-Proton Cross-Section at  $\sqrt{s} = 7$  TeV with the ATLAS Detector”, *Nature Commun.* **2** (2011) 463, doi:10.1038/ncomms1472, arXiv:1104.0326.

- [10] CMS Collaboration, “Measurement of the inelastic proton-proton cross section at  $\sqrt{s} = 7$  TeV”, *Phys. Lett. B* **722** (2013) 5–27, doi:10.1016/j.physletb.2013.03.024, arXiv:1210.6718.
- [11] CMS Collaboration, “Summaries of CMS cross section measurements”.  
<https://twiki.cern.ch/twiki/bin/view/CMSPublic/PhysicsResultsCombined>.
- [12] A. Pozdnyakov, “Fermionic decays of SM Higgs”, in *XXXIV Physics in Collision*. SLAC eCONF, 2014. arXiv:1411.1981.
- [13] A. Abbasabadi, D. Bowser-Chao, D. A. Dicus, and W. W. Repko, “Radiative Higgs boson decays  $H \rightarrow ff\gamma$ ”, *Phys. Rev. D* **55** (1997) 5647, doi:10.1103/PhysRevD.55.5647, arXiv:hep-ph/9611209.
- [14] D. A. Dicus and W. W. Repko, “Calculation of the decay  $H \rightarrow e\bar{e}\gamma$ ”, *Phys. Rev. D* **87** (2013) 077301, doi:10.1103/PhysRevD.87.077301, arXiv:1302.2159.
- [15] L. B. Chen, C. F. Qiao, and R. L. Zhu, “Reconstructing the 125 GeV SM Higgs boson through  $\ell\bar{\ell}\gamma$ ”, *Phys. Lett. B* **726** (2013) 306, doi:10.1016/j.physletb.2013.08.050, arXiv:1211.6058.
- [16] G. Passarino, “Higgs Boson Production and Decay: Dalitz Sector”, *Phys. Lett. B* **727** (2013) 424–431, doi:10.1016/j.physletb.2013.10.052, arXiv:1308.0422.
- [17] Y. Sun, H. Chang, and D. Gao, “Higgs decays to  $\gamma\ell^+\ell^-$  in the standard model”, *JHEP* **05** (2013) 061, doi:10.1007/JHEP05(2013)061, arXiv:1303.2230.
- [18] ATLAS Collaboration, “Search for Higgs boson decays to a photon and a Z boson in pp collisions at  $\sqrt{s}=7$  and 8 TeV with the ATLAS detector”, *Phys. Lett. B* **732** (2014) 8, doi:10.1016/j.physletb.2014.03.015, arXiv:1402.3051.
- [19] CMS Collaboration, “Search for a Higgs boson decaying into a Z and a photon in pp collisions at  $\sqrt{s} = 7$  and 8 TeV”, *Phys. Lett. B* **726** (2013) 587, doi:10.1016/j.physletb.2013.09.057, arXiv:1307.5515.
- [20] ATLAS Collaboration, “Search for the Standard Model Higgs boson decay to  $\mu^+\mu^-$  with the ATLAS detector”, *Phys. Lett. B* **738** (2014) 68, doi:10.1016/j.physletb.2014.09.008, arXiv:1406.7663.
- [21] CMS Collaboration, “Search for a standard model-like Higgs boson in the  $\mu^+\mu^-$  and  $e^+e^-$  decay channels at the LHC”, arXiv:1410.6679.

- [22] A. Firan and R. Stroynowski, “Internal conversions in Higgs decays to two photons”, *Phys. Rev. D* **76** (2007) 057301, doi:10.1103/PhysRevD.76.057301, arXiv:0704.3987.
- [23] D. A. Dicus and W. W. Repko, “Dalitz decay  $H \rightarrow f\bar{f}\gamma$  as a background for  $H \rightarrow \gamma\gamma$ ”, *Phys. Rev. D* **89** (2014) 093013, doi:10.1103/PhysRevD.89.093013, arXiv:1402.5317.
- [24] LHC Higgs Cross Section Working Group Collaboration, “Handbook of LHC Higgs Cross Sections: 3. Higgs Properties”, doi:10.5170/CERN-2013-004, arXiv:1307.1347.
- [25] J. Campbell and R. Ellis, “MCFM for the Tevatron and the LHC”, *Nuclear Physics B - Proceedings Supplements* (2010) doi:10.1016/j.nuclphysbps.2010.08.011.
- [26] A. Korchin and V. Kovalchuk, “Angular distribution and forward-backward asymmetry of the Higgs-boson decay to photon and lepton pair”, *Eur. Phys. J. C* **74** (2014) doi:10.1140/epjc/s10052-014-3141-7.
- [27] A. Abbasabadi, D. Bowser-Chao, D. A. Dicus, and W. W. Repko, “Higgs-boson<sup>\*</sup>photon associated production at  $e\bar{e}$  colliders”, *Phys. Rev. D* **52** (Oct, 1995) 3919–3928, doi:10.1103/PhysRevD.52.3919.
- [28] G. T. Bodwin, F. Petriello, S. Stoynev, and M. Velasco, “Higgs boson decays to quarkonia and the  $H\bar{c}c$  coupling”, *Phys. Rev. D* **88** (2013) 053003, doi:10.1103/PhysRevD.88.053003, arXiv:1306.5770.
- [29] G. T. Bodwin et al., “Relativistic corrections to Higgs boson decays to quarkonia”, *Phys. Rev. D* **90** (2014) 1130, doi:10.1103/PhysRevD.90.113010, arXiv:1407.6695.
- [30] ATLAS Collaboration, “Search for Higgs and Z boson decays to  $J/\Psi\gamma$  and  $\Upsilon(nS)\gamma$  with the ATLAS detector”, *Phys. Rev. Lett.* **114** (2015) 121801, doi:10.1103/PhysRevLett.114.121801, arXiv:1501.03276.
- [31] G. Perez, Y. Soreq, E. Stamou, and K. Tobioka, “Constraining the Charm Yukawa and Higgs-quark Universality”, arXiv:1503.00290.
- [32] CMS Collaboration, “The CMS experiment at the CERN LHC”, *JINST* **3** (2008) S08004, doi:10.1088/1748-0221/3/08/S08004.
- [33] CMS Collaboration, “Studies of Tracker Material”, Technical Report CMS-PAS-TRK-10-003, 2010.

- [34] CMS Collaboration, “Description and performance of track and primary-vertex reconstruction with the CMS tracker”, *JINST* **9** (2014) P10009, doi:10.1088/1748-0221/9/10/P10009, arXiv:1405.6569.
- [35] P. Goldenzweig, “Operational Experience with the CMS Hadronic Calorimeter in the 2011 LHC run”, *Journal of Physics: Conference Series* **404** (2012), no. 1, 012005, doi:10.1088/1742-6596/404/1/012005.
- [36] O. Jones, “LHC beam instrumentation”, in *Particle Accelerator Conference (PAC07)*. IEEE, 2007.
- [37] P. Forck, P. Kowina, and D. Liakin, “Beam Position Monitors”, in *CERN Accelerator School on Beam Diagnostics*. CERN, 2008.
- [38] O. Brüning et al., “LHC Design Report Vol.1: The LHC Main Ring”, technical report, 2004.
- [39] “EG&G ORTEC Model 935 Quad Constant-Fraction 200 MHz Discriminator”, <http://www.ortec-online.com/download/935.pdf>.
- [40] Lecroy, “WaveRunner Xi-A/MXi-A oscilloscopes”. <http://teledynelecroy.com>.
- [41] “DIP and DIM”. <http://j2eeps.cern.ch/wikis/display/EN/DIP+and+DIM>.
- [42] LHC, “LHC Configuration Vistar”. <http://op-webtools.web.cern.ch>.
- [43] J. Alwall et al., “MadGraph 5 : Going Beyond”, *JHEP* **06** (2011) 128, doi:10.1007/JHEP06(2011)128, arXiv:1106.0522.
- [44] T. Corbett, O. J. P. Éboli, J. Gonzalez-Fraile, and M. C. Gonzalez-Garcia, “Constraining anomalous Higgs boson interactions”, *Phys. Rev. D* **86** (Oct, 2012) 075013, doi:10.1103/PhysRevD.86.075013.
- [45] T. Sjöstrand, S. Mrenna, and P. Z. Skands, “PYTHIA 6.4 physics and manual”, *JHEP* **05** (2006) 026, doi:10.1088/1126-6708/2006/05/026, arXiv:hep-ph/0603175.
- [46] J. Pumplin et al., “New generation of parton distributions with uncertainties from global QCD analysis”, *JHEP* **0207** (2002) 012, doi:10.1088/1126-6708/2002/07/012, arXiv:hep-ph/0201195.

- [47] T. Sjöstrand, S. Mrenna, and P. Z. Skands, “A brief introduction to PYTHIA 8.1”, *Comput. Phys. Commun.* **178** (2008) 852, doi:10.1016/j.cpc.2008.01.036, arXiv:0710.3820.
- [48] “Introduction to jet-parton matching in MG/ME”.  
<https://cp3.irmp.ucl.ac.be/projects/madgraph/wiki/IntroMatching>.
- [49] CMS Collaboration, “Particle flow Event Reconstruction in CMS and Performance for Jets, Taus, and  $E_T^{\text{miss}}$ ”, CMS Physics Analysis Summary CMS-PAS-PFT-09-001, 2009.
- [50] CMS Collaboration, “Commissioning of the Particle-flow Event Reconstruction with the first LHC collisions recorded in the CMS detector”, CMS Physics Analysis Summary CMS-PAS-PFT-10-001, 2010.
- [51] CMS Collaboration, “Performance of photon reconstruction and identification with the CMS detector in proton-proton collisions at  $\sqrt{s} = 8$  TeV”, (2015).  
arXiv:1502.02702.
- [52] CMS Collaboration, “Observation of the diphoton decay of the Higgs boson and measurement of its properties”, *Eur. Phys. J.* **C74** (2014), no. 10, 3076, doi:10.1140/epjc/s10052-014-3076-z, arXiv:1407.0558.
- [53] N. Marinelli, “Track finding and identification of converted photons”, Technical Report CMS-NOTE-2006-005, CERN, Geneva, 2006.
- [54] CMS Collaboration, “Performance of CMS muon reconstruction in  $pp$  collision events at  $\sqrt{s} = 7$  TeV”, *JINST* **7** (2012) P10002, doi:10.1088/1748-0221/7/10/P10002, arXiv:1206.4071.
- [55] S. Baffioni et al., “Electron reconstruction in CMS”, *Eur. Phys. J. C* **49** (2007) 1099, doi:10.1140/epjc/s10052-006-0175-5.
- [56] CMS Collaboration, “Electron reconstruction and identification at  $\sqrt{s} = 7$  TeV”, CMS Physics Analysis Summary CMS-PAS-EGM-10-004, CERN, 2010.
- [57] W. Adam, R. Fruhwirth, A. Strandlie, and T. Todor, “Reconstruction of Electrons with the Gaussian-Sum Filter in the CMS Tracker at the LHC”,.
- [58] A. Hoecker et al., “TMVA: Toolkit for Multivariate Data Analysis”, *PoS ACAT* (2007) 040, arXiv:physics/0703039.

- [59] M. Oreglia, “A study of the reactions  $\psi' \rightarrow \gamma\gamma\psi$ ”. PhD thesis, Stanford University, 1980.
- [60] CMS Collaboration, “Procedure for the LHC Higgs boson search combination in summer 2011”, Analysis Note, CERN, 2011.
- [61] J. Neyman and E. S. Pearson, “On the problem of the most efficient tests of statistical hypotheses”, *Royal Society of London Philosophical Transactions Series A* **231** (1933) 289, doi:10.1098/rsta.1933.0009.
- [62] G. Cowan, K. Cranmer, E. Gross, and O. Vitells, “Asymptotic formulae for likelihood-based tests of new physics”, *Eur. Phys. J. C* **71** (2011) 1554, doi:10.1140/epjc/s10052-011-1554-0, arXiv:1007.1727.
- [63] A. L. Read, “Presentation of search results: the  $CL_s$  technique”, *J. Phys. G* **28** (2002) 2693, doi:10.1088/0954-3899/28/10/313.
- [64] T. Junk, “Confidence level computation for combining searches with small statistics”, *Nucl. Instrum. Meth. A* **434** (1999) 435, doi:10.1016/S0168-9002(99)00498-2, arXiv:hep-ex/9902006.
- [65] W. Verkerke and D. P. Kirkby, “The RooFit toolkit for data modeling”, *eConf C0303241* (2003) MOLT007, arXiv:physics/0306116.
- [66] S. Alekhin et al., “The PDF4LHC Working Group Interim Report”, (2011). arXiv:1101.0536.
- [67] M. Botje et al., “The PDF4LHC Working Group Interim Recommendations”, (2011). arXiv:1101.0538.
- [68] R. D. Ball et al., “Impact of Heavy Quark Masses on Parton Distributions and LHC Phenomenology”, *Nucl. Phys. B* **849** (2011) 296, doi:10.1016/j.nuclphysb.2011.03.021, arXiv:1101.1300.
- [69] CMS Collaboration, “CMS luminosity based on pixel cluster counting - Summer 2013 update”, CMS Physics Analysis Summary CMS-PAS-LUM-13-001, CERN, 2013.
- [70] ATLAS Collaboration, “Measurements of fiducial and differential cross sections for Higgs boson production in the diphoton decay channel at  $\sqrt{s} = 8$  TeV with ATLAS”, *JHEP* **1409** (2014) 112, doi:10.1007/JHEP09(2014)112, arXiv:1407.4222.

## APPENDIX A

### $J/\psi$ polarization

In the MC sample of the  $H \rightarrow (J/\psi)\gamma$  process, the  $J/\psi$  is expected to be 100% polarized, since both  $\gamma$  and  $J/\psi$  are spin-one particles and  $H$  has spin-zero. This polarization of  $J/\psi$  is not taken into account in the MC sample (PYTHIA 8), which is produced for the analysis. It can be checked by looking at the distribution of  $\cos\theta$ , where  $\theta$  is the angle between the positive (negative) lepton and the direction of the  $J/\psi$ . The angle has to be obtained at the generator level, before selection and calculated in the rest frame of the  $J/\psi$ , while the direction of  $J/\psi$  is taken from the centre-of-mass frame of the Higgs boson (i.e.  $J/\psi + \gamma$  system). Figure A.1 (left) shows this distribution, compared with  $H \rightarrow \gamma^*\gamma \rightarrow \mu\mu\gamma$  (Dalitz) sample. The  $\gamma^*$  in the Dalitz sample is polarized while the  $J/\psi$  is not. This issue could result in a difference in the event acceptance. In order to estimate this effect, I reweight the MC sample based on that  $\cos\theta$  distribution with per-event weight  $w = (3/4) \times (1 + \cos\theta^2)$ . Figure A.1 (right) shows the distributions after reweighting of the  $H \rightarrow (J/\psi)\gamma$  sample. It confirms the correct implementation of the re-weighting. The signal acceptance decreases by 5.5% once the reweighting is performed, which leads to  $\sim 6.5\%$  decrease in the sensitivity (i.e. an upper limit).

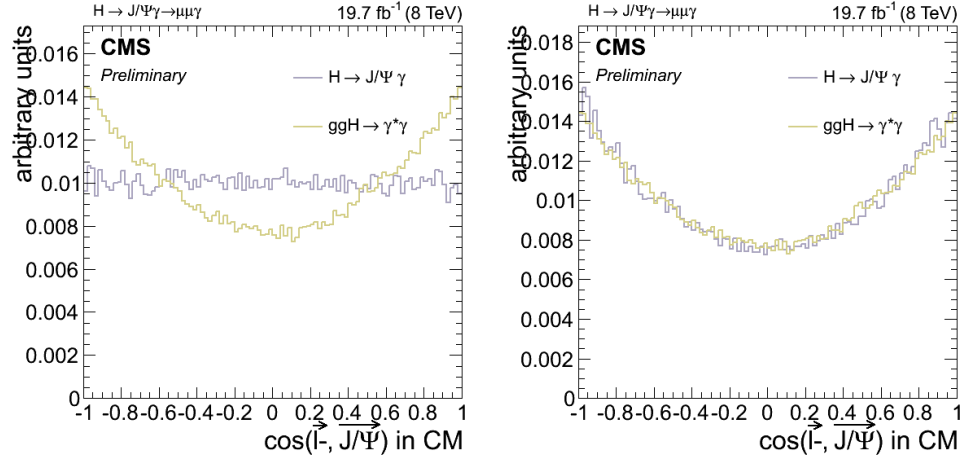


Figure A.1. Distribution of polarization angle from  $J/\psi \rightarrow \mu\mu$  and  $\gamma^* \rightarrow \mu\mu$ . Left: before reweighting of the  $H \rightarrow (J/\psi)\gamma$  sample; right: after reweighting.



## APPENDIX B

### Background Simulation study in Muon Channel

In order to better understand the background composition in the signal region, I have used Monte Carlo simulation and generated two main background processes:  $\gamma^*\gamma$  and  $\gamma^* + jet$ . The first consists of the ISR ( $pp \rightarrow \gamma^* + \gamma \rightarrow \mu\mu\gamma$ ) and FSR ( $pp \rightarrow \gamma^*/Z \rightarrow \mu\mu\gamma$ ) of the Drell–Yan process, with low di-muon invariant mass,  $m_{\mu\mu} < 20$  GeV. The second is an ISR process,  $pp \rightarrow \gamma^* + jet \rightarrow \mu\mu + jet$ , where a jet in the final state is mis-identified as a photon. Further in the text I will refer to those processes as *DYGamma* and *DYJet*, where DY means  $\gamma^*/Z^* \rightarrow \mu\mu$  conversion. Only  $\mu\mu\gamma$  final state is considered for this study.

Both of the above samples are produced starting with MADGRAPH for the tree diagrams generation and then hadronized with PYTHIA 6. In order to avoid double-counting of FSR photons from PYTHIA, the FSR process was disabled during hadronization. for the production of the *DYG* sample. For the *DYJ* sample, for the same reason of avoiding double-counting of the jets, I applied jet-matching settings prescribed in Ref. [48]. This however may not have worked properly (see further discussion). Event pre-selection is applied at the generator level for both samples, which is close to the selection used in the analysis. This is done in order to reduce the number of events produced. Particularly, for the Jet in *DYJ* sample, only  $p_T^j > 35$  GeV and  $|\eta^j| < 1.5$  jets are generated.

The normalization of the MC samples are determined from the fit to the data in a control region (CR), defined as  $60 < m_{\mu\mu\gamma} < 120$  GeV (while all the other cuts are the same

Table B.1. Simulated samples of the background processes for  $\mu\mu\gamma$  final state. Effective cross sections of the samples are determined from the fit to the data in the control region (see text).

Process	tag	$\sigma_{eff}$ , pb
$pp \rightarrow \gamma^*\gamma$	DYG	1.1
$pp \rightarrow \gamma^* + jet$	DYJ	180

as described in Section 3.5). For this fitting I make use of the Z-peak in  $m_{\mu\mu\gamma}$  distribution from the FSR events, and normalize the MC samples to match the data. At the same time we want a good description of the  $m_{\mu\mu}$  distribution, see Fig. B.1. Simultaneous fit to these two distributions leads to an effective cross sections of the samples reported in Table B.1.

Figures B.2 and B.3 show other relevant distributions, from which one can see that the two MC samples do not account for all of the events in data. Overall, about 10% of events are missing and this problem probably comes from the mis-modeling of jets in the *DYJ* sample, see jet distributions on Fig. B.3.

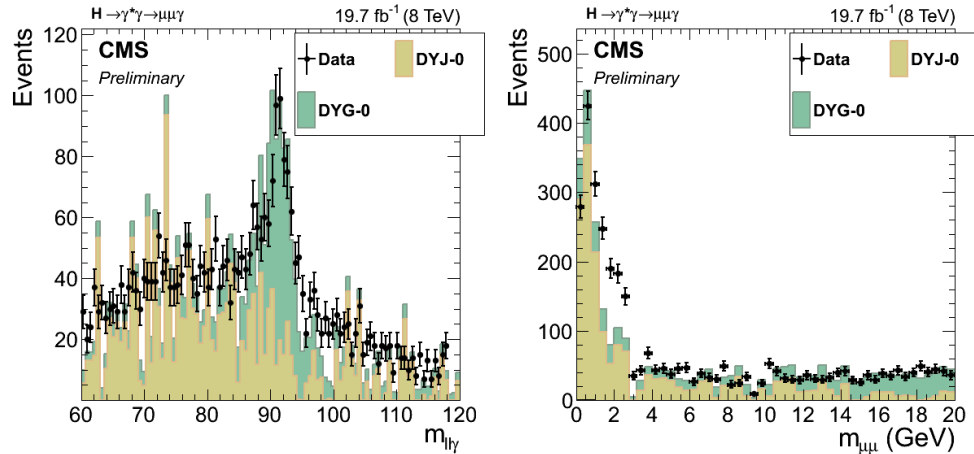


Figure B.1.  $m_{\mu\mu\gamma}$  and  $m_{\mu\mu}$  distributions in the Z peak control region. Background MC samples are normalized in order to simultaneously fit these two distributions.

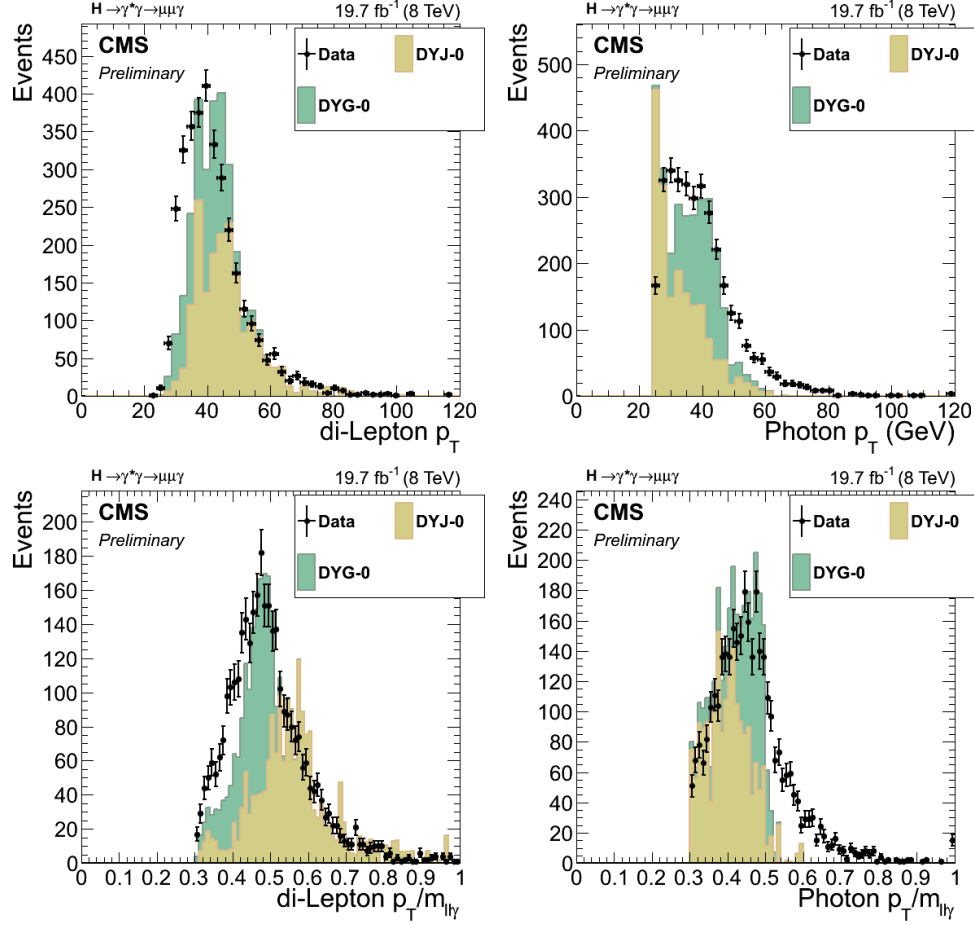


Figure B.2. Dimuon and photon  $p_T$  distributions of events in the Z peak control region.

Nevertheless, we can use this normalization from the CR and see the predictions of the background in the signal region (SR,  $110 < m_{\mu\mu\gamma} < 170$  GeV). The discrepancy between the data and MC becomes larger in SR: about 35% of events are not described by the MC. I think this discrepancy comes from the *DYJ* sample, while *DYG* gives a reliable prediction of the background. Hence, I assume that about 40% of the total background is from *DYG* process. See Figs. B.4 and B.5 for the relevant distributions in the SR and Table B.2 for the event yields in the CR and SR.

Table B.2. Number of events from data and MC backgrounds in the control and signal regions.

	Events, (% of total)			
	data	DYG	DYJ	Other
CR, $60 < m_{\mu\mu\gamma} < 120$ GeV	3372	1833 (54)	1146 (34)	393 (12)
SR, $110 < m_{\mu\mu\gamma} < 170$ GeV	665	272 (41)	177 (27)	216 (32)

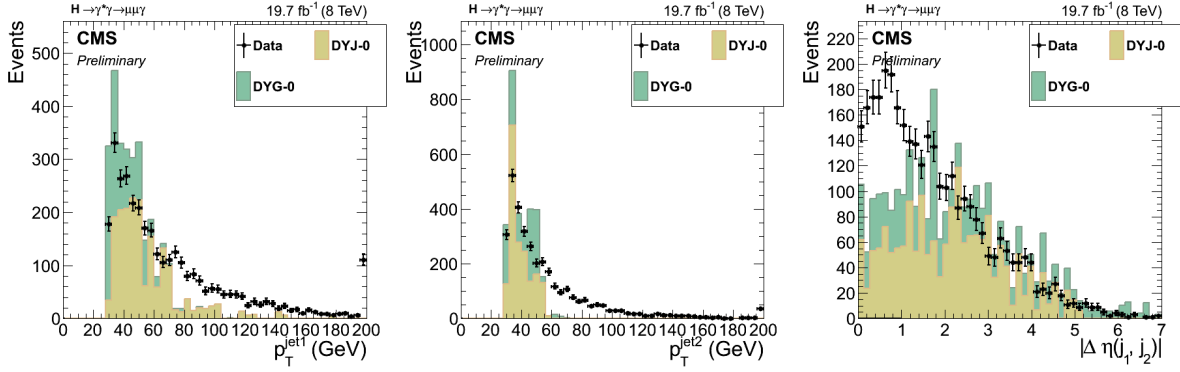


Figure B.3. Distributions of jets'  $p_T$  and  $\Delta\eta$  in the Z peak control region.

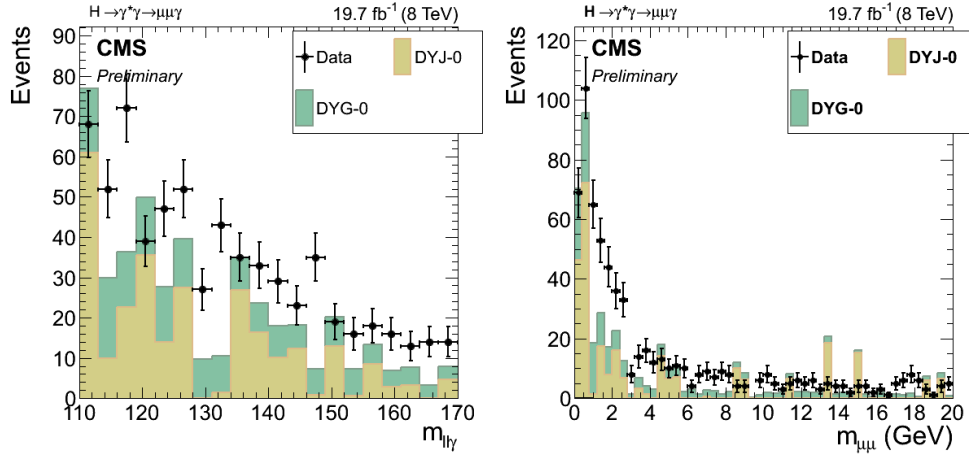


Figure B.4.  $m_{\mu\mu\gamma}$  and  $m_{\mu\mu}$  distributions in the SR, where the background normalization is taken from the CR.

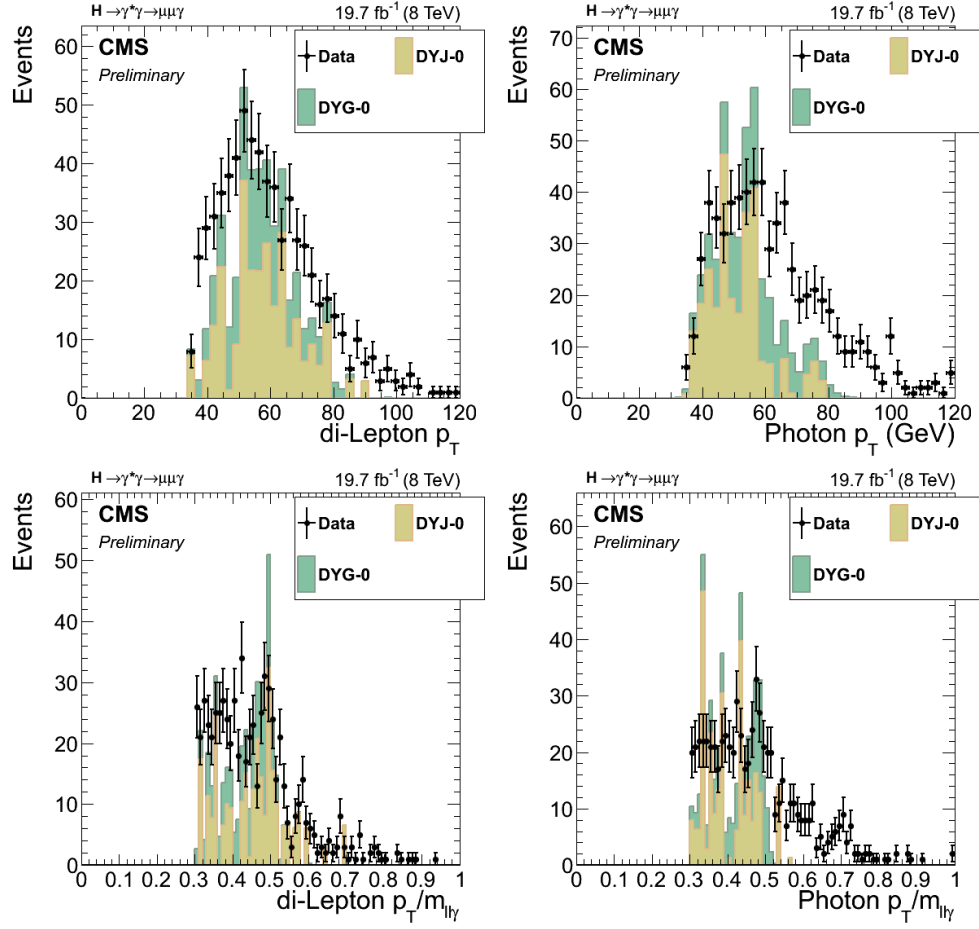


Figure B.5. Dimuon and photon  $p_T$  and  $p_T/m_{\mu\mu\gamma}$  distributions of the events in the signal region.

## APPENDIX C

**Vector Bosons Fusion selection in muon channel**

In the muon channel of the analysis, a separate category for vector bosons fusion (VBF) event topology was considered. The jets used in the VBF tag are reconstructed with PF algorithm, described in Sec. 3.4.2, and their energy is corrected using the techniques described in Ref. [49]. These jets are required to be within  $|\eta| < 4.7$ , and have  $p_T^j > 30$  GeV. Two such jets have to be present in an event.

Three variables are considered to identify the VBF events: difference in  $\eta$ , di-jet invariant mass and a Zeppenfeld variable. The distributions of those variables for the events in data and simulated signal samples are shown in Fig. C.1.

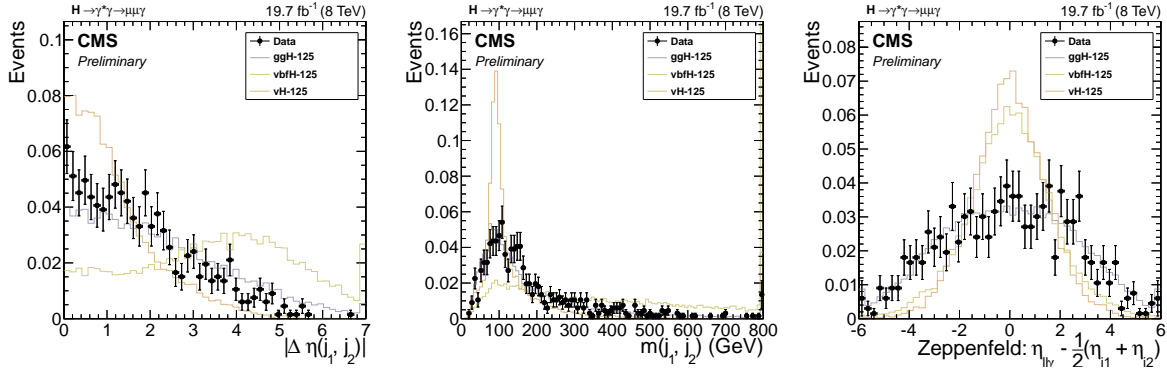


Figure C.1. Input variables for the VBF selection. Signals of three production channels are shown. Signal distributions are independently normalized to the total number of events in data.

The following selection for VBF-like events was chosen:

- $|\eta^{j1} - \eta^{j2}| > 3$ ;

- $m_{jj} > 450 \text{ GeV}$ ;
- $|\eta^{\mu\mu\gamma} - \frac{1}{2}(\eta^{j_1} + \eta^{j_2})| < 4$ .

After this selection we get 0 events in data within a  $122 < m_{\mu\mu\gamma} < 128 \text{ GeV}$  mass window, while expecting 0.08 signal events, see Table C.1 for the yields and Fig. C.2 for the three-body mass distributions. Due to the lack of statistics we are unable to estimate the background by fitting the data, and we don't have a MC background sample either. Because of that and the fact that very little signal is expected, we don't use the VBF category throughout the analysis. Even if this category is used, it would give an insignificant improvement in the limit. One can estimate this with a simple counting experiment as follows. Assuming that the background prediction is  $0.1 \pm 1$  events in the signal region and observed number of events is zero, we can place an upper limit on  $\mu$  at  $\sim 30 \times$  SM prediction for the signal.

Although it is not used at present analysis, this category will be useful in the future data-taking at 13 TeV, with larger statistics.

Table C.1. Event yield after full selection in VBF category.

$m_{\mu\mu\gamma}$ selection, GeV	Data	Total signal	ggH	vbFH	VH
[110, 170]	5	0.09	0.02	0.07	<0.005
[122, 128]	0	0.08	0.02	0.06	<0.005

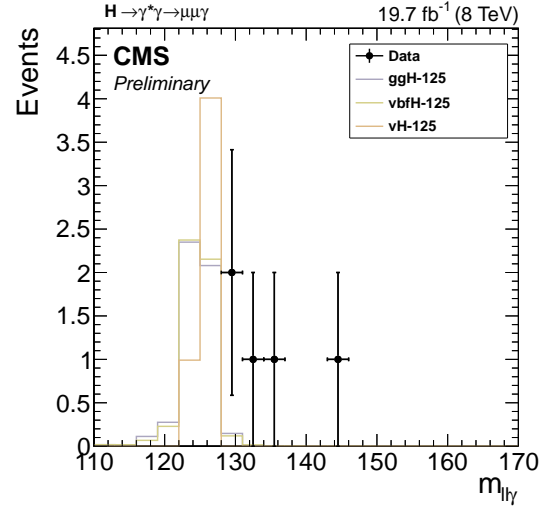


Figure C.2. Three body mass distribution in the VBF category. Signal histograms are independently normalized to the number of events in data.



## APPENDIX D

### Auxiliary information and plots

In this Section I include additional information, which is not necessary for the results presented in the main part of this dissertation, but relevant for a better understanding of the analysis.

#### D.1. Muon channel

The rejection and efficiency of the selection presented in the analysis can be looked at through Table D.1, where the event yields in data and signal are shown after each selection.

Figures D.1 show the key  $m_{\mu\mu}$  distributions. They are plotted after the full selection in three categories denoted by 1 –  $EB$ , 2 –  $EE$ , 3 –  $mll50$  in the Table D.1. Figures D.2–D.12 show additional kinematic distributions relevant in the analysis also split in those three categories. Signal MC distributions (left) from gluon fusion sample are to be compared with data (right), which should be thought of as background.

Table D.1. Event yield after each selection criteria for data and signal with  $m_H = 125$  GeV for  $L = 19.7 \text{ fb}^{-1}$  in the muon channel. Three independent categories of events used in the analysis are also marked.

Category	Selection creteria	Data	Total signal	ggH	vbfH	VH
	Pass Trigger and Photon selection	1.2M	7.86	6.90	0.57	0.39
	Two muons selected	79K	5.89	5.16	0.43	0.29
	$110 < m_{\mu\mu\gamma} < 170$ ; $m_{\mu\mu} < 50$ GeV	3196	5.85	5.13	0.43	0.28
	$\Delta R(\mu, \gamma) > 1$ ; removed $J/\psi$ , $\Upsilon$	2662	5.59	4.93	0.40	0.26
$m_{\mu\mu} < 20$ GeV		1822	4.68	4.12	0.33	0.22
(1) <i>EB</i>	$ \eta_{SC}^\gamma  < 1.4442$	3.67	3.24	0.27	0.16	
	$q_T^{\mu\mu}/m_{\mu\mu\gamma} > 0.3$ , $E_T^\gamma/m_{\mu\mu\gamma} > 0.3$	3.28	2.92	0.22	0.14	
	$122 < m_{\mu\mu\gamma} < 128$ GeV	2.97	2.64	0.20	0.12	
(2) <i>EE</i>	$1.566 <  \eta_{SC}^\gamma  < 2.5$	793	1.00	0.88	0.07	0.06
	$q_T^{\mu\mu}/m_{\mu\mu\gamma} > 0.3$ , $E_T^\gamma/m_{\mu\mu\gamma} > 0.3$	347	0.81	0.71	0.05	0.04
	$122 \text{ GeV} < m_{\mu\mu\gamma} < 128 \text{ GeV}$	57	0.58	0.51	0.04	0.03
$20 \text{ GeV} < m_{\mu\mu} < 50 \text{ GeV}$ ; $ \eta_{SC}^\gamma  < 1.4442$		512	0.72	0.63	0.05	0.03
(3) <i>ml50</i>	$q_T^{\mu\mu}/m_{\mu\mu\gamma} > 0.3$ , $E_T^\gamma/m_{\mu\mu\gamma} > 0.3$	299	0.57	0.51	0.03	0.02
	$122 < m_{\mu\mu\gamma} < 128 \text{ GeV}$	47	0.51	0.46	0.03	0.02

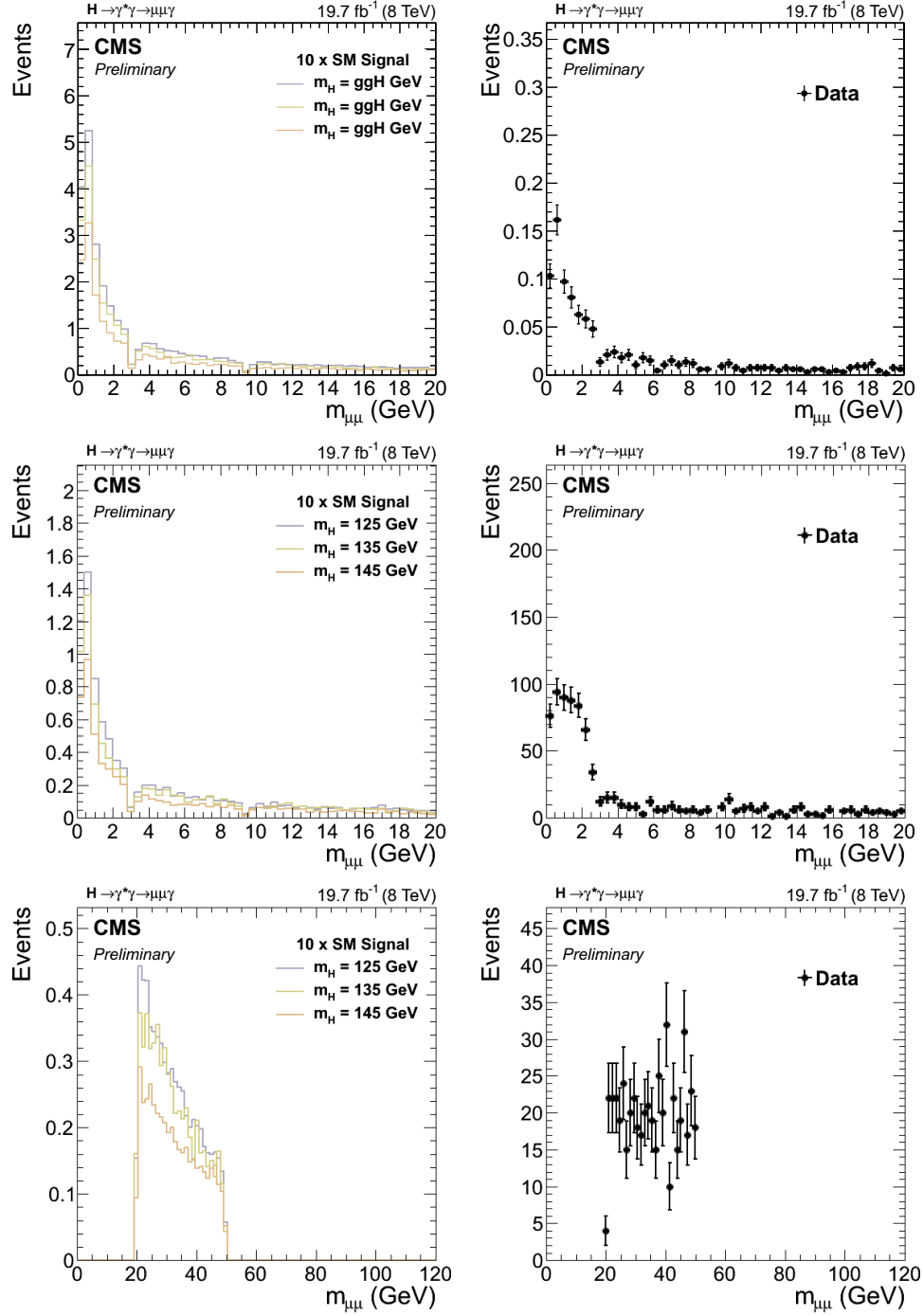


Figure D.1. Distributions of  $m_{\mu\mu}$ , after full selection in  $110 < m_{\mu\mu\gamma} < 170$  GeV window. Rows from top to bottom correspond to categories 1 (top), 2 (middle), 3 (bottom) as described in the text. The ggF signal distributions are shown on the left and scaled by 10. Data is on the right.

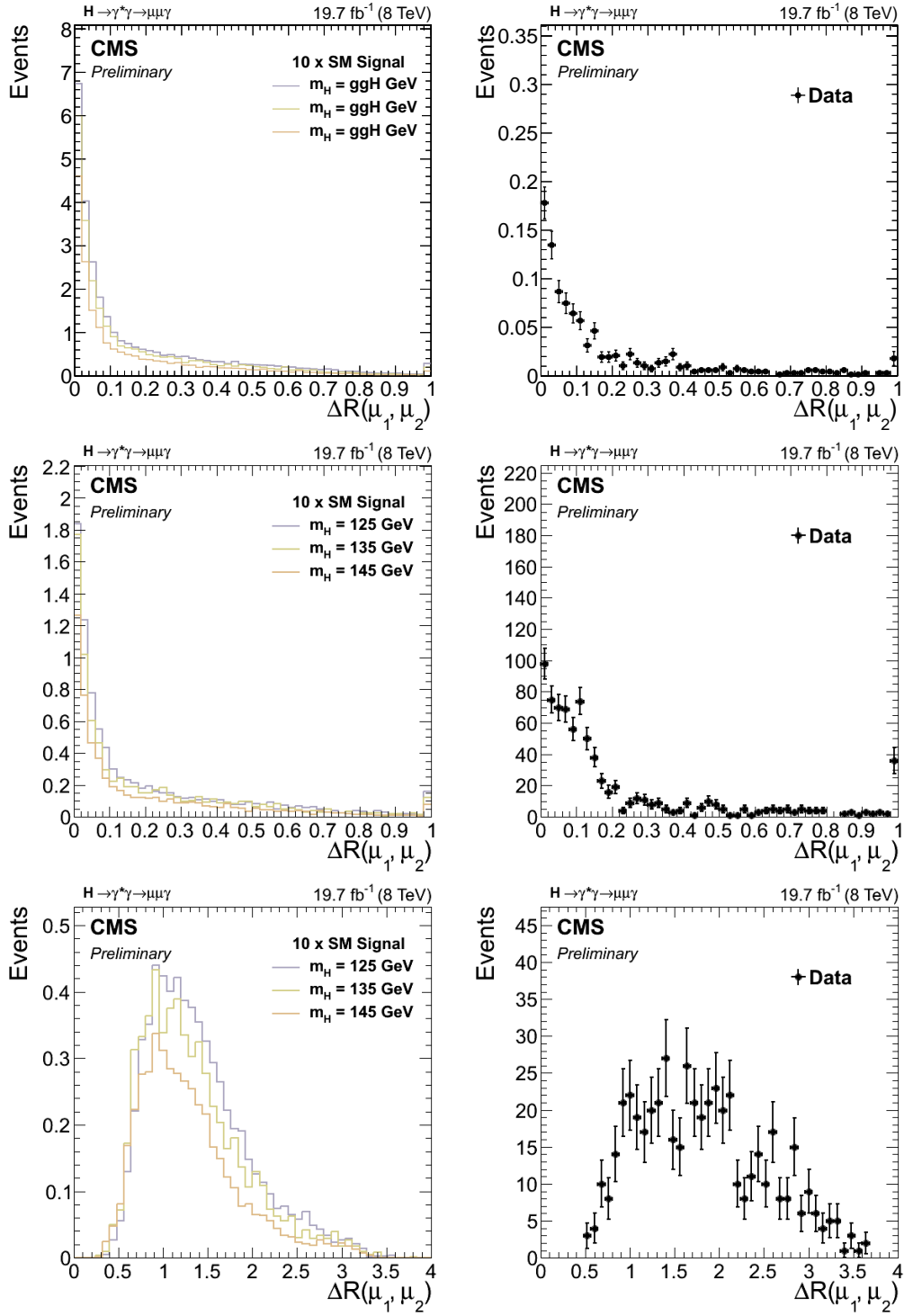


Figure D.2. Distributions of  $\Delta R(\mu_1, \mu_2)$  for ggF signal (left) and data (right) in 3 categories (top to bottom).

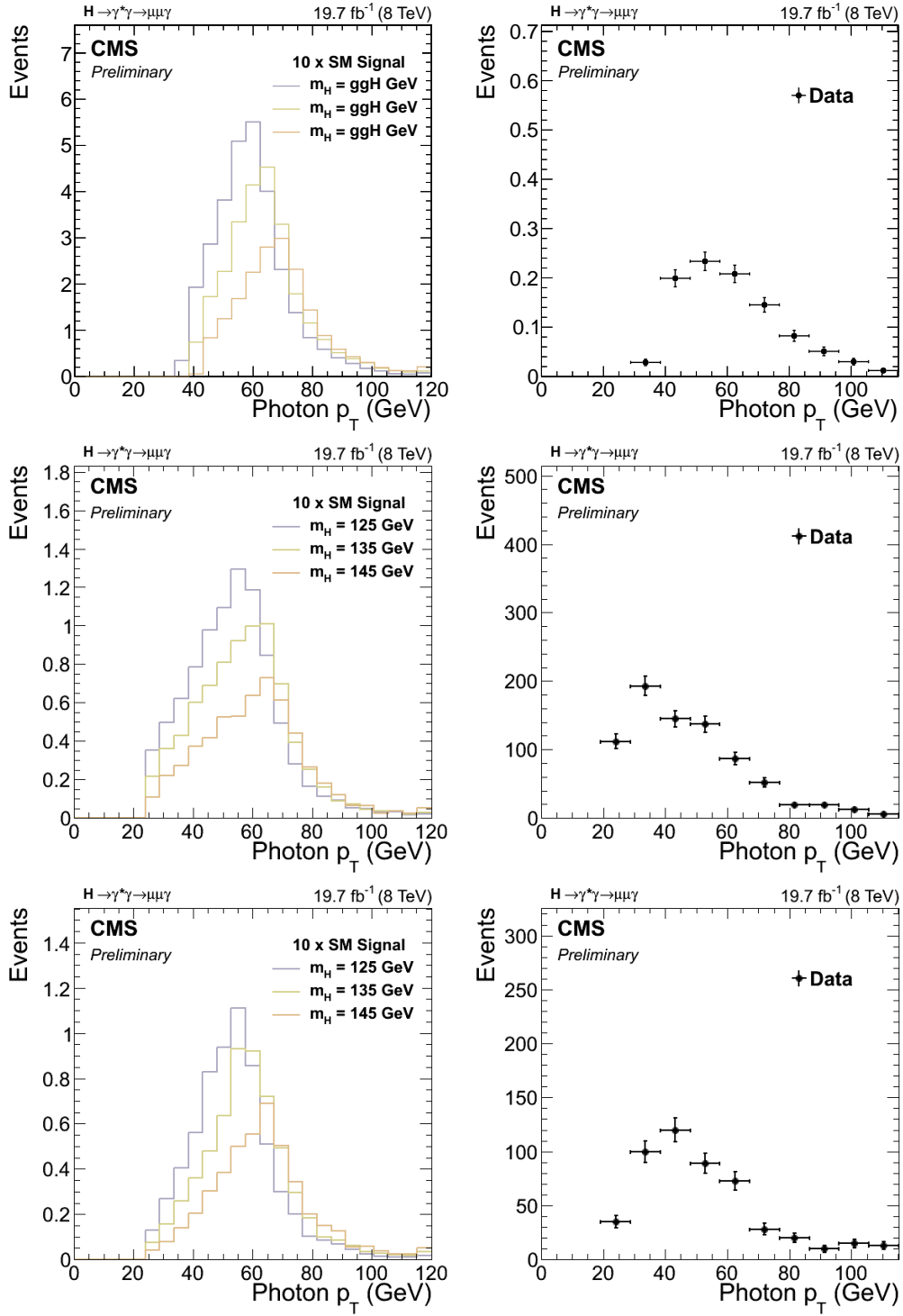


Figure D.3. Distributions of  $p_T^\gamma$  for ggF signal (left) and data (right) in 3 categories (top to bottom).

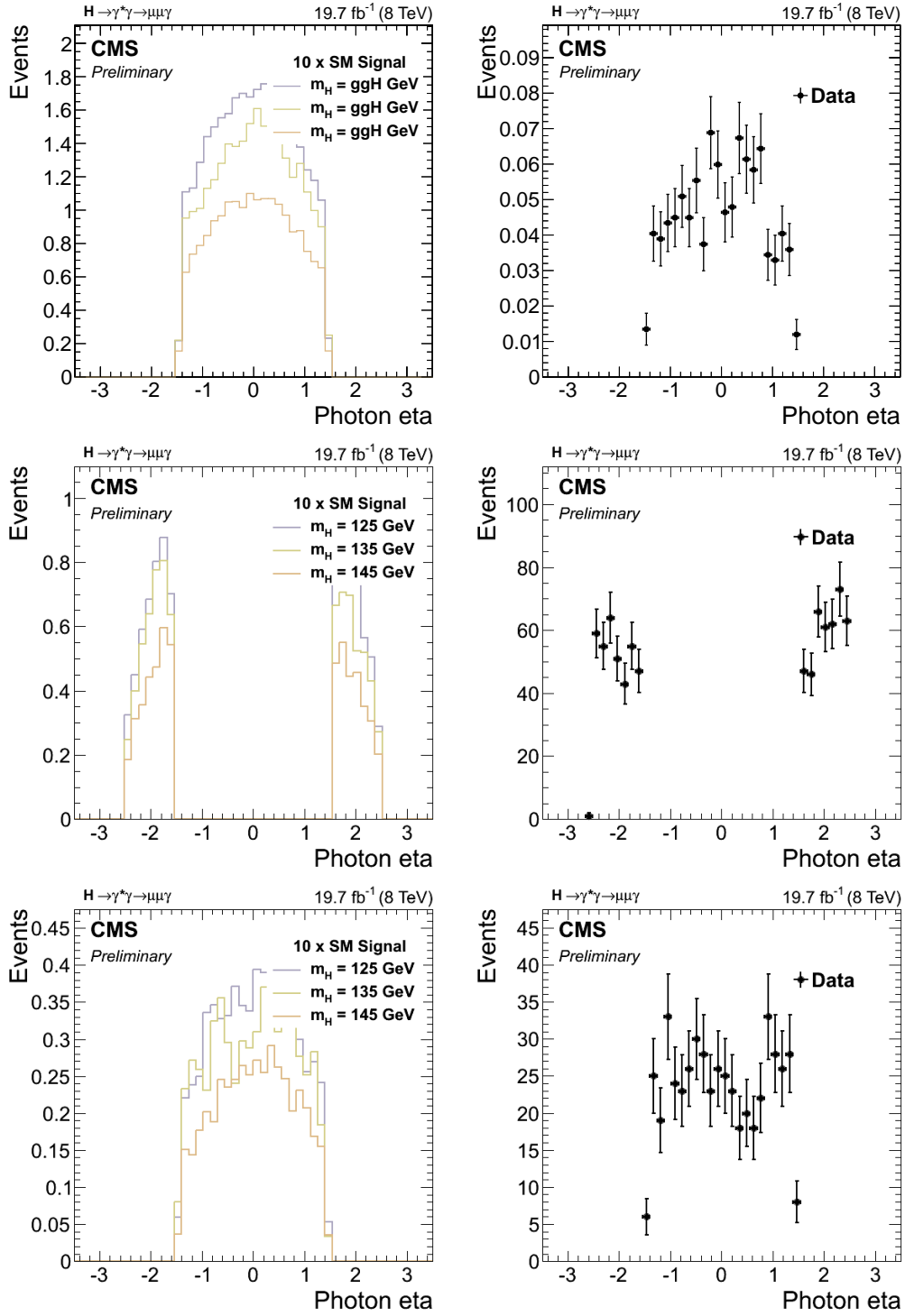


Figure D.4. Distributions of  $\eta^\gamma$  for ggF signal (left) and data (right) in 3 categories (top to bottom).

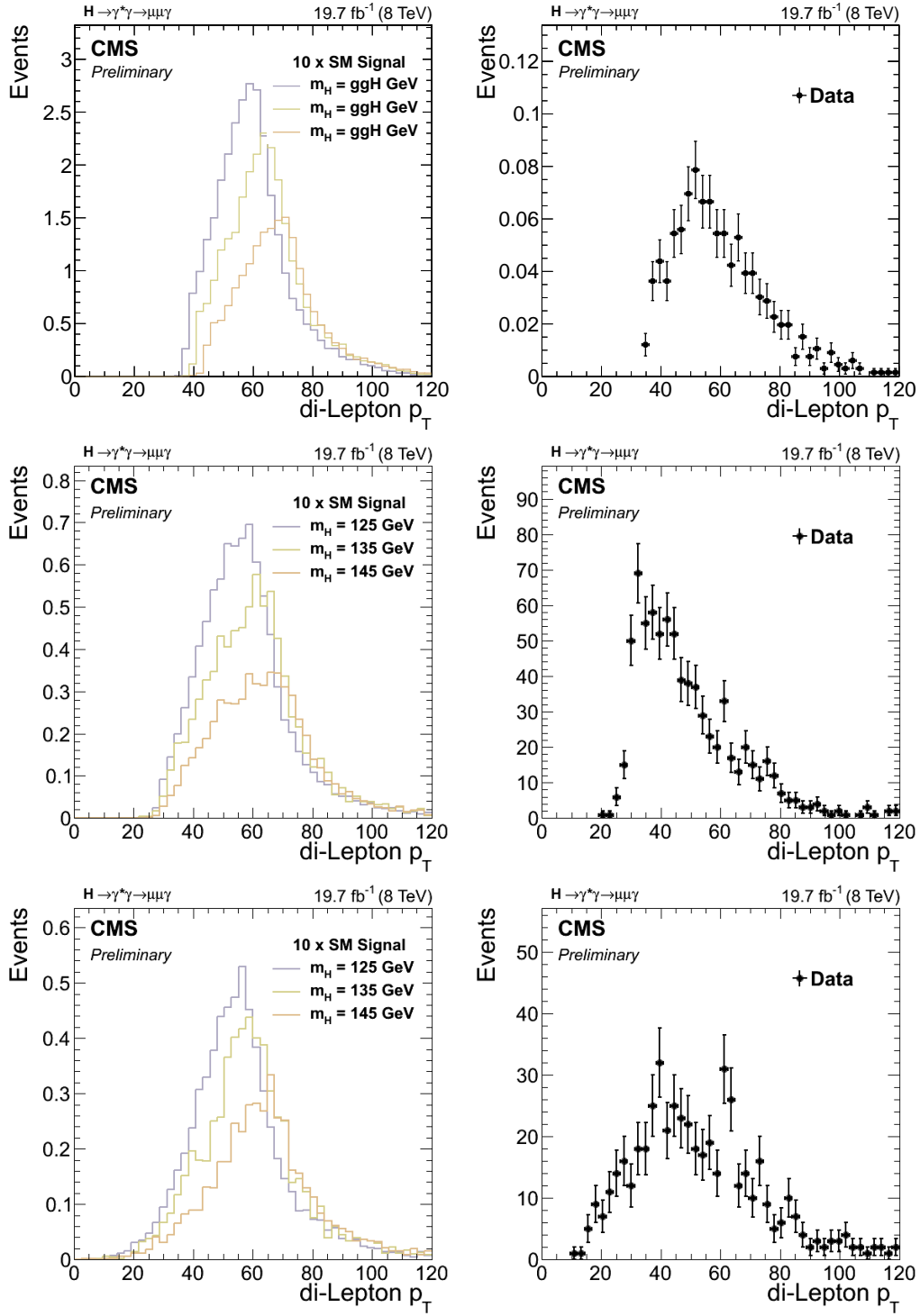


Figure D.5. Distributions of the dimuon transverse momentum,  $p_T^{\mu\mu}$ , in 3 categories (top to bottom).

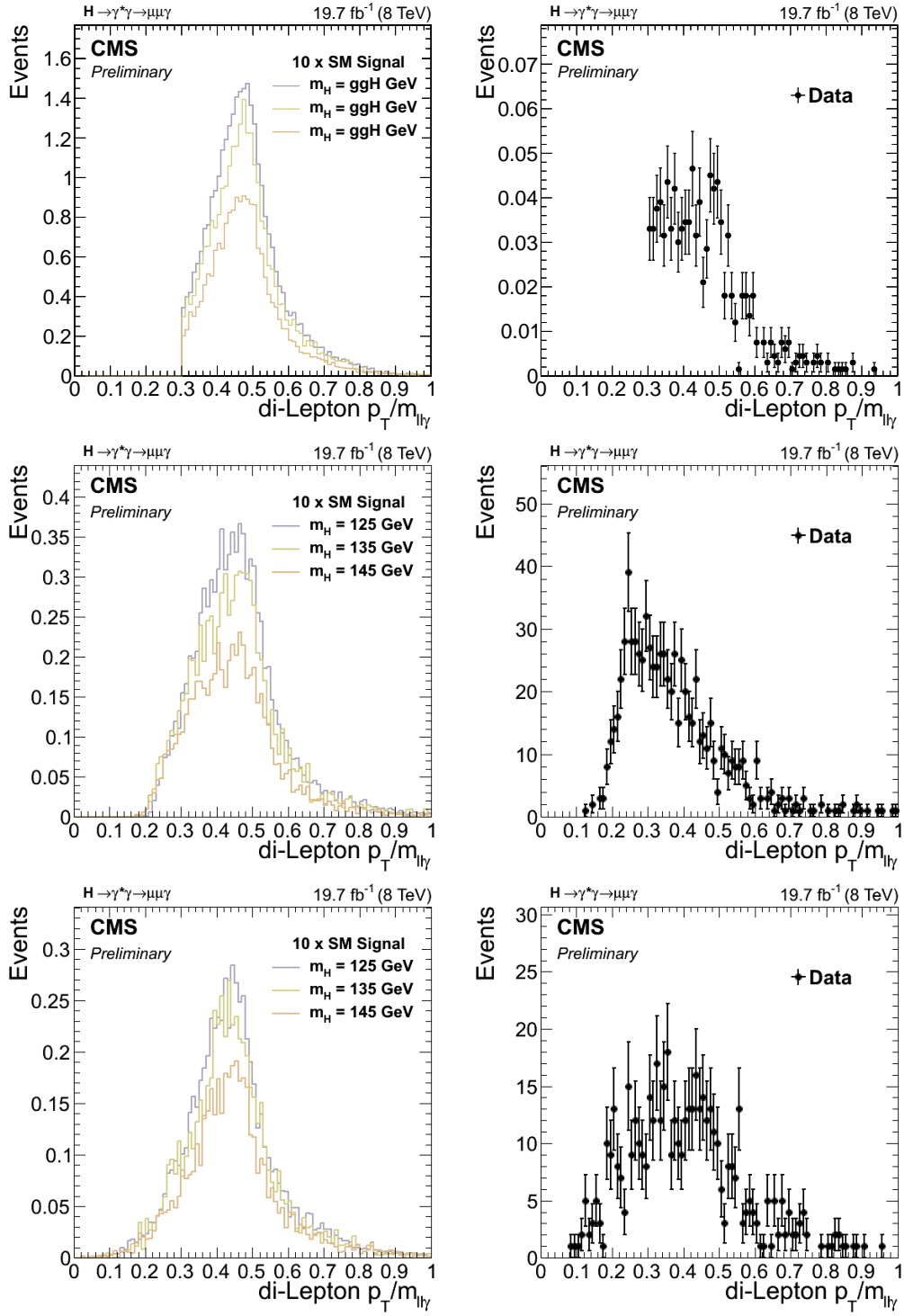


Figure D.6. Distributions of the  $p_T^{\mu\mu}/m_{\mu\mu\gamma}$ , in 3 categories (top to bottom).



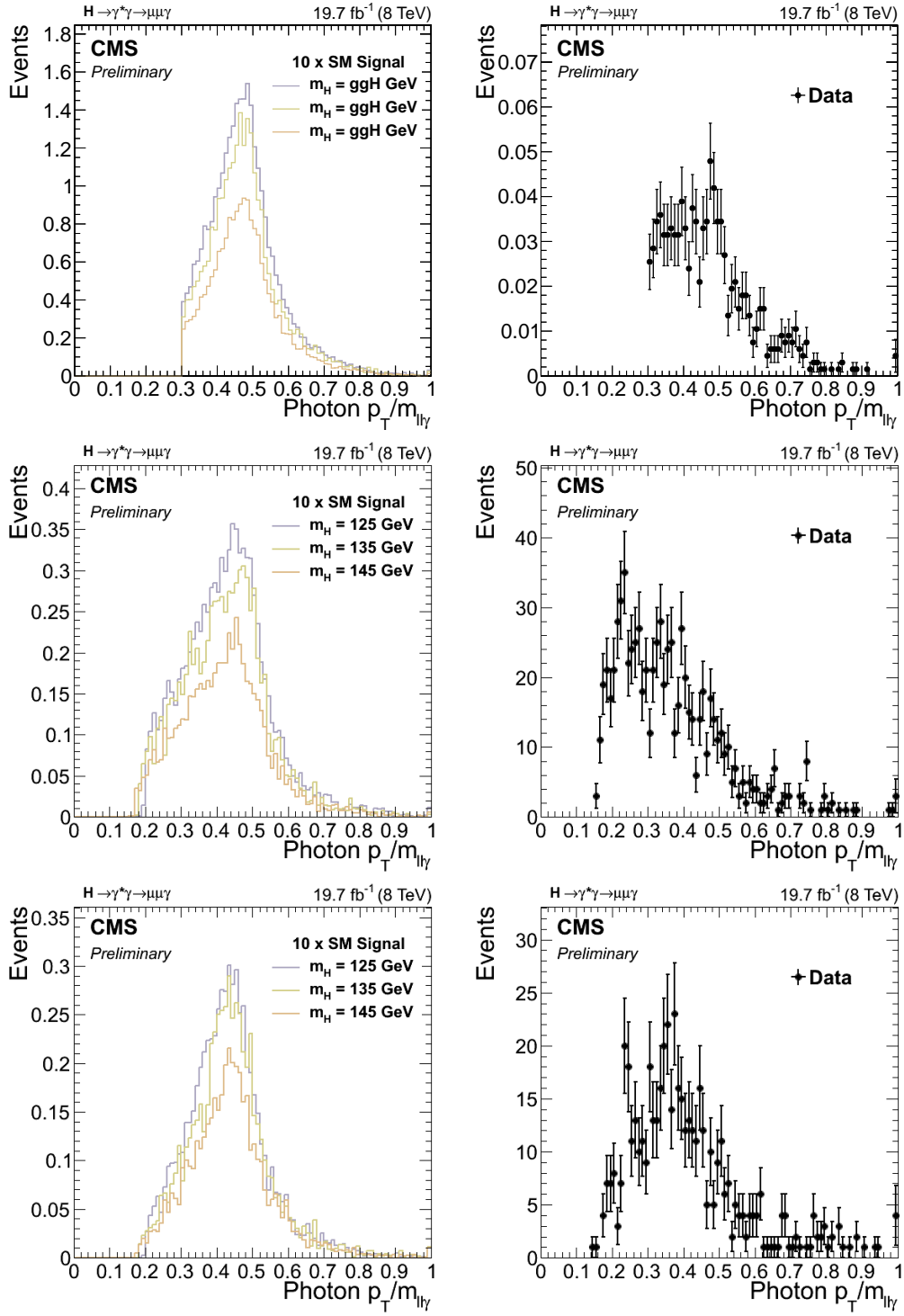


Figure D.7. Distributions of the  $p_T^\gamma / m_{\mu\mu\gamma}$ , in 3 categories (top to bottom).

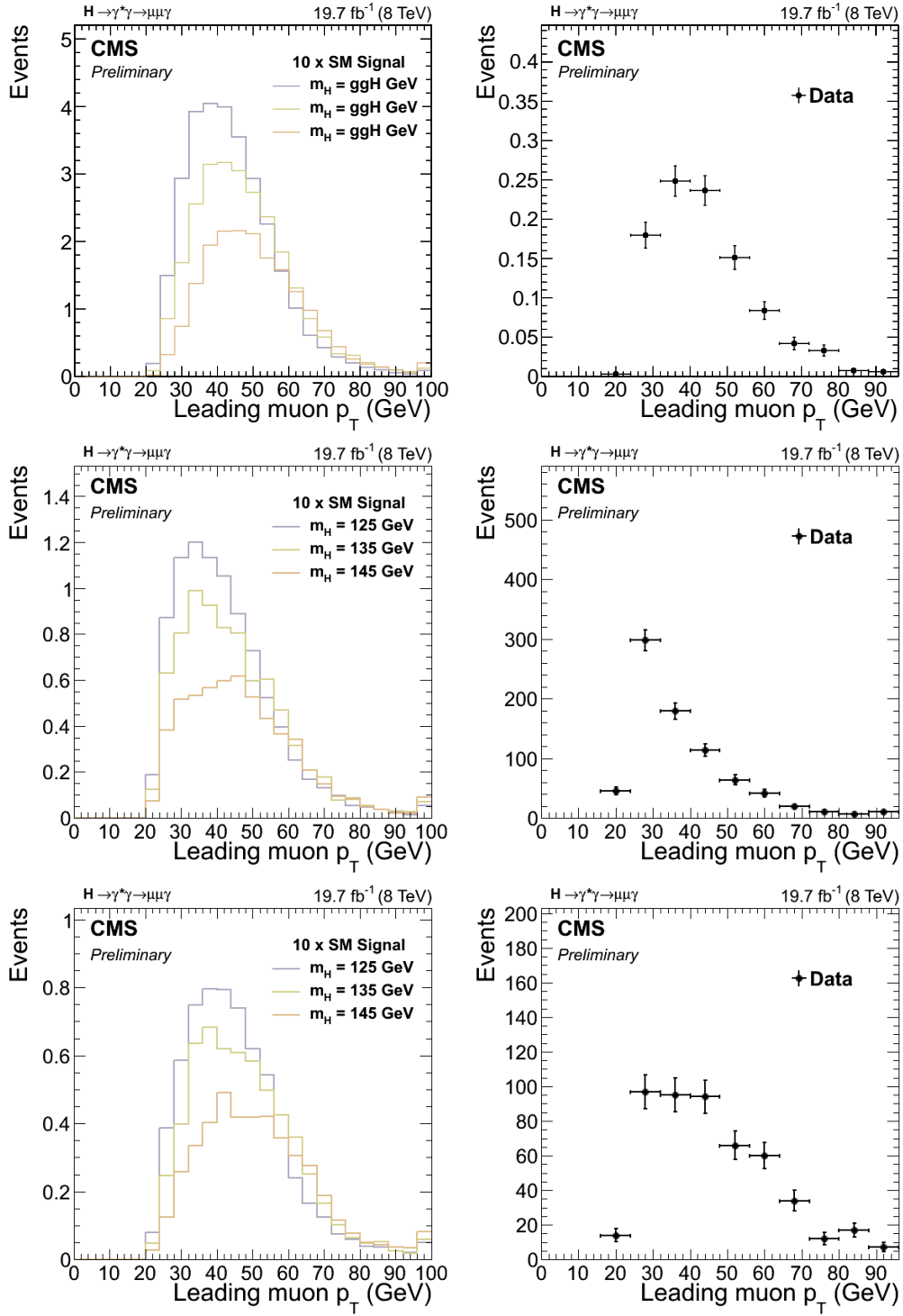


Figure D.8. Distributions of the leading muon  $p_T$ , in 3 categories (top to bottom).

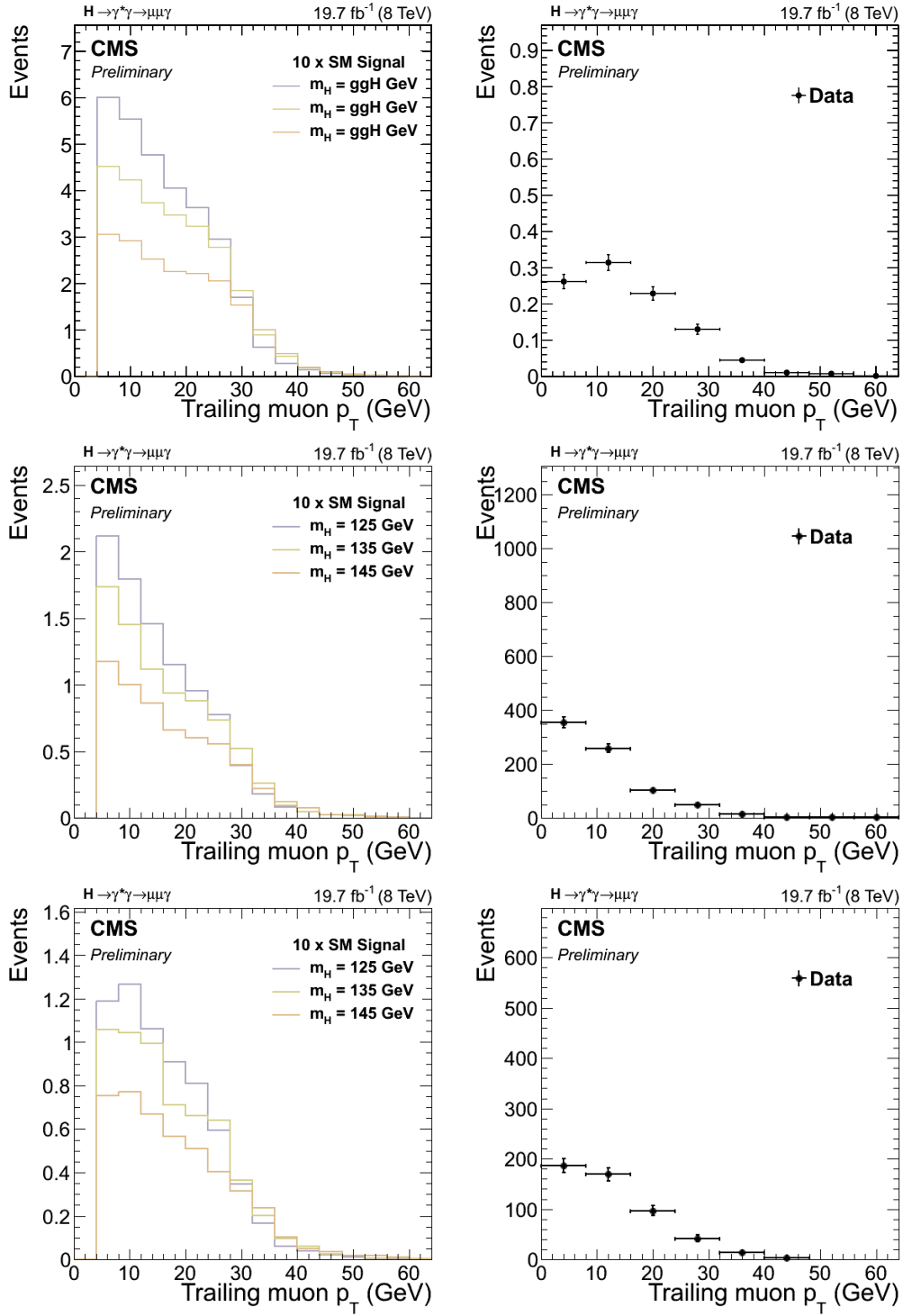


Figure D.9. Distributions of the sub-leading muon  $p_T$ , in 3 categories (top to bottom).

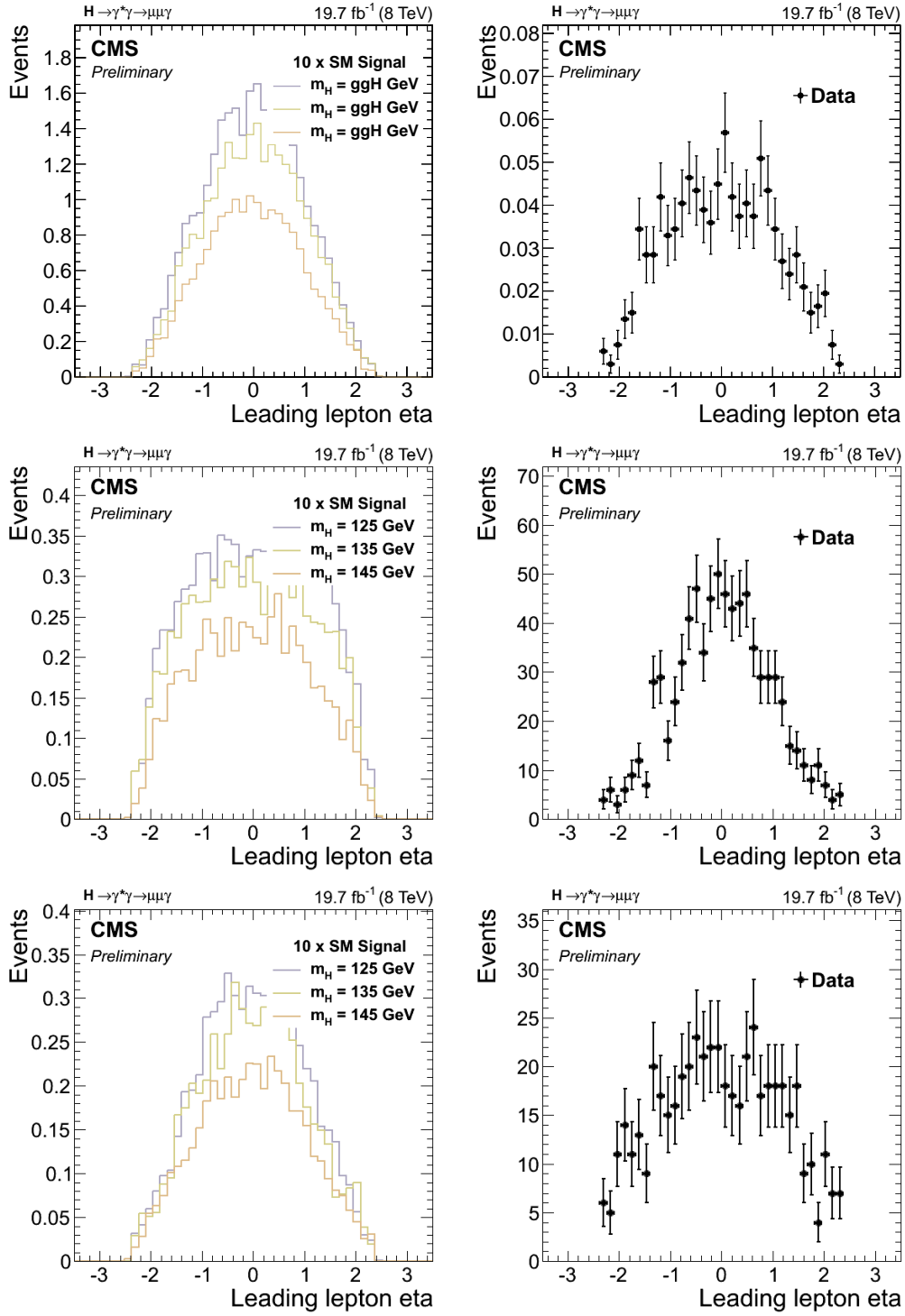


Figure D.10. Distributions of the leading muon  $\eta$ , in 3 categories (top to bottom).

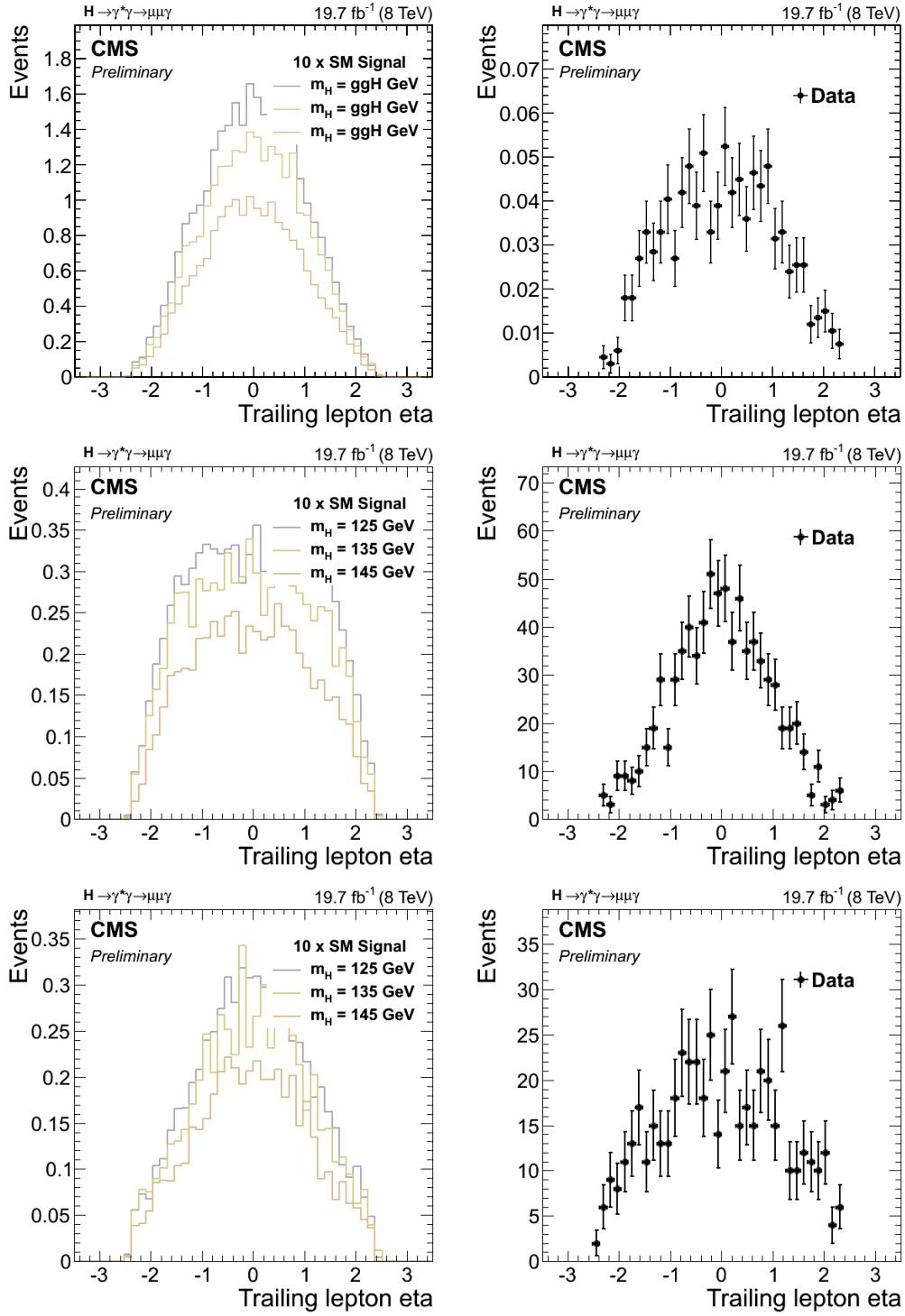


Figure D.11. Distributions of the sub-leading muon  $\eta$ , in 3 categories (top to bottom).

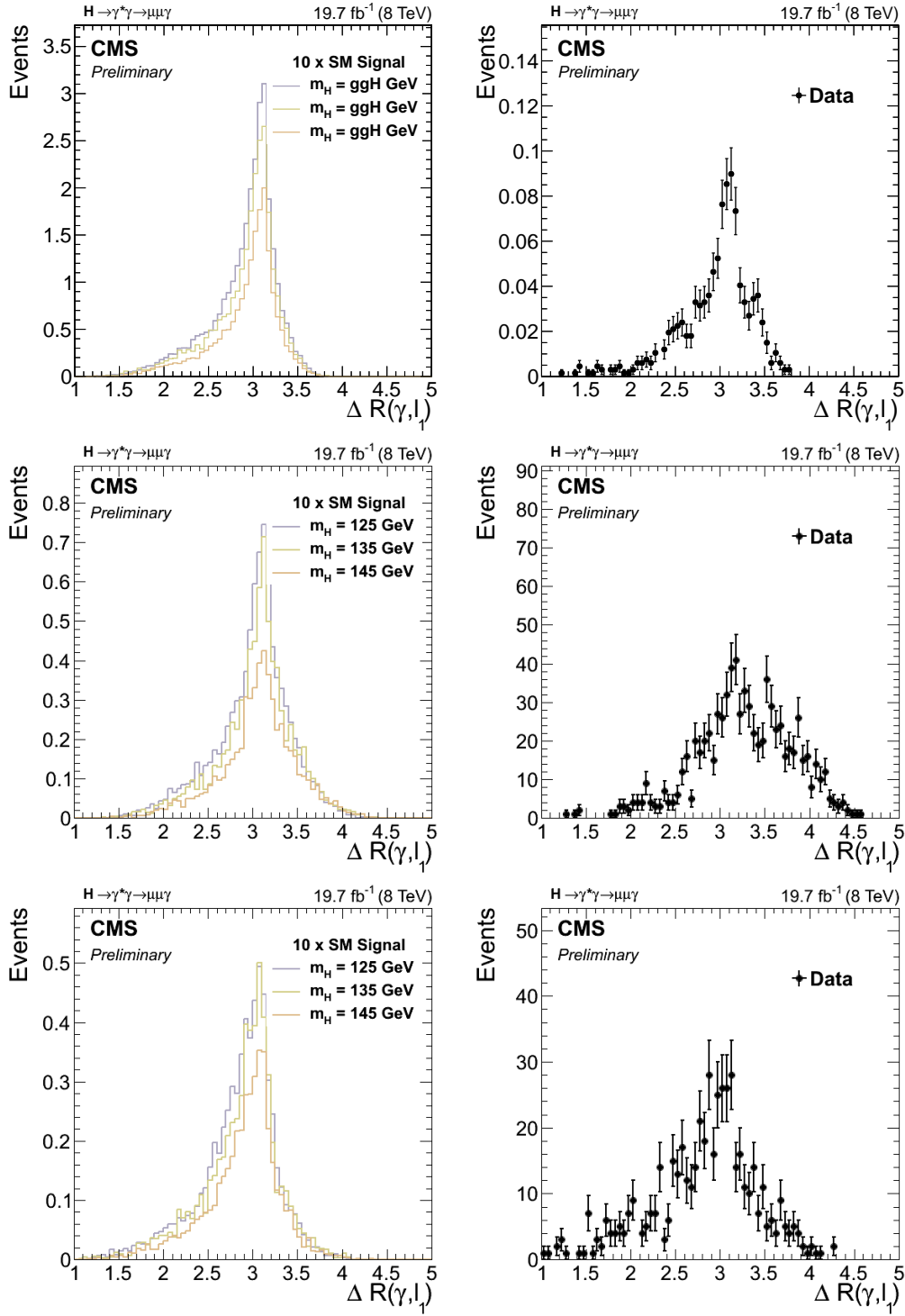


Figure D.12. Distributions of the  $\Delta R_{\eta\phi}$  between the leading muon and the photon.

### D.1.1. Resolution of $m_{\mu\mu}$ , $m_{\mu\mu\gamma}$ and angular variables

Resolution of the dimuon invariant mass, three-body mass and  $\Delta R(\mu\mu)$  are determined from the signal MC samples. Results using the samples from all of the Higgs boson masses are presented in Fig. D.13 for two event categories: *EB* and *EE*. The distributions are fitted with the Gaussian function, which width is taken as resolution (even though the fit itself may not be very good). One can see, for example, a degradation of the  $m_{\mu\mu\gamma}$  resolution in the Endcap region.

Figure D.14 shows the resolution of dilepton invariant mass in different bins of  $m_{\mu\mu}$ . This result is relevant for the limit on differential cross section presented in Section 4.

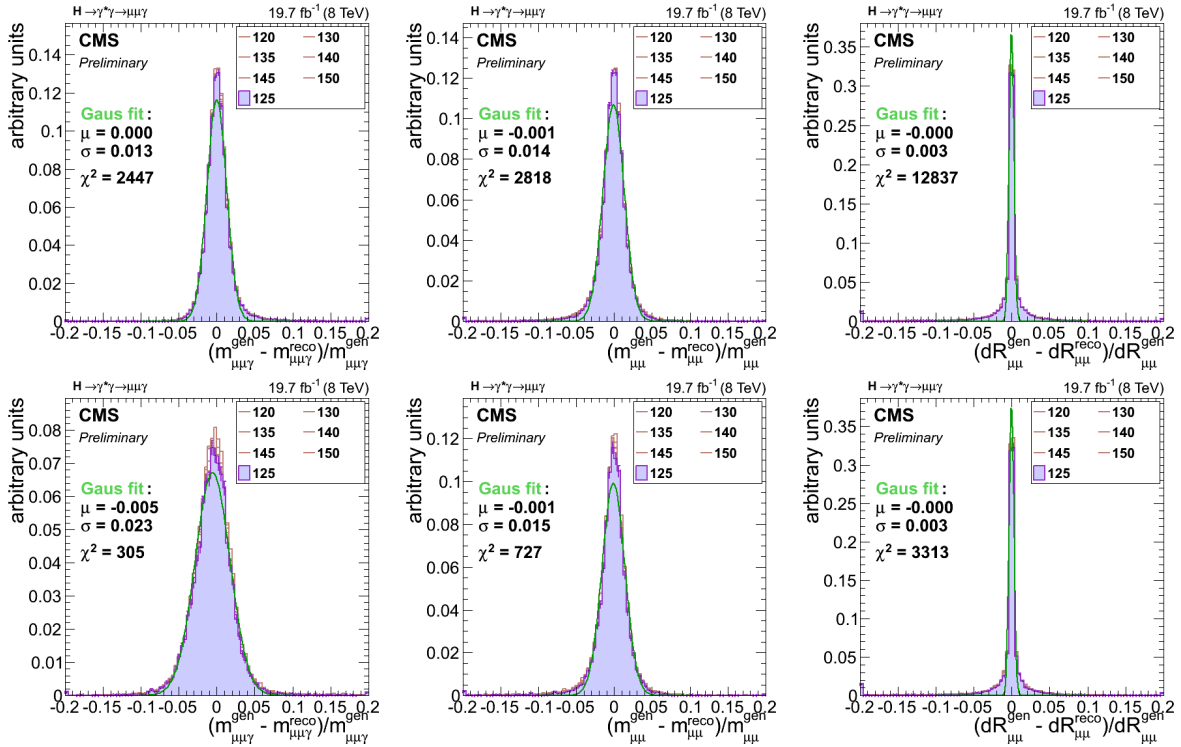


Figure D.13. Resolutions of  $m_{\mu\mu}$ ,  $m_{\mu\mu\gamma}$  and  $\Delta R(\mu\mu)$ . Top plots for EB category (photon in the Barrel), bottom plots for EE (photon in the Endcap).

One can see that there is a decrease of resolution in low di-lepton mass: 2.4% in the lowest bin,  $m_{\mu\mu}=[0.2,0.5]$  GeV and 1.2% in the highest,  $m_{\mu\mu}=[0.2,0.5]$  GeV bin.

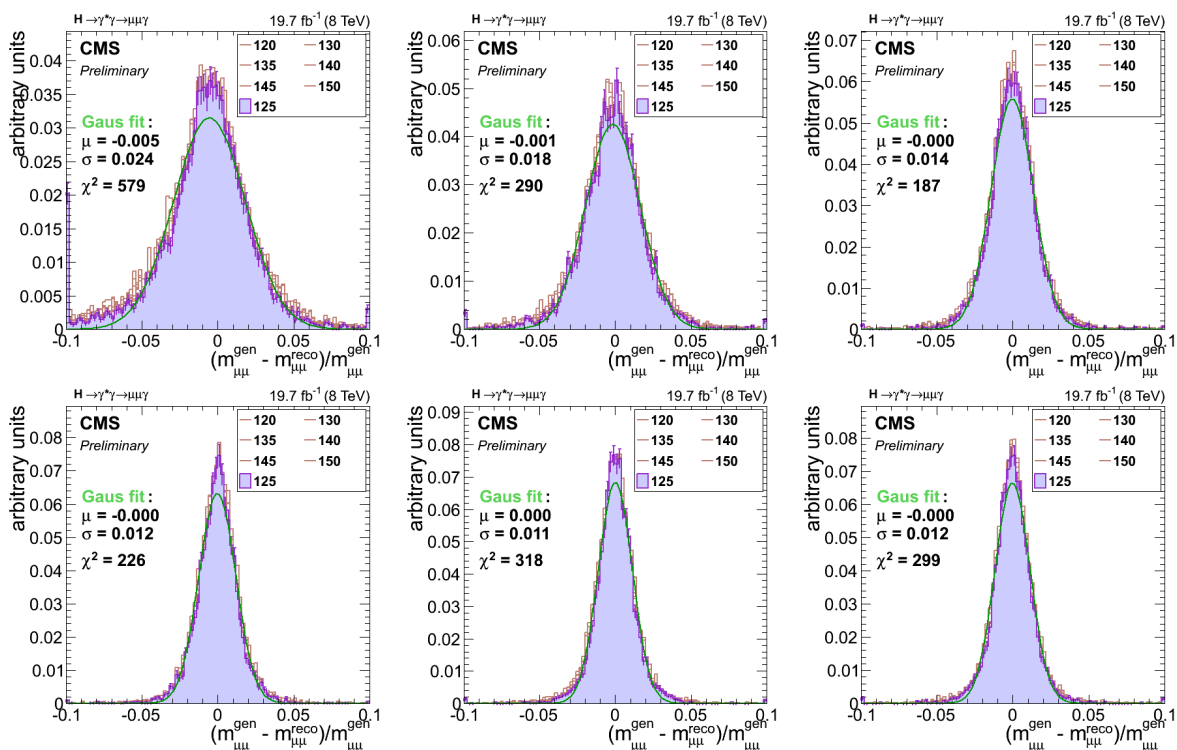


Figure D.14. Resolution of  $m_{\mu\mu}$ , in 6 bins of  $m_{\mu\mu}$ :  $0.2 - 0.5 - 1.0 - 2.0 - 4.0 - 9.0 - 20$  GeV (ordered from left-to-right, then top-to-bottom).



## D.2. Electron channel

Table D.2 shows the event yields after each selection in the electron channel.

Figures D.15–D.19 show various kinematic distributions, plotted after the selection denoted by the star (\*) in Table D.2.

It is also useful to look at the input variables to the MVA ID used for the merged electron object, after the selection. Those are shown in Figures D.20, D.21 and D.22. The distributions from the signal MC of  $m_H = 125 \text{ GeV}$  are normalized to the data and shown as green histograms.

Table D.2. Event yield after each selection criteria for data and signal with  $m_H = 125 \text{ GeV}$  for  $L = 19.7 \text{ fb}^{-1}$  in the electron channel.

Selection	Data	Sig: total	ggH	vbfH
Pass Trigger	87M	23.25	21.46	1.78
DALelectron selection (MVA ID cut at 0.12)	58K	3.76	3.48	0.27
$p_T^{e1} + p_T^{e2} > 44 \text{ GeV}$ , $m_{ee} < 1.5 \text{ GeV}$	26K	3.12	2.89	0.22
Photon $p_T > 30 \text{ GeV}$ ; $ \eta_{SC}  < 1.4442$	1566	2.06	1.91	0.14
$110 < m_{e'\gamma} < 170 \text{ GeV}$	436	2.05	1.91	0.14
* $p_T^{e'}/m_{e'\gamma} > 0.3$ and $p_T^{\gamma}/m_{e'\gamma} > 0.3$	337	1.95	1.82	0.13

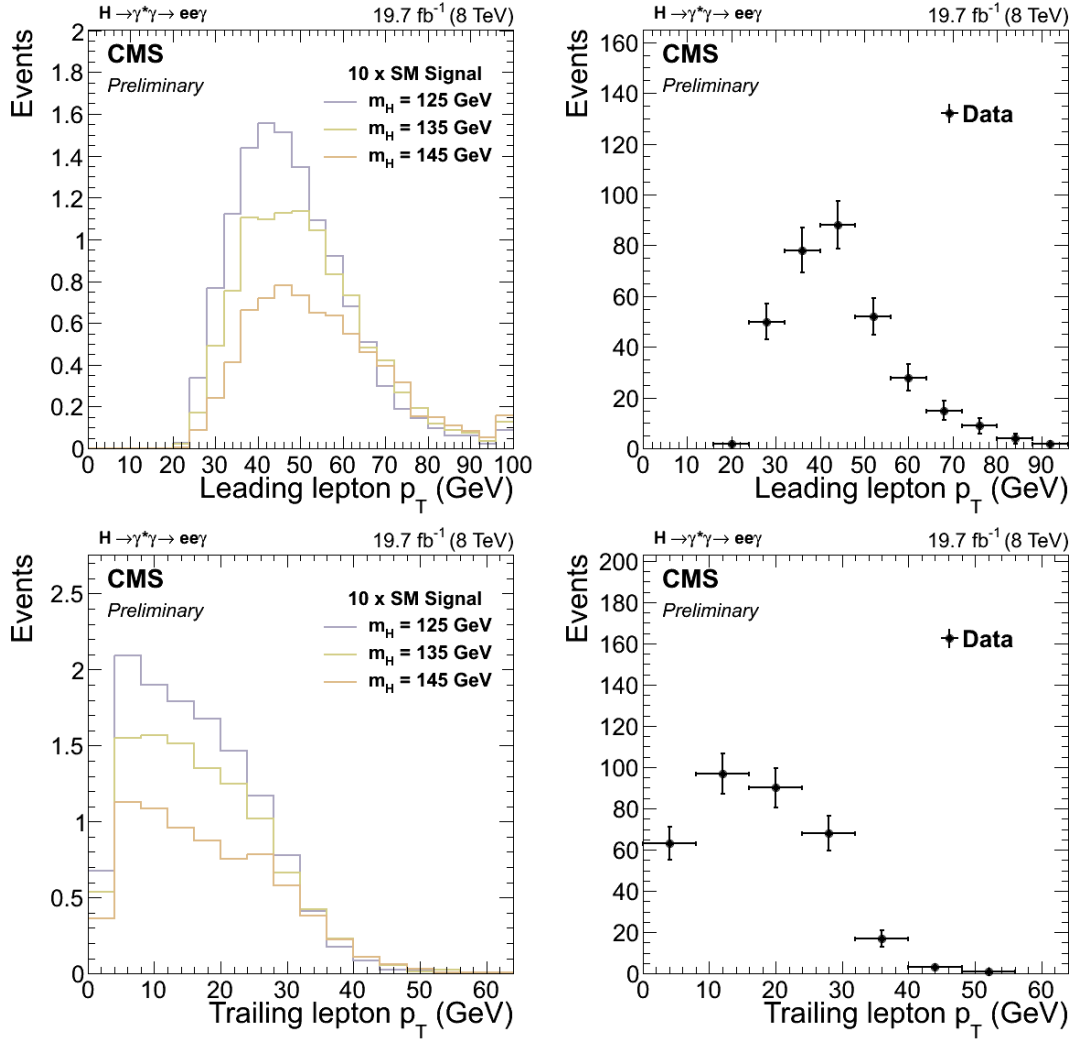


Figure D.15. Transverse momenta of the leading and trailing GSF tracks inside the Dalitz electron object (see text of Sec.3.4.6).

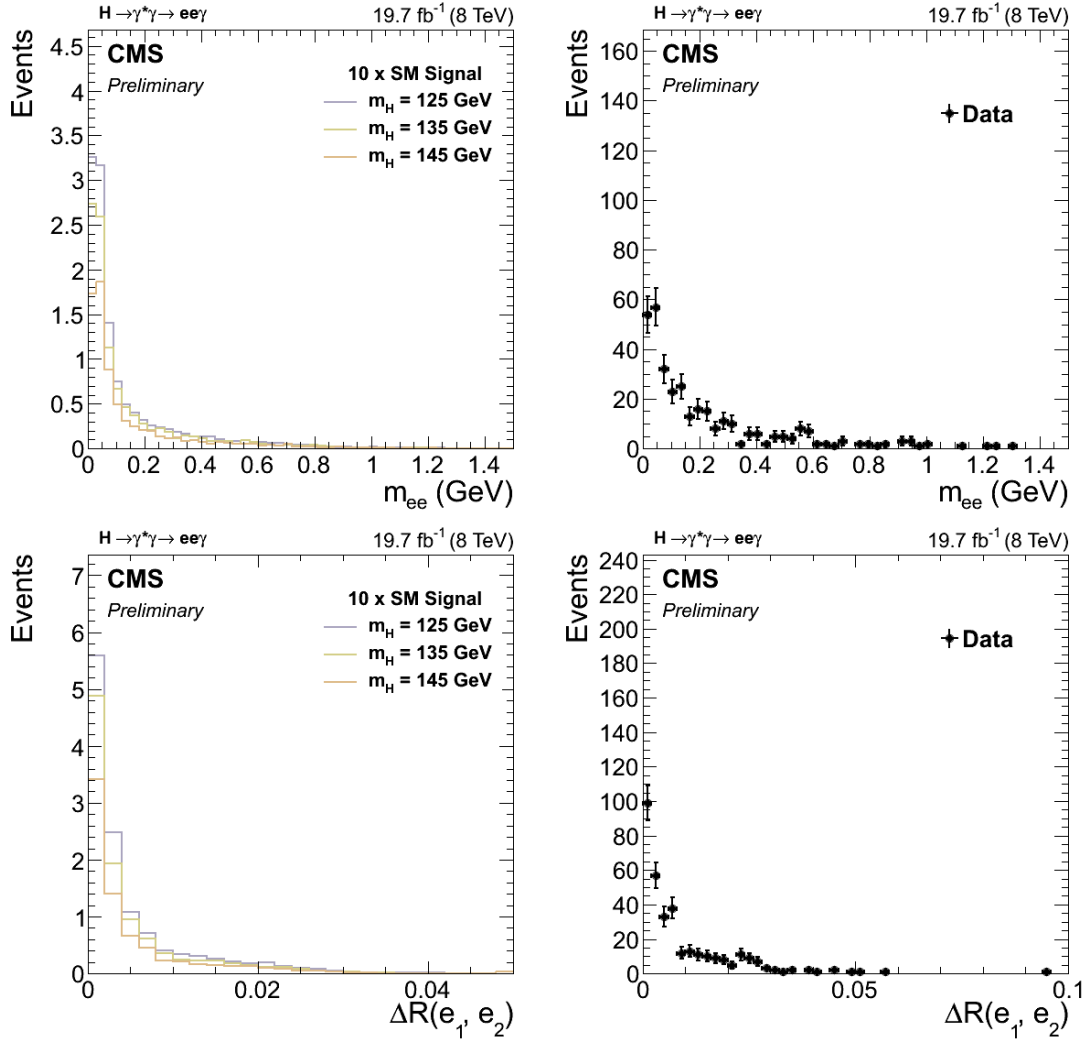
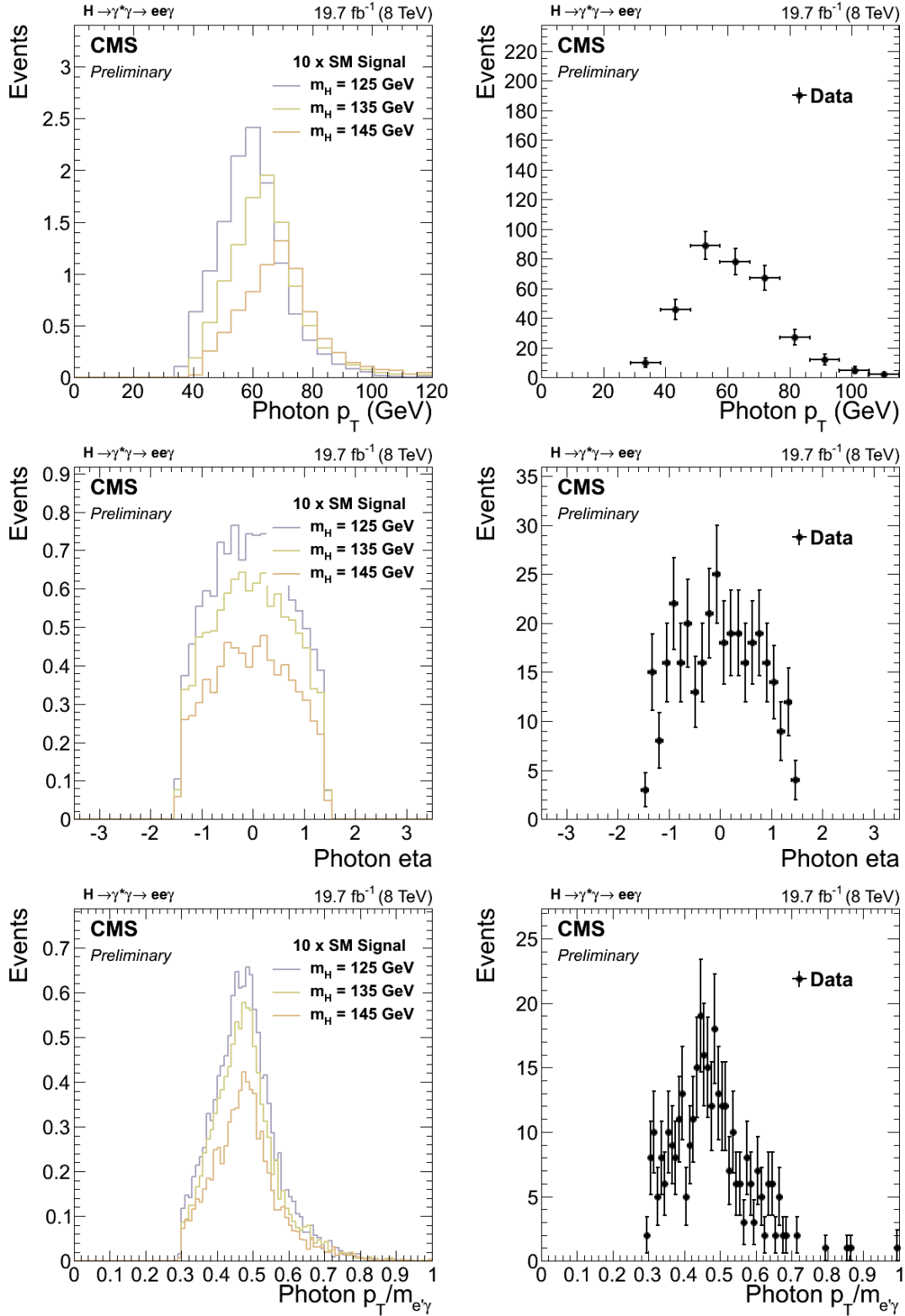
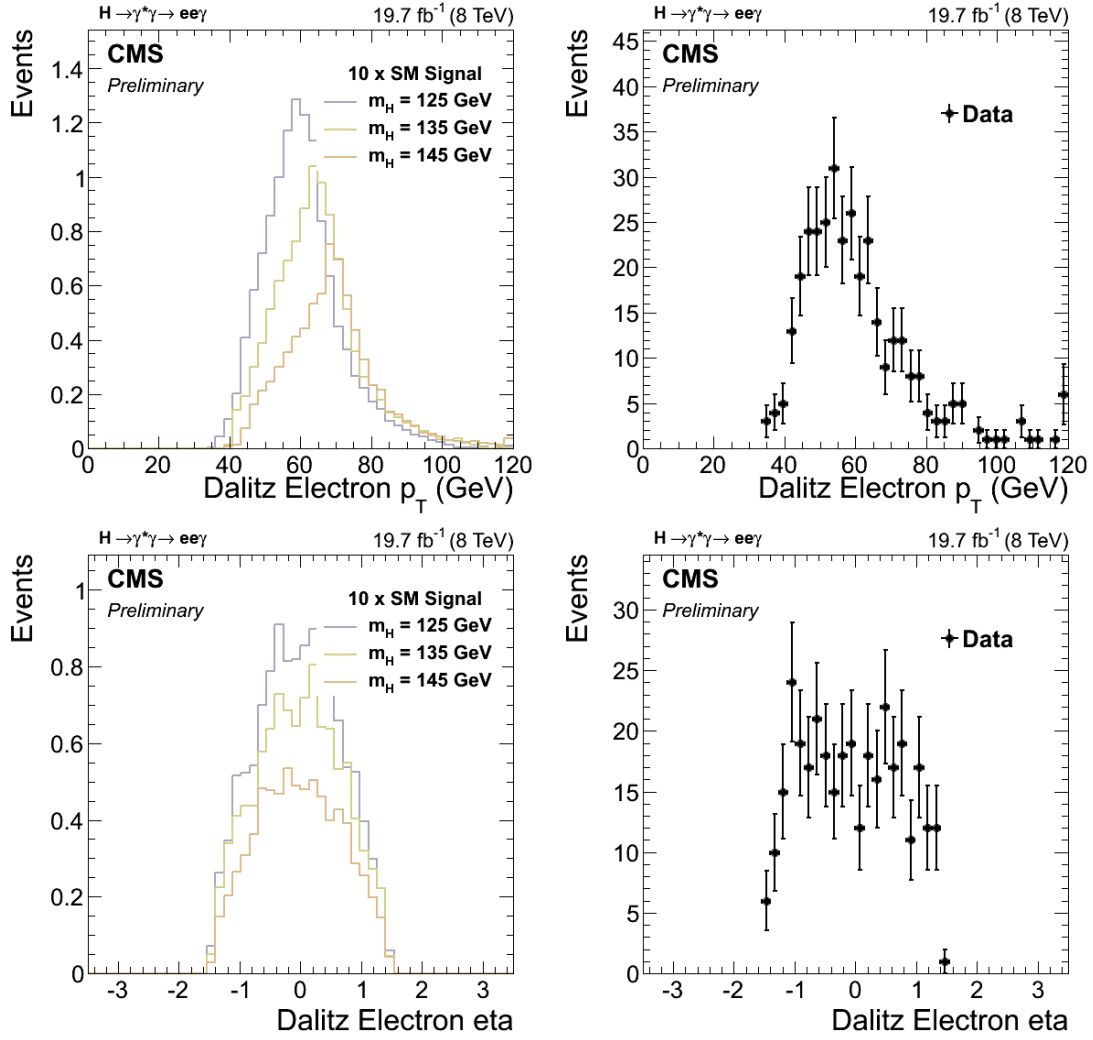


Figure D.16. Invariant mass and  $\Delta R_{\eta\phi}$  of the two GSF tracks.

Figure D.17. Photon distributions:  $p_T, \eta, p_T/m_{e'\gamma}$ .

Figure D.18. Dalitz electron object distributions:  $p_T, \eta$ .

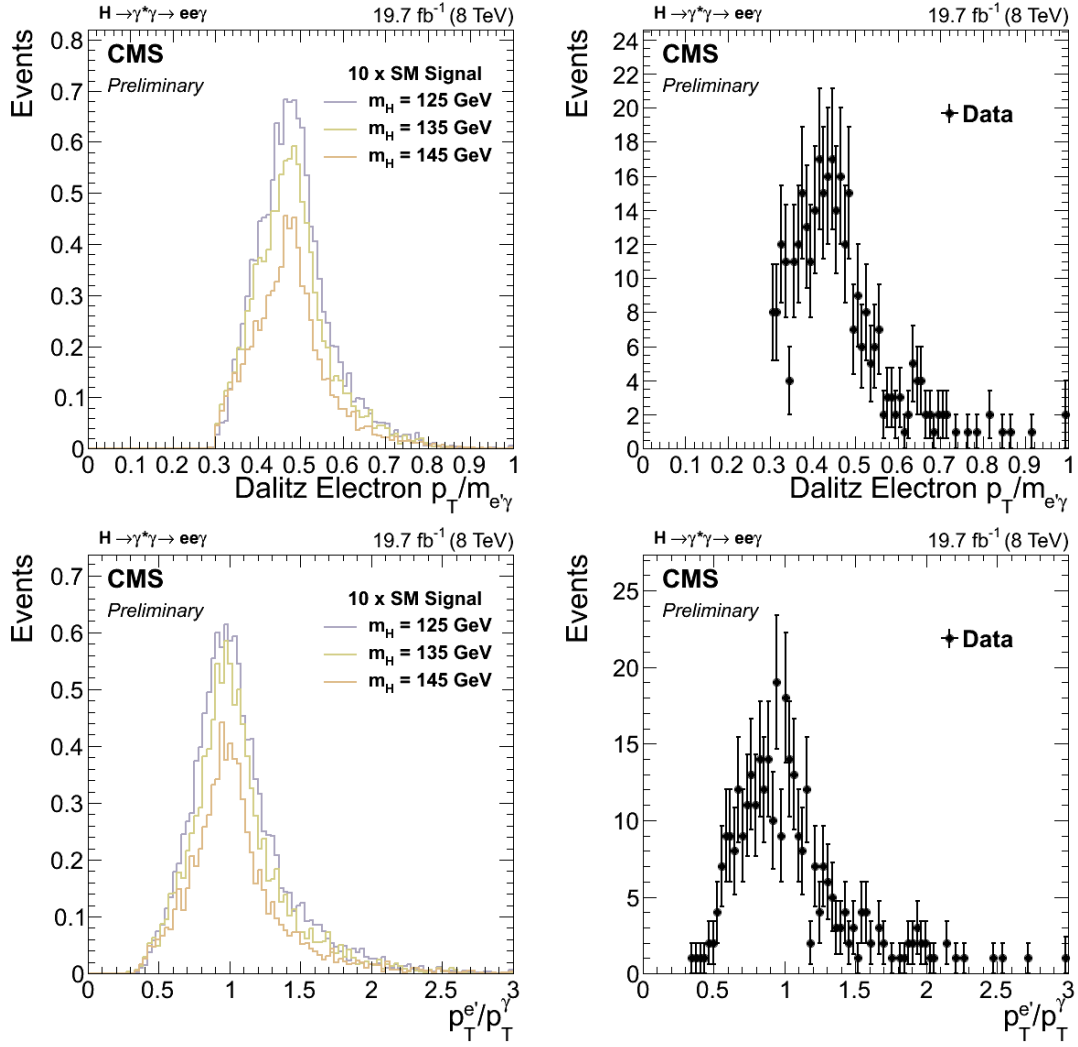


Figure D.19. Dalitz electron object distributions:  $p_T/m_{e'\gamma}, p_T^{e'}/p_T^\gamma$ .

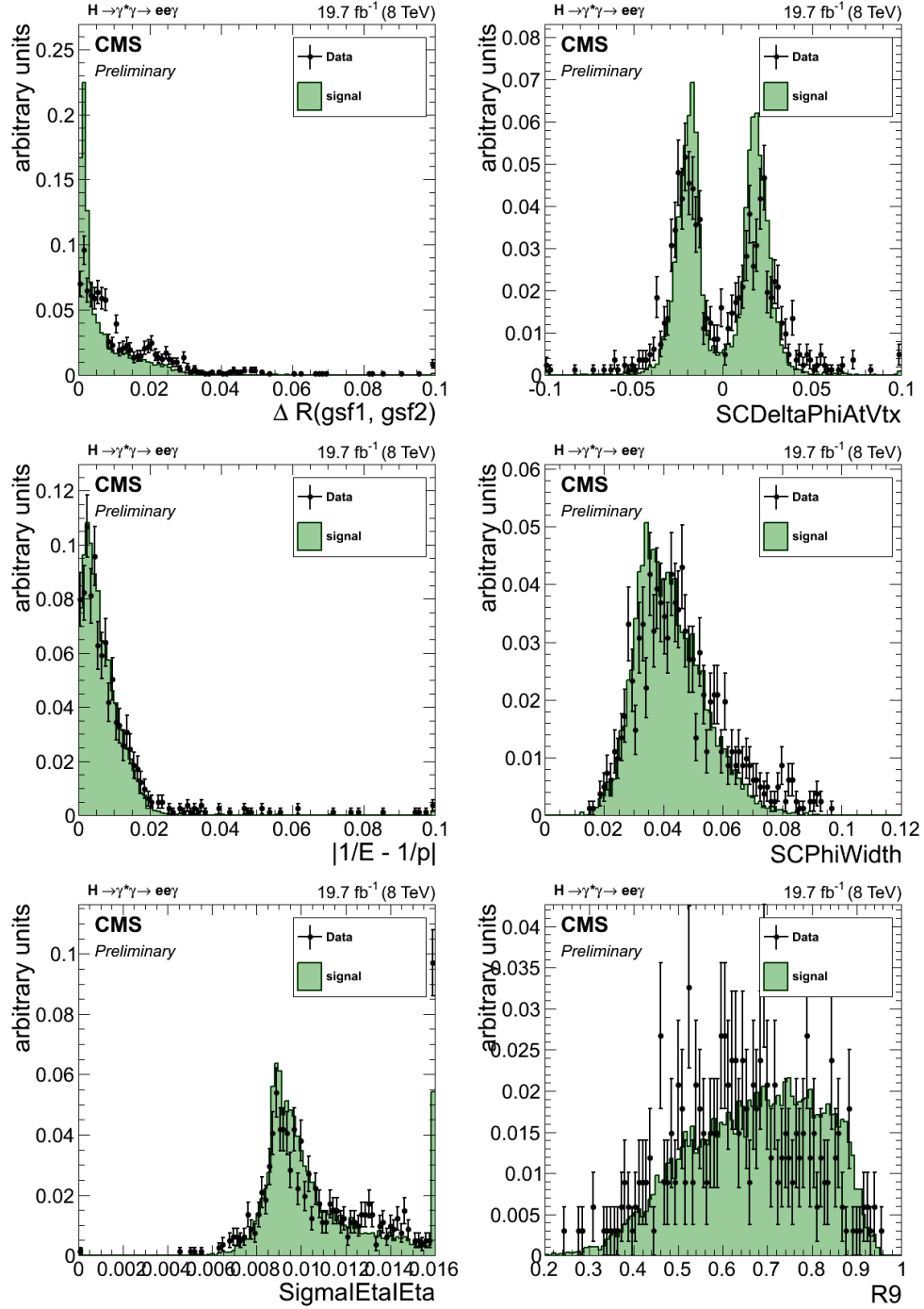


Figure D.20. MVA ID input variables I.  $\Delta R$  between two GSF tracks and  $\Delta\phi_{in}$  (top);  $|1/E - 1/p|$  and SC  $\phi$ -width (middle);  $\sigma_{in\eta}$  of the second most energetic basic cluster and  $R_9$  (bottom).

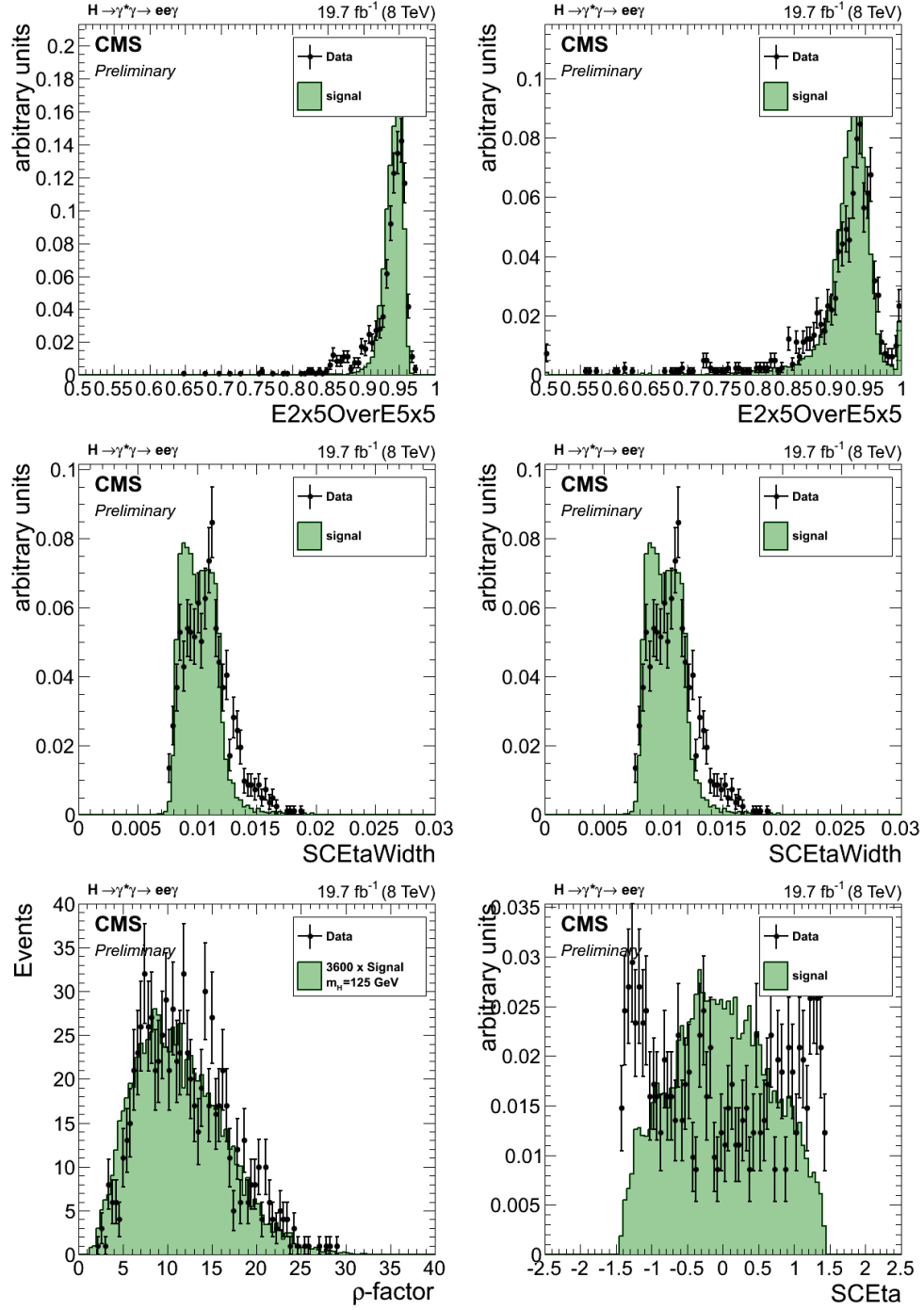


Figure D.21. MVA ID input variables II.  $E_{2 \times 5} / E_{5 \times 5}$  of the most energetic basic cluster and  $E_{2 \times 5} / E_{5 \times 5}$  of the second most energetic basic cluster (top);  $H/E$  and SC  $\eta$ -width (middle);  $\rho$  and  $\eta^{SC}$  (bottom).



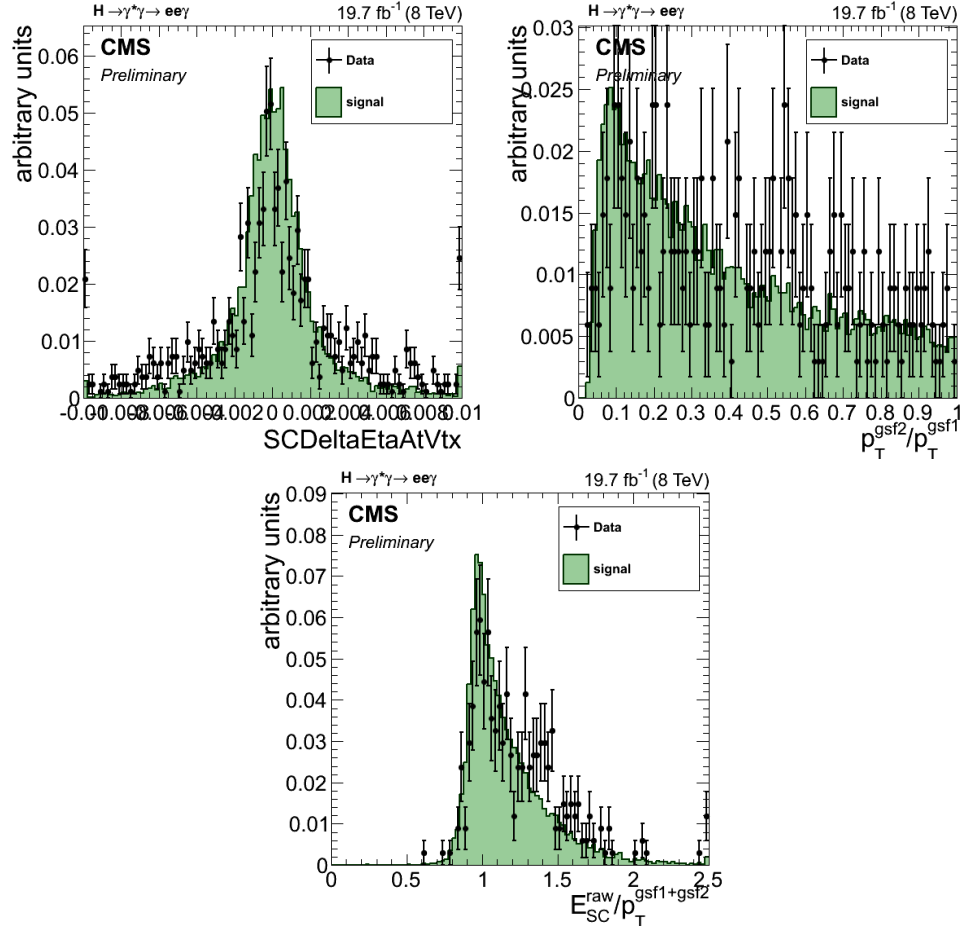


Figure D.22. MVA input variables III.  $\Delta\eta_{in}$  and the ratio of  $p_T$  between second highest  $p_T$  GSF track to highest  $p_T$  GSF track raw  $E^{SC}$  over  $p_T$  of two GSF tracks (middle).

### D.3. $H \rightarrow (J/\psi)\gamma$

Table D.3 shows the yields obtained in the  $H \rightarrow (J/\psi)\gamma \rightarrow \mu\mu\gamma$  search. The signals both from  $J/\psi$  and Dalitz decay channels are shown. Figures D.23 and D.24 show the distributions of the relevant kinematic observables after the full event selection (denoted by a (\*) in Table D.3).

Table D.3. Event yield after each selection criteria for data and  $H \rightarrow (J/\psi)\gamma \rightarrow \mu\mu\gamma$  signal with  $m_H = 125 \text{ GeV}$  for  $L = 19.7 \text{ fb}^{-1}$ .

Selection requirement	Observed events in data	Expected signal events	
		from $H \rightarrow J/\psi\gamma$	from $H \rightarrow \gamma^*\gamma$
HLT; Photon: $p_T^\gamma > 25 \text{ GeV}$ , $ \eta^\gamma  < 1.444$	0.6M	0.023	5.31
Muon selection: $p_T^{\mu 1} > 23 \text{ GeV}$ and $p_T^{\mu 2} > 4 \text{ GeV}$	57K	0.018	4.01
$m_{\mu\mu} < 20 \text{ GeV}$ , $\Delta R(\gamma, \mu) > 1$	5714	0.018	3.37
Loose $J/\psi$ selection: $2.5 < m_{\mu\mu} < 3.7 \text{ GeV}$	820	0.017	0.27
$p_T^\gamma > 40 \text{ GeV}$ and $p_T^{\mu\mu} > 40 \text{ GeV}$	221	0.015	0.23
* Tight $J/\psi$ selection: $2.9 < m_{\mu\mu} < 3.3 \text{ GeV}$	129	0.015	0.08
Fit region: $110 < m_{\mu\mu\gamma} < 150 \text{ GeV}$	48	0.015	0.08
Higgs mass: $122 < m_{\mu\mu\gamma} < 128 \text{ GeV}$	7	0.013	0.07

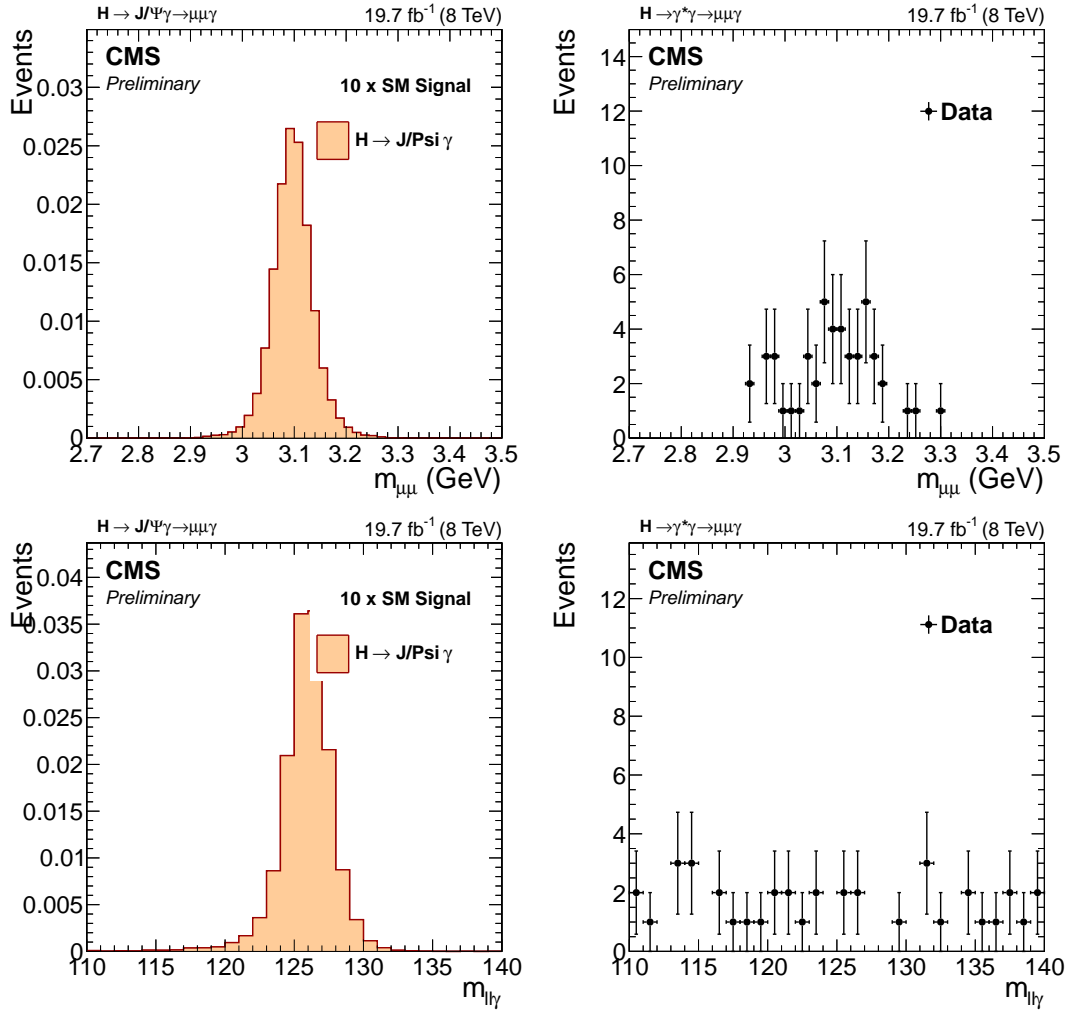


Figure D.23.  $J/\psi \rightarrow \mu\mu$  peak and the three-body mass. The signal distributions (left) are normalized to the total number of events in data (right).

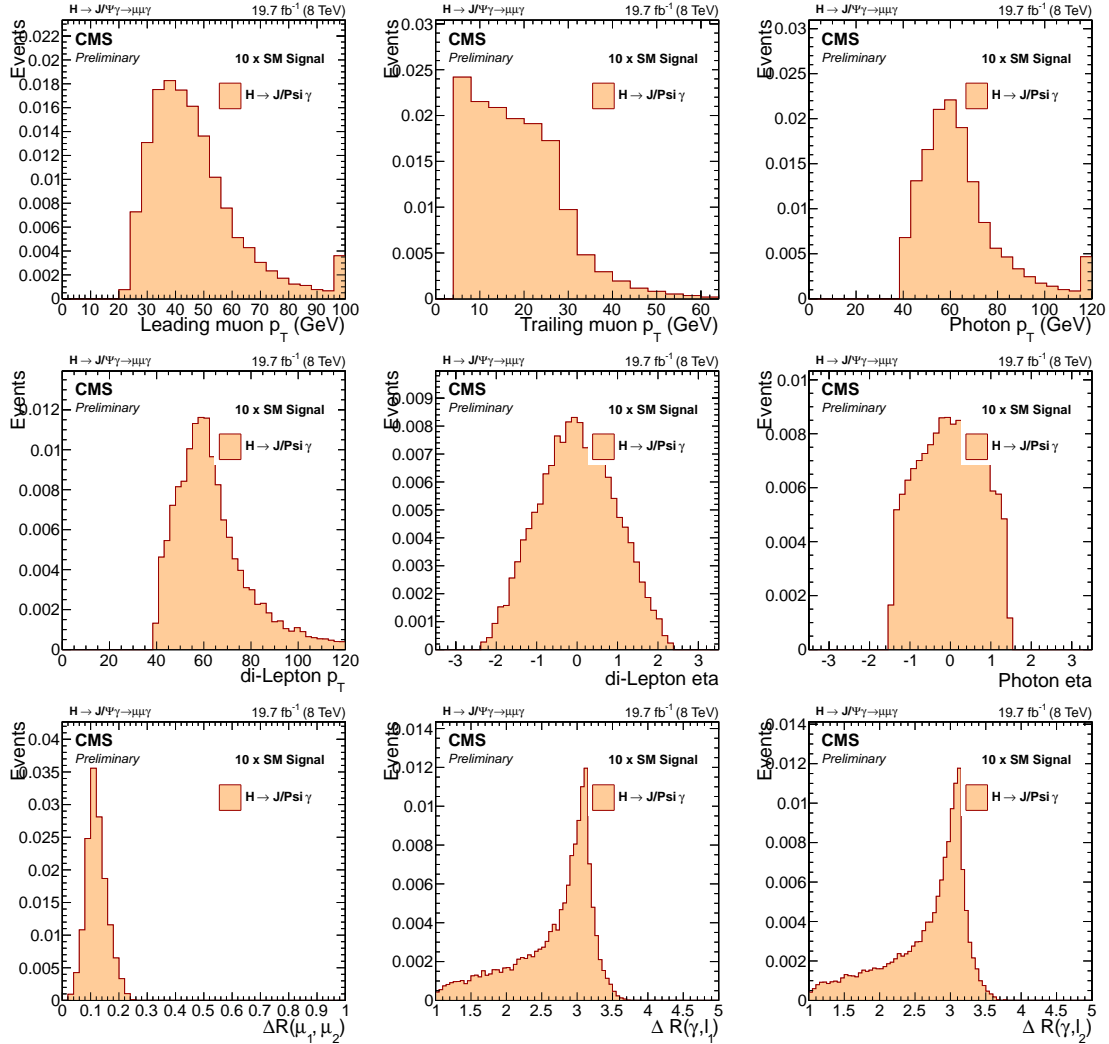


Figure D.24. Distributions of the key variables from the  $H \rightarrow (J/\psi)\gamma$  signal process. Transverse momenta of the muons, the dimuon system and the photon; pseudorapidity of the photon and the dimuon system; distances  $\Delta R_{\eta\phi}$  between the objects.

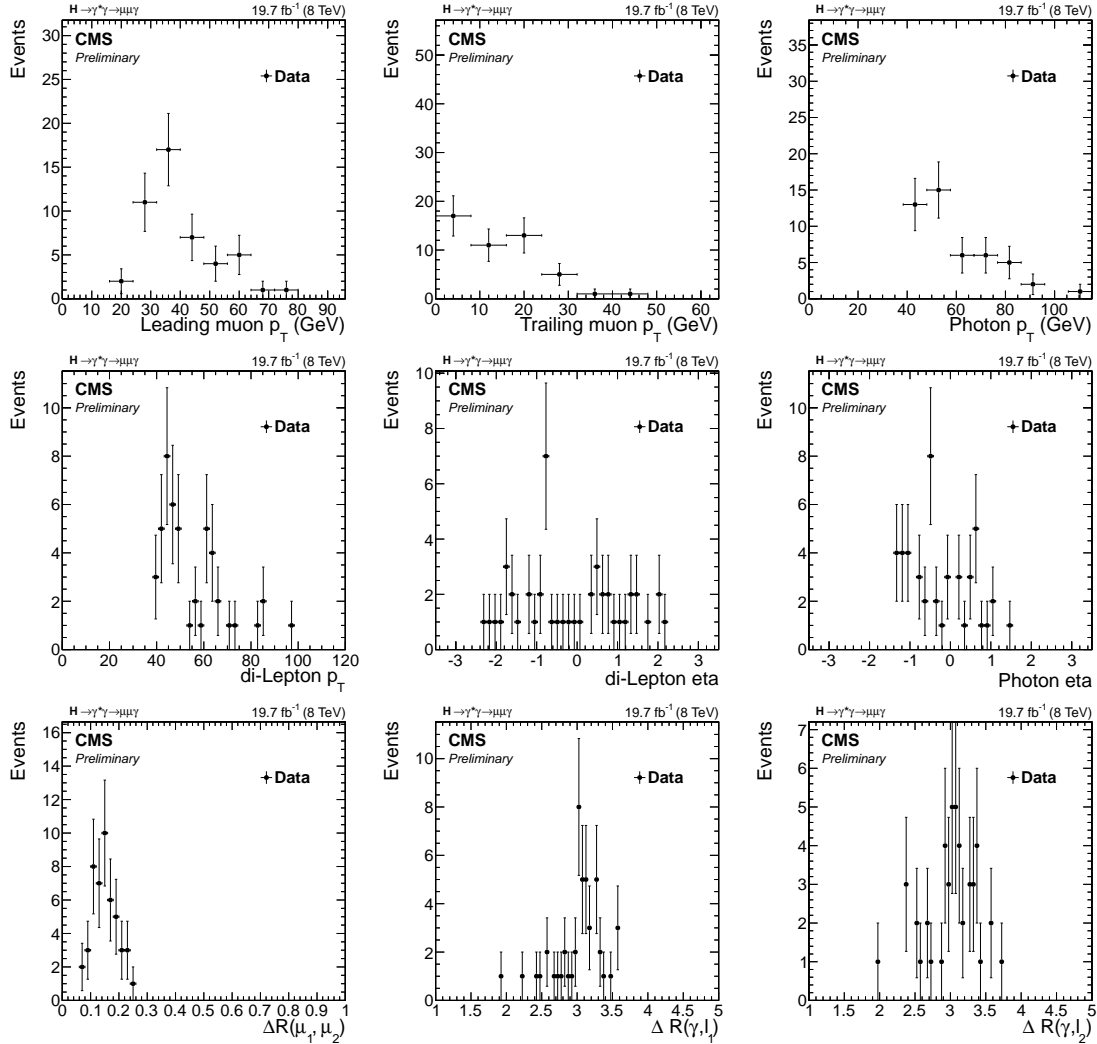


Figure D.25. Distributions of the key variables in data events after the full selection of the  $H \rightarrow (J/\psi)\gamma$  search. Transverse momenta of the muons, the dimuon system and the photon; pseudorapidity of the photon and the dimuon system; distances  $\Delta R_{\eta\phi}$  between the objects.

## APPENDIX E

### **Effect of the Systematics on the Expected Limits**

Here I compare the expected limits in the Dalitz search analysis with and without the systematic uncertainties enabled in the limit setting procedure. I only consider the most sensitive *EB* category in muon channel. I find that applying the systematic uncertainties change the median of the expected limit by less than 4–5%, and also widens the error band by a little bit. Overall, the analysis sensitivity is limited by the size of the data sample, and not by the systematic uncertainties.

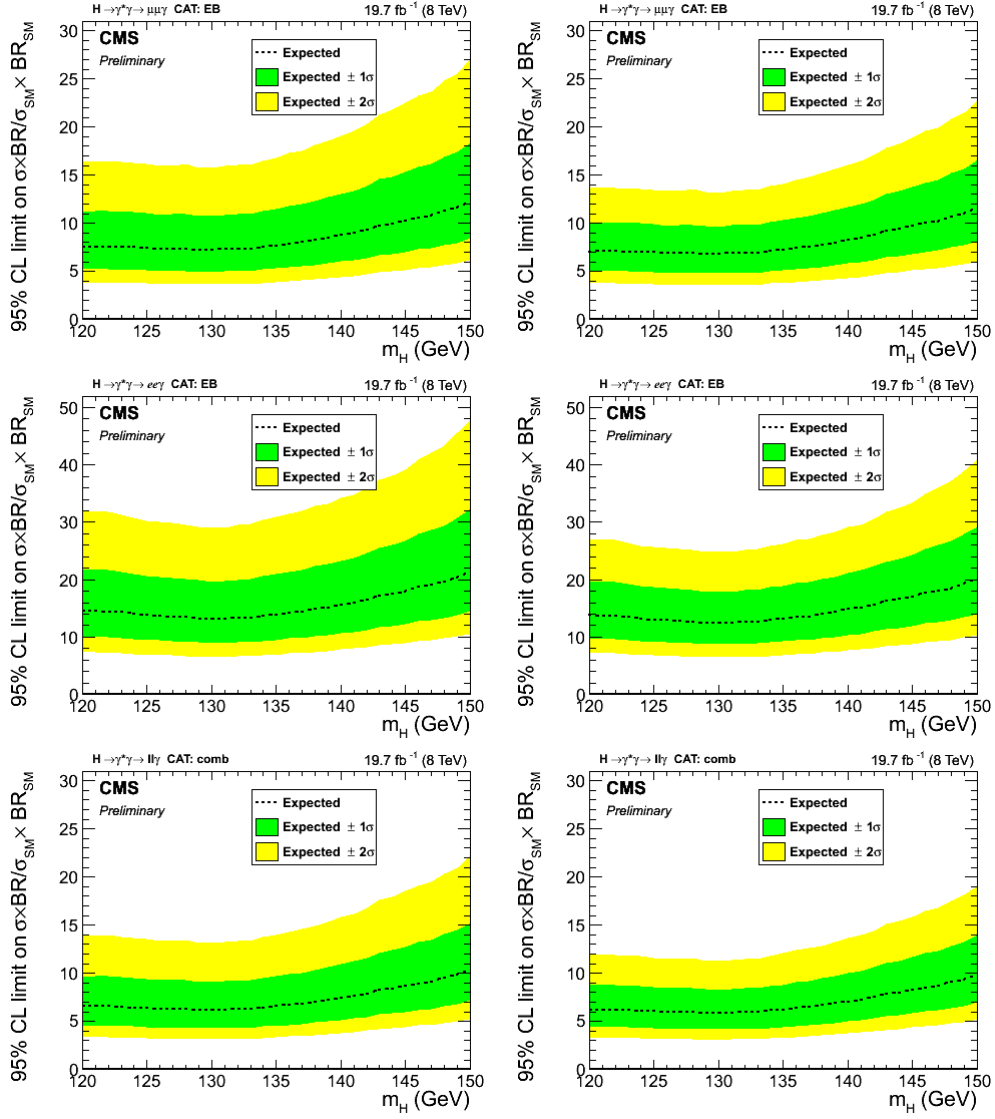


Figure E.1. Expected limits vs  $m_H$ , left: default; right: without systematics. Top: muon channel in EB category; middle: electron channel; bottom: combined.